universität wien

MASTERARBEIT

Titel der Masterarbeit

„Computational study on ruthenium anticancer complexes in the presence of Reactive Oxygen Species “

verfasst von

Christoph Bauer BSc

angestrebter akademischer Grad

Master of Science (MSc)

Wien, 2013

Studienkennzahl lt. Studienblatt:	A 066 862
Studienrichtung lt. Studienblatt:	Masterstudium Chemie
Betreut von:	Univ.-Prof. Dr. **Leticia González Herrero**

Computational study on ruthenium anticancer complexes in the presence of Reactive Oxygen Species

Christoph Bauer
Institute of theoretical chemistry, University of Vienna

October 14, 2013

Abstract

The subject of this thesis is the study of the reduction-oxidation chemistry of ruthenium coordination compounds in the presence of reactive oxygen species (ROS). KP1019 and NAMI-A, two ruthenium compounds currently in clinical trials, were chosen as model systems to study chemical reactions using a Density Functional Theory (DFT) method. The objective of this thesis is to gain knowledge of the chemistry of these compounds in the presence of hydrogen peroxide and potential follow-up reactions. Thereby we want to help contributing to the elucidation of possible reaction mechanisms of KP1019 and NAMI-A type compounds with ROS. In the end, the goal is to draw conclusions concerning the possible reduction-oxidation chemistry of ruthenium anticancer coordination compounds *in vivo*.

Contents

1 Introduction 4
1.1 Platinum Compounds in Cancer Therapy . . . 4
1.2 Ruthenium Compounds in Cancer Therapy . . . 5
1.2.1 Ruthenium Compounds Successful in Clinical Trials: KP1019 and NAMI-A . . . 5
1.3 Activation by Reduction Hypothesis . . . 6
1.4 The Biological Relevance of reactive oxygen species (ROS) . . . 8
1.4.1 Source of ROS in Biological Context . . . 8
1.4.2 Fenton and Fenton-Like Reactions . . . 8
1.4.3 Reactivity of the Hydroxyl Radical, Oxidative Damage to DNA . . . 9
1.4.4 Enzymatic Conversion of ROS . . . 10
1.4.5 ROS and Cancer . . . 10
1.5 Goals of this Thesis . . . 11

2 Theory 13
2.1 The Schrödinger Equation . . . 13
2.2 The Hartree-Fock Approximation . . . 14

2.3 Density Functional Theory . . . 16
2.3.1 The Thomas-Fermi Model . . . 17
2.3.2 The Hohenberg-Kohn Theorems . . . 18
2.3.3 The Kohn-Sham Method . . . 19
2.3.4 The Local Spin Density (LSD) and Generalized Gradient (GGA) approximations . . . 20
2.3.5 Hybrid Functionals . . . 22
2.3.6 Dispersion Correction . . . 22
2.4 The Broken Symmetry DFT Ansatz . . . 23
2.5 Basis Sets . . . 24
2.5.1 Pople Split Valence Basis Sets . . . 24
2.5.2 Effective Core Potentials (ECP) . . . 25
2.6 The Poisson-Boltzmann (PB) Implicit Solvation model . . . 25

3 Computational Details 27
3.1 Methods for all systems . . . 27
3.2 Method for Systems with Spin Contamination . . . 29

4 Results and Discussion 32
4.1 Conformational Analysis Examplified by KP1019 Anion Rotamers 32
4.2 Fenton-like Reactions: Heterolytic vs. Homolytic Peroxide Bond Cleavage . . . 35
4.2.1 Prelude: Aquation and Perhydrolysis of KP1019 and NAMI-A derivatives . . . 38
4.2.2 Oxidation of Ru^{2+} Compounds . . . 39
4.2.3 Oxidation of Ru^{3+} Compounds . . . 42
4.3 Oxygen Atom Transfer (Singlet PES) . . . 49
4.4 Hydrogen Atom Transfer (HAT) to Ruthenyl Compounds . . . 54
4.4.1 Structures of the HAT Mechanism . . . 55
4.4.2 The Energetics of the HAT Mechanism . . . 60

5 Conclusion and Outlook 65

6 Acknowledgment 68

7 Glossary 69

Appendix A 72

Appendix B: Zusammenfassung der Arbeit in deutscher Sprache 73

References 74

1 Introduction

Transition metal compounds have been used to battle cancer for more than four decades. Research groups from all over the world are currently searching for new drug candidates containing a variety of different transition metals, focusing also on their reduction-oxidation properties [1, 2].

In this introduction, first the Pt anticancer agents will be presented followed by the Ru anticancer drug candidates. Then, the "activation by reduction" hypothesis will be discussed briefly in section 1.3. Reactive oxygen species (ROS), being the biochemical agents that could reoxidize transition metal compounds, and their reactions will be presented in section 1.4. Wrapping up the introduction, the goals of this thesis will be stated concisely in section 1.5.

1.1 Platinum Compounds in Cancer Therapy

The success story of transition metal compounds in cancer therapy began with the discoveries of Barnett Rosenberg and coworkers at Michigan state university in the 1960s [3, 4]. Cisplatin was the first transition metal based anticancer drug that passed clinical trials and has been approved by the FDA since 1978. The use of Cisplatin has dramatically increased the cure rate of testicular cancer[5] and today, the drug is approved for treatment of various tumor types.[6] Its mode of action involves most likely the formation of Cisplatin-DNA adducts by binding to the N-7 sites of adjacent guanines from which apoptosis eventually follows [6].

The success of Cisplatin (see Figure 1.1) spawned a new field for research in bioinorganic chemistry. The search for new compounds is ongoing but despite undoubtedly huge efforts, only two other platinum based anticancer drugs have gained worldwide approval, namely Oxaliplatin and Carboplatin (see Figure 1.1) notwithstanding the fact that several other compounds have been approved locally [7, 8].

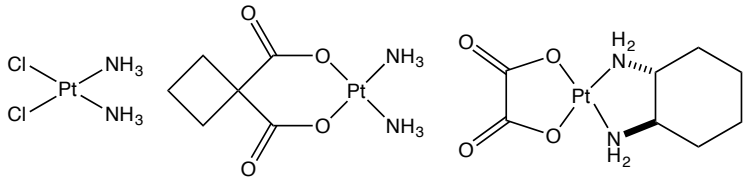

Figure 1.1: Pt^{II} based anticancer drugs

Pt(II) drugs have, however, the disadvantage of being severely neuro- and nephrotoxic [6]. This is the reason why development of anticancer agents based on other transition metals, foremost ruthenium, has been initiated. As detailed in section 1.2 below, in recent years, the interest in ruthenium compounds has increased dramatically with several different kinds of Ru anticancer compounds currently in development.

1.2 Ruthenium Compounds in Cancer Therapy

While ruthenium compounds are not yet of the same importance in cancer therapy as platinum compounds, there is potential for a widespread use of such molecules since some of them have been found to be either cytotoxic against cancer cells selectively, or inhibitors to metastasis formation. Section 1.2.1 will focus on two of the best described ruthenium compounds in the field of anti-cancer drug development.

1.2.1 Ruthenium Compounds Successful in Clinical Trials: KP1019 and NAMI-A

Currently, two promising Ru drug candidates, namely NAMI-A (Imidazolium *trans*-[tetrachlorido DMSO imidazole ruthenate(III)] and KP1019 (Indazolium *trans*-[tetrachloridobis (1H-indazole) ruthenate(III)], the latter having been developed by the research group of Bernhard Keppler, are in clinical trials [9, 10]. The structural formulae of these compounds, are in Figure 1.2a and Figure 1.2b, respectively.

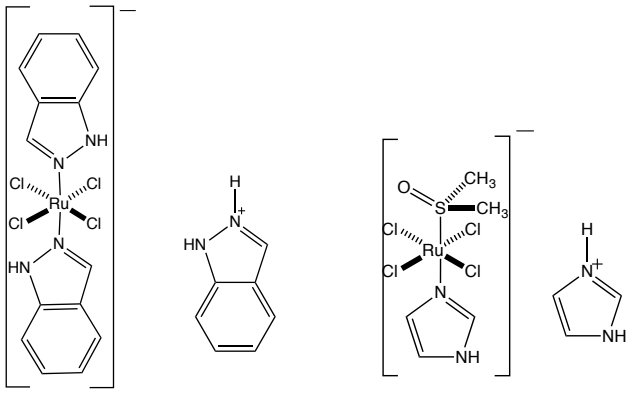

(a) Structural formula for Indazolium *trans*-[tetrachloridobis(1H-indazole)ruthenate(III)], KP1019

(b) Structural formula for Imidazolium *trans*-[tetrachlorido DMSO imidazole ruthenate(III)], NAMI-A

Figure 1.2: Structural formulae of KP1019 and NAMI-A

The modes of action of these two compounds have remained unknown. However, many experimental and theoretical studies have been published about certain elements of their chemistry which may help to explain their (selective) potency against cancer cells. In the following, a selection of studies on KP1019 and NAMI-A will be presented.

1.2.1.1 KP1019

KP1019[11] is used against solid tumors. Cellular uptake of KP1019 is assumed to take place mediated by transferrin [12] which helps explain the apparent tumor selectivity of KP1019. KP1019 is bioreducible and a correlation has been found between its reduction potential and its in vitro

potency [13]. Therefore it has been suggested that KP1019 in its ruthenate(III) form is in fact a pro-drug and its ruthenate(II) reduced form the active species, corresponding well to the "activation by reduction" hypothesis which has been further supported by a study finding increased activity of KP1019 at high concentrations of ascorbic acid [14]. It is, however, not clear in which way KP1019 or any metabolite thereof eventually induces apoptosis in cancer cells.

1.2.1.2 NAMI-A

NAMI-A is primarily used against metastases[15]. According to literature, it undergoes aquation (ligand exchange) reactions within minutes [16] and is more soluble in water than KP1019. There have also been experiments confirming that NAMI-A is readily reducible by such bioreductant molecules as ascorbic acid or glutathione (GSH) whose reactions by means of outer sphere single electron transfer yield a reduced Ru^{2+} complex [17, 18, 19]. Quite recently, a study on human ovarian cancer cells has shown significant cellular uptake of NAMI-A with the drug also being found within the nucleus[20]. Summarizing recent literature, it can be concluded that NAMI-A's mode of action is quite possibly a combination of extra- and intracellular processes.

Additionally, a DFT study on the hydrolysis of NAMI-A has recently been performed supporting claims that NAMI-A is easily reduced and hydrolyzed, yielding mono- and diaquated species of its reduced version [21]. This article by Vargiu et al. has amended a separate study by Chen et al. [22], which considered only the hydrolysis of NAMI-A as administered in its Ru^{3+} form.

Chiorescu et al. [23] have investigated the hydrolysis reactions of Ru(III) anticancer agents including KP1019 and NAMI-A using a DFT/Continuum Dielectric Medium (CDM) approach. The calculations predict, as opposed to former computational studies [22, 21], that the hydrolysis of the Ru(III) species follows an interchange mechanism with dissociative character, whereas the hydrolysis of the reduced Ru(II) analogues follows a limiting dissociative mechanism via significantly lower activation barriers. [23] The same authors[23] have also studied using DFT/CDM the reactions of the partially hydrolyzed species with functional groups of biomolecules and analyzed the control of the reduction potentials of Ru anticancer agents by (i) the axial ligand, (ii) the binding of biomolecules, and (iii) the environment.

These scientific findings on KP1019 and NAMI-A type compounds fit well into a model that has become known as "activation by reduction" hypothesis. This model will be introduced in the following section.

1.3 Activation by Reduction Hypothesis

"Activation by reduction" states that transition metal based drugs (or drug candidates) are not given to the patient in their active form. Instead, a metabolized, reduced form of the compound acts as the cytotoxin killing off the cancer cells. For Ru compounds specifically, this hypothesis has been brought into play as early as 1980 [24].

Reduction of e.g. Pt(IV) or Ru(III) compounds is probable because solid tumors have been shown to be hypoxic (low O_2 partial pressure) by the use of oxygen electrodes[25, 26]. Hypoxia regulates key biological pathways that may aid malignant tumor progression such as angiogenesis [27].

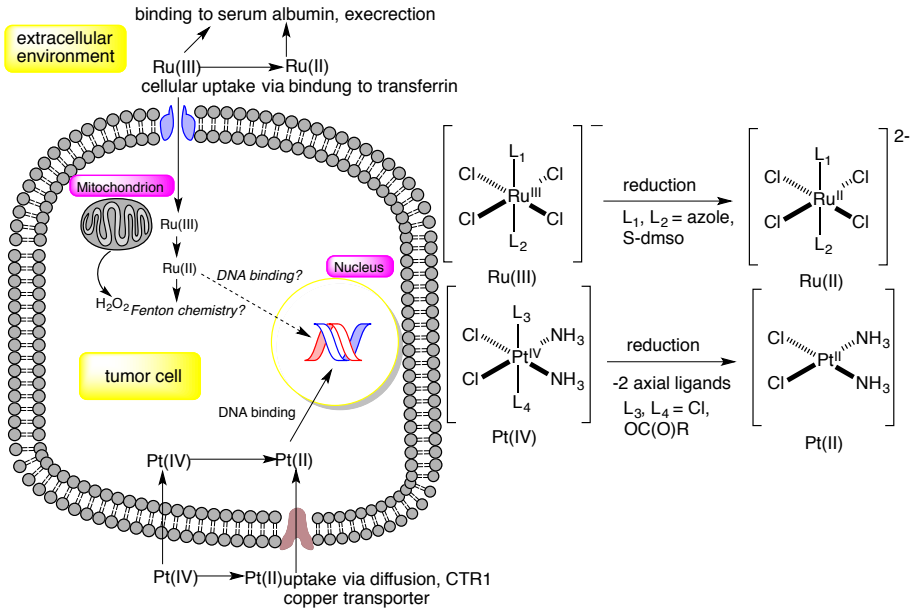

Figure 1.3: Illustration of the activation by reduction hypothesis. Note that explicit aquation reactions and charges for Pt compounds have been omitted for clarity.

Figure 1.3 is a (selective) summary of the processes that may be going on with Pt(IV) and Ru(III) anticancercompounds in the body. Pt(IV) compounds may be reduced extracellularly [28] or within a cancer cell. They may enter the tumor cell by diffusion or, after extracellular reduction, by the CTR1 copper transporter [6]. The main idea behind the development of Pt(IV) compounds is that they are more inert [7] and thus less toxic and may be given orally. Subsequently, after reduction to Pt(II), they bind to DNA much like Pt(II) anticancer drugs. The suggestions for metabolic processing of Pt based anticancer drugs displayed in Figure 1.3 are taken from the literature [6, 12, 29, 2].

For Ru(III) compounds such as KP1019 and NAMI-A, the reduction may also happen extracellularly or intracellulary by biochemical reducing agents, see section 1.2.1 above. Ligand exchange (e.g. water for chloride) for Ru(II) is faster than for Ru(III)[30, 24, 31]. The step following the cellular uptake of compounds is, however, unclear.

Since ruthenium has stable oxidation states from II to IV, the possibility of Fenton-like reactions for Ru(II) has been included in Figure 1.3. Even in hypoxic environments, different reactive oxygen species (ROS) such as the superoxide radical anion or hydrogen peroxide may exist in tumor cells, even in higher concentrations than in normal cells. An introduction to these species is given

in the next section.

1.4 The Biological Relevance of reactive oxygen species (ROS)

1.4.1 Source of ROS in Biological Context

ROS are classified as reactive molecules in biological context that contain oxygen. The most prominent examples are O_2, H_2O_2, the hydroxyl radical $^{\cdot}OH$ and the superoxide radical anion, $O_2^{-\cdot}$.

O_2 is the terminal electron acceptor in the mitochondrial electron transport chain for aerobic organisms and thus the basis for aerobic life.

In aerobic organisms, superoxide is leaked from the electron transport chain in the mitochondria. It is then converted by superoxide dismutase to O_2 (which can be reintroduced into the electron transport chain) and H_2O_2.

The role of hydrogen peroxide in the cell is of course vastly important but beyond the scope of this thesis. A review on the importance of H_2O_2 in signaling processes is given in reference [32]. For the implication of H_2O_2 in cancer, see section 1.4.5.

The origin of the hydroxyl radical in biological systems is most likely to be the breakdown of H_2O_2 by the Fenton and Fenton-like reactions which will be discussed in the following section.

1.4.2 Fenton and Fenton-Like Reactions

Transition metals in the presence of H_2O_2 may undergo a Fenton-like reaction type. The Fenton reaction can be described as the breakdown of hydrogen peroxide by ferrous iron, yielding an oxidated iron species and fragments of H_2O_2. Fenton made his original discovery of the oxidizing properties of ferrous iron in combination with hydrogen peroxide in 1894 [33]. There are two competing proposals for the mechanism of the Fenton reaction, regarding the nature of the oxidizing species which arise from it:

$$Fe^{2+} + H_2O_2 \longrightarrow Fe^{3+} + OH^- + OH^{\cdot} \tag{1.1}$$

$$Fe^{2+} + H_2O_2 \longrightarrow FeO^{2+} + H_2O \tag{1.2}$$

Hydroxyl radicals as oxidants arising from the Fenton reaction (according to reaction equation 1.1) were first proposed by Haber and Weiss in 1934 [34] whereas the hypothesis of high valent ferryl iron oxo species with a formal oxidation state of iron(IV) (as stated in reaction equation 1.2) was first formulated by Bray and Gorin in 1932 [35].

The reaction given in equation 1.1 is a homolytic dissociation of H_2O_2, catalyzed by iron whereas the equation 1.2 describes a heterolytic H_2O_2 dissociation.

In principle, this type of reaction with hydrogen peroxide can be formulated for any general transition metal ion M^{n+}:

$$M^{n+} + H_2O_2 \longrightarrow M^{(n+1)+} + OH^- + OH^{\cdot} \tag{1.3}$$

$$M^{n+} + H_2O_2 \longrightarrow MO^{n+} + H_2O \tag{1.4}$$

These reactions are called Fenton-like reactions. It has been theorized that most hydroxyl radicals generated *in vivo* result from Fenton or Fenton-like reactions[36] with the most prevalent of the latter sort being the reaction of Cu^+ with H_2O_2 which has also been experimentally verified [37].

There seems to be no controversy that hydroxyl radicals will be formed in context with Fenton or Fenton-like reactions, yet the question *how and when* these radicals are formed has remained open to discussion.

In 2001, a DFT study of the intermediate of the Fenton reaction has been carried out [38], suggesting that there are a number of active intermediates with the most probable resulting oxidative species of ferryl iron. Buda et al. conclude that free hydroxyl radicals cannot be directly produced by the Fenton reaction [38]. This, of course, does not preclude that hydroxyl radicals will at some point be produced by a subsequent reaction involving ferryl iron or any other oxidant species resulting from a reaction with ferryl iron.

Whether Fenton-like reactions take place regarding any general transition metal ion M^{n+} with the right number of electrons depends on the chemistry of that transition metal M. Trying to elucidate the mechanism of a reaction of Ru^{2+} coordination compound with H_2O_2 will use a Fenton-like mechanism as a starting point in this work.

1.4.3 Reactivity of the Hydroxyl Radical, Oxidative Damage to DNA

If a hydroxyl radical is generated *via* a Fenton or Fenton-like reaction close to the DNA, a variety of processes may happen.

Firstly, the hydroxyl radical may attack the bases which upon forming an adduct with the OH radical may undergo ring-opening reactions or other kinds of decomposition reactions. For a review on oxidative damage to thymine and guanine, see reference [39].

A second important target for the OH radical would be the sugar moieties in the backbone of DNA. There, the hydroxyl radical may abstract a hydrogen atom which may ultimately lead to strand breaks. A study on this subject can be found in reference [40].

While there is no certainty yet on how the OH radical induces strand breaks in DNA there is virtually no doubt that the reactions that do occur happen at or near the diffusion limit due to the high reactivity of the OH radical.

1.4.4 Enzymatic Conversion of ROS

A number of well described enzymes contribute to the conversion/deactivation of ROS in the cell.

The superoxide radical anion $O_2^{-\cdot}$ is converted by the metalloenzyme superoxide dismutase (SOD) to hydrogen peroxide (H_2O_2) and O_2. The half reactions pertaining to this disproportionation read

$$M^{n+}\text{–SOD} + O_2^{-\cdot} \longrightarrow M^{(n-1)+}\text{–SOD} + O_2 \text{ and} \tag{1.5}$$

$$M^{n+}\text{–SOD} + O_2^{-\cdot} + 2\,H^+ \longrightarrow M^{(n+1)+}\text{–SOD} + H_2O_2, \tag{1.6}$$

where M may be Cu(I) or Mn(II). A description of the mechanism of copper/zinc SOD based on experimental observation is found in reference [41].

H_2O_2 and organic hydroperoxides are converted by the catalase and peroxidase metalloenzymes to H_2O and O_2. This can also be written as a disproportionation of peroxides:

$$2\,H_2O_2 \xrightarrow{\text{catalase/peroxidase}} 2\,H_2O + O_2 \text{ or} \tag{1.7}$$

$$2\,\text{ROOH} \xrightarrow{\text{peroxidase}} 2\,\text{ROH} + O_2. \tag{1.8}$$

While human catalase is heme-based (for a review, see reference [42]) there is also a (microbial) variant with manganese in the active center. For a review of manganese-dependent catalase, see ref.[43].

The mechanism of catalases/peroxidases is not entirely elucidated but will not be the subject of this thesis. The difference between catalases and peroxidases, i.e. the reason why catalase can only convert H_2O_2 but not organic hydroperoxides but peroxidases can convert both, is the substrate channel whereby the peroxide reaches the active center [44].

1.4.5 ROS and Cancer

The examples shown in this part are merely a selection of current literature on the subject of ROS and cancer and serve as background information in order to understand the motivation and the goals of this thesis.

Intracellular ROS levels seem to play a major role in signaling involved in cell proliferation [45]. Additionally, several human tumor cell lines (among them melanoma and colon cancer cell lines) have been found to produce high levels of H_2O_2 [29, 46]. López has reviewed the possible implication of H_2O_2 in cancer and suggested that there is a critical H_2O_2 concentration above which cancer cells die [47].

H_2O_2 has also been suggested to be implicated in tumor cell apoptosis after treatment of HL-60 leukemia cell lines with etoposide and camptothecin (both topoisomerase I inhibitors) lead to high intracellular peroxide levels and apoptosis which could be prevented by the activity of catalase [48].

In addition, KP1019 has been found to induce elevated levels of hydrogen peroxide in HT29 human colon carcinoma cells [49].

Concerning the superoxide radical anion and cancer, Zhou et al [50] have found that 2-Methoxyestradiol (2-ME), an SOD inhibitor, induces high intracellular $O_2^{-\cdot}$ levels in leukemia cells and subsequent apoptosis.

1.5 Goals of this Thesis

The proposed reactions to be investigated in this work are summarized in Figure 1.4.

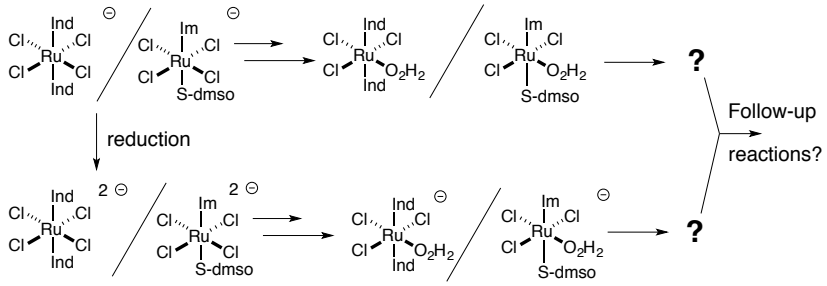

Figure 1.4: Summary of the proposed reactions to be treated

The goal of this thesis is to investigate the reduction-oxidation behavior of Ru based anticancer compounds KP1019 and NAMI-A (and selected derivatives thereof) in the presence of hydrogen peroxide. The method of choice will be DFT. Physiological conditions will be approximated by a continuum dielectric model (CDM), simulating aqueous solution.

The starting point will be a model for reoxidation of Ru^{II} compounds by H_2O_2 in a Fenton-like reaction. In addition, oxidative pathways starting from Ru^{III} compounds (in which oxidation state Ru anticancer drugs are administered) will also be investigated.

Characterization of the resulting species from the oxidation reactions calculated will include the discussion of optimized structures along the reactive pathways described as well as thermodynamic data (reaction free energies, reduction potentials). We aim at an accurate prediction of activation barrier heights and reaction free energies in aqueous solution in order to classify the reactive pathways by their likelihood.

A prevalent reactive pathway is characterized by low activation barriers and negative reaction free energies. The so predicted reaction product will be the

starting point to treat possible follow-up reactions, which may lead to a proposal of a catalytic cycle in which Ru anticancer compounds may continually be reduced and oxidized. Thus, even a very low concentration of these compounds in a (tumor) cell could have a great effect on the entire biochemical system.

The obatined computational results should then provide orientation for experimentalists and suggest new experiments from which the predictive powers of the methods used herein may be assessed. Ultimately, we hope to help to elucidate the mode of action of ruthenium-based anticancer compounds in order to provide guidelines for future efficient anticancer drug design.

2 Theory

This section will present the theoretical background to the methods used in this thesis. Firstly, the Schrödinger equation and the Hartree-Fock (HF) method will be presented in order to establish the wave function, the Hamiltonian and the SCF procedures as concepts which are needed in Kohn-Sham DFT. Secondly, DFT itself will be treated both conceptually and with additions devised during the last decades.

A glossary of abbreviations and symbols used heavily in this section will is given in the appendix to this thesis.

2.1 The Schrödinger Equation

Quantum chemistry is the line of work that deals with solving the time independent Schrödinger Equation (TISE):

$$\widehat{H}\Psi = E\Psi. \tag{2.1}$$

Ψ is the wave function that describes the entire system and $\widehat{H}$ the (total) Hamiltonian which consists of five terms. In the following the greek indices α, β are running over the nuclei and the latin indices i, j over the electrons. N_α shall be the total number of nuclei and n the total number of electrons.

$$\widehat{H} = \hat{T}_\mathrm{n} + \hat{T}_\mathrm{e} + \hat{V}_\mathrm{nn} + \hat{V}_\mathrm{ee} + \hat{V}_\mathrm{ne} \qquad \text{, where} \tag{2.2}$$

$$\hat{T}_\mathrm{n} = -\frac{\hbar^2}{2}\sum_{\alpha=1}^{N_\alpha}\frac{\nabla_\alpha^2}{m_\alpha} \qquad \hat{T}_\mathrm{e} = -\frac{\hbar^2}{2m_e}\sum_{i=1}^{n}\nabla_i^2 \qquad \text{and}$$

$$\hat{V}_\mathrm{nn} = \frac{1}{4\pi\epsilon_0}\sum_{\alpha=1}^{N_\alpha-1}\sum_{\beta=\alpha+1}^{N_\alpha}\frac{z_\alpha z_\beta e^2}{r_{\alpha\beta}},$$

$$\hat{V}_\mathrm{ee} = \frac{1}{4\pi\epsilon_0}\sum_{i=1}^{n-1}\sum_{j=i+1}^{n}\frac{e^2}{r_{ij}},$$

$$\hat{V}_\mathrm{ne} = -\frac{1}{4\pi\epsilon_0}\sum_{i=1}^{n}\sum_{\alpha=1}^{N_\alpha}\frac{z_\alpha e^2}{r_{i\alpha}},$$

where $\hbar = \dfrac{h}{2\pi}$ is Planck's constant h divided by 2π, m_e is the mass of an electron, $\hat{T}_\mathrm{n}$ is the kinetic energy operator of the nuclei, $\hat{T}_\mathrm{e}$ the kinetic energy operator for the electrons, $\hat{V}_\mathrm{nn}$ describes the nuclear repulsion , $\hat{V}_\mathrm{ee}$ accounts for the electron-electron repulsion and $\hat{V}_\mathrm{ne}$ stands for the attraction between the positively charged nuclei and the negatively charged electrons. By using the Born-Oppenheimer approximation [51] we separate the electronic from the nuclear contributions. If one looks at the electronic problem only, all $r_{\alpha\beta}$ and $r_{i\alpha}$ values are rendered constant (we retain a fixed nuclear geometry). The electronic part of the Hamilton operator $\widehat{H}_\mathrm{el}$ is constituted by:

$$\widehat{H}_{\mathrm{el}} = \hat{T}_{\mathrm{e}} + \hat{V}_{\mathrm{ne}} + \hat{V}_{\mathrm{ee}}. \tag{2.3}$$

Using the Born-Oppenheimer approximation, we can employ the following computational strategy with a given geometry:

1. Solve the time-independent Schödinger equation for the electronic system,

$$\widehat{H}_{\mathrm{el}}\Psi_{\mathrm{el}} = E_{el}\Psi_{\mathrm{el}}. \tag{2.4}$$

2. Evaluate the nuclear repulsion energy E_{nn} from $\hat{V}_{\mathrm{nn}}$.

3. Evaluate the total energy, $E_{\mathrm{tot}} = E_{\mathrm{el}} + E_{\mathrm{nn}}$.

For each geometry we thus obtain an energy value, having split the total wave function Ψ into an electronic and a nuclear part. The representation for the total energy depending on a fixed nuclear geometry is called potential energy surface (PES) and is one of the key concepts in quantum and computational chemistry.

2.2 The Hartree-Fock Approximation

This subsection follows in essence the book by Szabo and Ostlund[52] which provides an excellent introduction to the field of quantum chemistry.

The first step towards a solution of the electronic TISE for (ground state) molecular systems is to find a suitable ansatz for the electronic wave function $\Psi_{\mathrm{el}}(\vec{x}_1 ... \vec{x}_n)$ which has to comply with Pauli's principle. Thus, $\Psi_{\mathrm{el}}(\vec{x}_1 ... \vec{x}_n)$, consisting of one-electron functions $\chi_1(\vec{x}_1) ... \chi_n(\vec{x}_n)$ (where $\vec{x}_n$ are the spin coordinates of the n^{th} electron) has to fulfill the following conditions:

1. Ψ_{el} must be antisymmetric, i.e. upon exchange of two electrons, its sign must change.

2. Ψ_{el} must become zero if two electrons occupy the same space i.e. are described by the same χ_i.

A Slater determinant $|\Psi\rangle$ meets these criteria.

$$|\Psi\rangle = \frac{1}{\sqrt{n!}} \begin{vmatrix} \chi_1(\vec{x}_1) & \chi_2(\vec{x}_1) & \cdots & \chi_n(\vec{x}_1) \\ \chi_1(\vec{x}_2) & \chi_2(\vec{x}_2) & \cdots & \chi_n(\vec{x}_2) \\ \vdots & \vdots & \ddots & \vdots \\ \chi_1(\vec{x}_n) & \cdots & \cdots & \chi_n(\vec{x}_n) \end{vmatrix}, \tag{2.5}$$

where $\frac{1}{\sqrt{n!}}$ is the normalization factor.

We introduce the notation χ_i for the i$^{\mathrm{th}}$ spin orbital. The spin orbitals form an orthonormal, complete basis set.

The Hartree-Fock approximation leads to equations for single electrons moving in the mean field of all other electrons. A single Slater determinant is used

as the trial wave function which is then treated according to the variational principle:

$$\langle \Psi_{\text{trial}} | \widehat{H} | \Psi_{\text{trial}} \rangle = E_{\text{trial}} \geq E_0, \tag{2.6}$$

where E_0 is the exact electronic ground state energy, defined as E_{tot} before, having dropped the "tot" subindex.

The one-electron Fock operator $\hat{f}(\vec{x}_i)$ acts now on our spin orbitals χ_i. The equations are as follows[1]:

$$\hat{f}(\vec{x}_1)\chi(\vec{x}_1) = \varepsilon\chi(\vec{x}_1). \tag{2.7}$$

We further simplify the notation by writing $\hat{f}(i)$ instead of $\hat{f}(\vec{x}_i)$ where i is the i$^{\text{th}}$ electron in the mean field of all the other electrons. $\hat{f}(i)$ is the sum of the i$^{\text{th}}$'s electron kinetic and potential energies:

$$\hat{f}(i) = \underbrace{-\frac{1}{2}\nabla_i^2 - \sum_{\alpha=1}^{N_\alpha} \frac{z_\alpha}{r_{i\alpha}}}_{\hat{h}_i} + \hat{v}_i^{\text{HF}}. \tag{2.8}$$

$\hat{h}_i$ is called the core Hamiltonian operator and $\hat{v}_i^{\text{HF}}$ the effective potential also known as Hartree-Fock potential. It consists of the sum of Coulomb operators j and exchange operators k for the i$^{\text{th}}$ electron.

$$\hat{v}_i^{\text{HF}} = \sum_b \hat{j}_b(i) - \hat{k}_b(i). \tag{2.9}$$

The Coulomb and exchange operators are defined by their interaction with spin orbital χ_a:

$$\hat{j}_b(1)\chi_a(1) = \left[\int d\vec{x}_2 \chi_b^*(2) \frac{1}{r_{12}} \chi_b(2)\right] \chi_a(1), \tag{2.10}$$

$$\hat{k}_b(1)\chi_a(1) = \left[\int d\vec{x}_2 \chi_b^*(2) \frac{1}{r_{12}} \chi_a(2)\right] \chi_b(1). \tag{2.11}$$

The expectation values of the Coulomb and exchange operators are often written in a Bra-Ket notation:

$$\langle \chi_a(1) | \hat{j}_b(1) | \chi_a(1) \rangle = \int\int d\vec{x}_1 d\vec{x}_2 \chi_a^*(1)\chi_b^*(2) \frac{1}{r_{12}} \chi_a(1)\chi_b(2) = \langle ab|ab\rangle, \tag{2.12}$$

$$\langle \chi_a(1) | \hat{k}_b(1) | \chi_a(1) \rangle = \int\int d\vec{x}_1 d\vec{x}_2 \chi_a^*(1)\chi_b^*(2) \frac{1}{r_{12}} \chi_b(1)\chi_a(2) = \langle ab|ba\rangle. \tag{2.13}$$

The Hartree Fock (HF) equation is an eigenvalue equation that has to be solved iteratively in an Self Consistent Field (SCF) procedure because the Fock operator itself depends on the spin orbitals which are to be optimized to give the lowest ground state energy.

[1] We conveniently switch now to atomic units.

$$\hat{f}|\chi_a\rangle = \varepsilon_a|\chi_a\rangle. \tag{2.14}$$

The physical interpretation for ε_a (which in a mathematical sense is a Lagrange multiplier) is the orbital energy of χ_a. Koopmans' theorem[53] equates the ε of the highest occupied molecular orbital (HOMO) to the negative first ionization potential of that compound. Since ε_a is the expectation value of the Fock operator we can write:

$$\begin{aligned} \varepsilon_a = \langle\chi_a|\hat{f}|\chi_a\rangle =& \langle a|\hat{h}|a\rangle + \sum_b \langle ab||ab\rangle \ , \\ \text{with } \langle ab||ab\rangle =& \langle ab|ab\rangle - \langle ab|ba\rangle, \end{aligned} \tag{2.15}$$

where $\langle a|\hat{h}|a\rangle$ is the expectation value of the core Hamiltonian acting on the spin orbital χ_a and the expression $\langle ab||ab\rangle$ is the combination of Coulomb and exchange integrals, thus the expectation value of $\hat{v}^{\mathrm{HF}}$. The total electronic ground state energy obtained by using the HF method, E_{HF} is now:

$$E_{\mathrm{HF}} = \sum_a \varepsilon_a - \frac{1}{2}\sum_a \sum_b \langle ab||ab\rangle. \tag{2.16}$$

The reason for the subtraction of half of all Coulomb and exchange terms is the double-counting which occurs by evaluating electron 1 in the field of electron 2 and electron 2 in the field of electron 1. Thus, the HF energy is not the sum of all spin orbital energies.

The HF method by itself will not be used in any of the calculations relevant to this thesis. The reasons why it has been described are, that the HF procedure is the foundation of all wave-function based correlation methods.Furthermore, Kohn-Sham DFT uses the same SCF formalism as the HF method. We will see this in a subsequent section of this work.

2.3 Density Functional Theory

This section gives an overview of the vastly popular DFT method, from its beginnings with the Thomas-Fermi model via the Hohenberg-Kohn theorems and Kohn-Sham equations to hybrid functionals which include *ab-initio* and "pure" DFT contributions. This section will follow, in essence, the book by Robert Parr and Weitao Yang [54] which is considered a standard reference book on this topic.

The basic idea of DFT is to write the energy of an n-electron system as a functional of its density $\rho(\vec{r})$ with the global constraint

$$\int \rho(\vec{r})d\vec{r} = n. \tag{2.17}$$

This idea will be expanded on in the next few subsections.

2.3.1 The Thomas-Fermi Model

The Thomas-Fermi model was the first attempt of calculating the total energy of an electronic system as a functional of the density. It was developed for the uniform electron gas which is a fair approximation for solid metals. In SI units, the energy levels of an electron ($\mathfrak{E}$) in a three-dimensional box with quantum numbers n_x, n_y, n_z are:

$$\mathfrak{E}(n_x, n_y, n_z) = \frac{h^2}{8m_e l^2}(n_x^2 + n_y^2 + n_z^2). \tag{2.18}$$

$$\left(\text{with Planck's constant } h = 6.626 * 10^{-34}\frac{\mathrm{m^2 kg}}{\mathrm{s}}\right)$$

We now conveniently put a number of electrons n into a cubic cell of volume l^3. Within this model, it can be shown that the density of states $g(\mathfrak{E})$ is proportional to $\mathfrak{E}^{\frac{1}{2}}$. As electrons are fermions, they follow the Fermi-Dirac distribution

$$\mathfrak{f}(\mathfrak{E}) = \frac{1}{1 + \exp[\frac{\mathfrak{E}-\mu}{\mathrm{k_B}\Theta}]}, \tag{2.19}$$

where μ denotes the chemical potential which at Θ=0 K is equivalent to the Fermi-energy $\mathfrak{E}_F$ and $\mathrm{k_B}$ is the Boltzmann constant. At 0 K the Fermi-Dirac distribution therefore becomes a step-function.

To arrive at the (total) energy of this free particle system, an integral over all states with respect to their occupation and the density of states must be evaluated:

$$E = 2\int \mathfrak{E}\mathfrak{f}(\mathfrak{E})g(\mathfrak{E})\mathrm{d}\mathfrak{E} = \varkappa\int_0^{\mathfrak{E}_F} \mathfrak{E}^{\frac{3}{2}}\mathrm{d}\mathfrak{E} = \varkappa\frac{2}{5}\mathfrak{E}_F^{\frac{5}{2}}, \tag{2.20}$$

where $g(\mathfrak{E})$ is the density of states, $\varkappa$=$4\pi\left(\frac{2m_e}{h^2}\right)^{\frac{3}{2}} l^3$ and is valid for the n electrons in a 3 dimensional cubic box model. The factor 2 enters into the equation because each level $\mathfrak{E}$ is doubly occupied and every contribution from an occupied level thus has to be counted twice (for 2 n electron systems).
Similarly, for n we find[2]:

$$n = 2\int \mathfrak{f}(\mathfrak{E})g(\mathfrak{E})\mathrm{d}\mathfrak{E} = \varkappa\int_0^{\mathfrak{E}_F} \mathfrak{E}^{\frac{1}{2}}\mathrm{d}\mathfrak{E} = \varkappa\frac{2}{3}\mathfrak{E}_F^{\frac{3}{2}}. \tag{2.21}$$

Rearrangement yields:

$$E = \frac{3}{5}n\mathfrak{E}_F = \frac{3h^2}{10m_e}\left(\frac{3}{8\pi}\right)^{\frac{2}{3}} l^3\left(\underbrace{\frac{n}{l^3}}_{\rho}\right)^{\frac{5}{3}}. \tag{2.22}$$

[2] n is equal to an integration of the density of states g($\mathfrak{E}$) over all d$\mathfrak{E}$ elements, taking into account the Fermi-Dirac distribution $f(\mathfrak{E})$

We have arrived at the Thomas-Fermi functional for the kinetic energy of electrons in a cubic box. Integration over all space yields the Thomas-Fermi kinetic energy functional:

$$T_{\mathrm{TF}}[\rho] = C_{\mathrm{F}} \int \rho^{\frac{5}{3}} d\vec{r}, \tag{2.23}$$

where the Thomas-Fermi constant C_{F} is now 2.871 atomic units.

Unfortunately, since this model assumes a uniform electron gas, it fails for molecules (or any covalent system) where the electrons are extremely localized.

2.3.2 The Hohenberg-Kohn Theorems

Formulated in 1964[55], the Hohenberg-Kohn theorems are the foundation of modern density functional theory.

The first Hohenberg-Kohn theorem states that the density $\rho(\vec{r})$ defines the external potential (any external potential, not necessarily an electrostatic one, but in the case of molecules we will inevitably deal with Coulomb potentials) and thus the wave function for any system. The proof for this theorem is simple: Assuming a non-degenerate ground state of some n-electron system, we show that two different external potentials $V(\vec{r})$ and $V^{'}(\vec{r})$(differing by more than a constant) cannot have the same $\rho(\vec{r})$. $V^{'}(\vec{r})$ defines $\widehat{H}^{'}_{\mathrm{el}}$ and $|\Psi^{'}\rangle$. If we take now $|\Psi^{'}\rangle$ as a wave function for the electronic Hamiltonian $\widehat{H}_{\mathrm{el}}$, we arrive at

$$\begin{aligned}\left\langle \Psi^{'} \middle| \widehat{H}_{\mathrm{el}} \middle| \Psi^{'} \right\rangle &= \left\langle \Psi^{'} \middle| \widehat{H}^{'}_{\mathrm{el}} \middle| \Psi^{'} \right\rangle + \left\langle \Psi^{'} \middle| \widehat{H}_{\mathrm{el}} - \widehat{H}^{'}_{\mathrm{el}} \middle| \Psi^{'} \right\rangle > E_0 \\ &= E^{'}_0 + \int \rho(\vec{r})[V(\vec{r}) - V^{'}(\vec{r})]d\vec{r} > E_0. \end{aligned} \tag{2.24}$$

Similarly, taking $|\Psi\rangle$ for the $\widehat{H}^{'}_{\mathrm{el}}$ problem, we arrive at

$$\begin{aligned}\left\langle \Psi \middle| \widehat{H}^{'}_{\mathrm{el}} \middle| \Psi \right\rangle &= \left\langle \Psi \middle| \widehat{H}_{\mathrm{el}} \middle| \Psi \right\rangle + \left\langle \Psi \middle| \widehat{H}^{'}_{\mathrm{el}} - \widehat{H}_{\mathrm{el}} \middle| \Psi \right\rangle > E^{'}_0 \\ &= E_0 - \int \rho(\vec{r})[V(\vec{r}) - V^{'}(\vec{r})]d\vec{r} > E^{'}_0. \end{aligned} \tag{2.25}$$

Adding equations 2.24 and 2.25 leads to the following contradiction

$$E^{'}_0 + E_0 > E_0 + E^{'}_0. \tag{2.26}$$

Mathematically, this is sufficient proof of the first Hohenberg-Kohn theorem for non-degenerate systems.

The first Hohenberg-Kohn theorem allows us to define the energy of an n-electron system as a functional of its density $\rho(\vec{r})$. The terms are

$$\begin{aligned} E[\rho] &= T[\rho] + V_{\mathrm{ne}}[\rho] + V_{\mathrm{ee}}[\rho] \\ &= F_{\mathrm{HK}}[\rho] + \int \rho(\vec{r}) V_{\mathrm{ne}}(\vec{r}) d\vec{r}, \\ \text{where } F_{\mathrm{HK}}[\rho] &= T[\rho] + V_{\mathrm{ee}}[\rho]. \end{aligned} \tag{2.27}$$

The Hohenberg-Kohn functional $F_{\mathrm{HK}}[\rho]$ is a universal functional and does not depend on the external potential (the positions of the nuclei in a molecule). It is, however, unknown and approximations to it will be described in later subsections of this work.

The second Hohenberg-Kohn theorem is the variational principle for DFT. The central expression is

$$E[\rho_0] \leq E[\rho_{\mathrm{trial}}]. \tag{2.28}$$

The proof for the second Hohenberg-Kohn theorem builds on the first theorem. Since a trial density ρ_{trial} necessarily also defines a trial wave function $|\Psi_{\mathrm{trial}}\rangle$ which differs from the ground state wave function $|\Psi\rangle$ by an external potential $V(\vec{r})_{\mathrm{trial}}$ it follows that any trial density must lead to a higher energy than the true ground state density ρ_0.

2.3.3 The Kohn-Sham Method

The kinetic energy as a functional of the density $\rho(\vec{r})$ is a formidable idea with one substantial drawback: There is no simple analytical expression for it apart from the one of the Thomas-Fermi model (vide supra), which is not a good approximation for molecules. In order to circumvent this problem elegantly, Kohn and Sham developed their approach which introduces one-electron functions into the DFT formalism [56].

The kinetic Kohn-Sham energy is defined by

$$T_{\mathrm{KS}}[\rho] = \sum_a \left\langle \chi_a \left| -\frac{1}{2}\nabla^2 \right| \chi_a \right\rangle. \tag{2.29}$$

The Kohn-Sham spin orbitals denoted in this work as $\chi_a(\vec{r},\sigma)$ (although they are not the same as the HF spin orbitals also called χ) depend on space and spin and are related to the density $\rho(\vec{r})$ by the following equation

$$\rho(\vec{r}) = \sum_a \sum_\sigma |\chi_a(\vec{r},\sigma)|^2, \tag{2.30}$$

where the spin index σ runs over $\uparrow$ and $\downarrow$ spins.

We rewrite now the universal $F_{\mathrm{HK}}[\rho]$ as $F_{\mathrm{KS}}[\rho]$

$$\begin{aligned} F_{\mathrm{KS}}[\rho] &= T_{\mathrm{KS}}[\rho] + J[\rho] + E_{xc}[\rho], \\ \text{where } E_{xc}[\rho] &= T[\rho] - T_{\mathrm{KS}}[\rho] + V_{\mathrm{ee}}[\rho] - J[\rho]. \end{aligned} \tag{2.31}$$

$J[\rho]$ is the coulomb term and $E_{xc}[\rho]$ is called exchange-correlation energy and contains the deviation of $T_{\mathrm{KS}}[\rho]$ from $T[\rho]$, assumed to be small, and the non-classical part of the electron-electron interactionV_{ee}. Since this splitting of terms implies that the particles do not interact, the Kohn-Sham effective potential is defined as follows:

$$V_{\text{eff,KS}}(\vec{r}) = V_{\text{ne}}(\vec{r}) + \frac{\delta J[\rho]}{\delta\rho(\vec{r})} + \frac{\delta E_{xc}[\rho]}{\delta\rho(\vec{r})}$$
$$= V_{\text{ne}}(\vec{r}) + \int \frac{\rho(\vec{r})}{|\vec{r}-\vec{r}'|} d\vec{r}' + V_{xc}(\vec{r}). \tag{2.32}$$

The one-electron functions (spin orbitals) χ_a must now fulfill the equation

$$\underbrace{\left[-\frac{1}{2}\nabla^2 + V_{\text{eff,KS}}(\vec{r})\right]}_{\hat{f}^{\text{KS}}} \chi_a = \varepsilon_a \chi_a, \tag{2.33}$$

and the density is built from equation 2.30. Since the effective potential (and with it the Kohn-Sham Fock operator $\hat{f}^{\text{KS}}$) depends already on $\rho(\vec{r})$, the system of equations must be solved iteratively and the computational procedure is thus very similar to a HF calculation. The total energy in the Kohn-Sham formalism is written as

$$E[\rho] = T_{\text{KS}}[\rho] + J[\rho] + E_{xc}[\rho] + \int V_{\text{ne}}(\vec{r})\rho(\vec{r})d\vec{r}$$
$$= \sum_a \left\langle \chi_a \middle| -\frac{1}{2}\nabla^2 \middle| \chi_a \right\rangle + J[\rho] + E_{xc}[\rho] + \int V_{\text{ne}}(\vec{r})\rho(\vec{r})d\vec{r} \tag{2.34}$$
$$= \sum_a \varepsilon_a - \frac{1}{2}\int\int \frac{\rho(\vec{r})\rho(\vec{r}')}{|\vec{r}-\vec{r}'|} d\vec{r}d\vec{r}' + E_{xc}[\rho] - \int V_{xc}(\vec{r})\rho(\vec{r})d\vec{r}, \tag{2.35}$$

where the first term is equal to

$$\sum_a \varepsilon_a = \sum_a \left\langle \chi_a \middle| -\frac{1}{2}\nabla^2 + V_{\text{eff,KS}}(\vec{r}) \middle| \chi_a \right\rangle. \tag{2.36}$$

Just as in Hartree-Fock theory, the total energy is not just the sum of all eigenvalues ε_a of the one-electron functions. In the next section, we deal with the usual approximation to describe the unknown exchange-correlation energy E_{xc}.

2.3.4 The Local Spin Density (LSD) and Generalized Gradient (GGA) approximations

The exchange-correlation energy can be split into two terms, E_x and E_c, with $\rho^\uparrow$ and $\rho^\downarrow$ as $\uparrow$ and $\downarrow$ spin densities:

$$E_{xc}[\rho^\uparrow, \rho^\downarrow] = E_x[\rho^\uparrow, \rho^\downarrow] + E_c[\rho^\uparrow, \rho^\downarrow]. \tag{2.37}$$

The Local Spin Density Approximation (LSD) states that for a small range in space we may treat the spin density just like the homogeneous electron gas of the Thomas Fermi model. Therefore, the exchange part E_x in this approximation (for derivation, see [54], chapter 6) is:

$$E_x^{LSD}[\rho^\uparrow, \rho^\downarrow] = 2^{1/3} C_x \int [(\rho^\uparrow)^{4/3} + (\rho^\downarrow)^{4/3}] d\vec{r}, \tag{2.38}$$

$$\text{with } C_x = \frac{3}{2}\left(\frac{3}{4\pi}\right)^{4/3}.$$

In spin-polarized DFT the parameter ξ which is a measure for spin-polarization is introduced. If $\xi = 0$ the system is entirely spin-compensated (paramagnetic) while $\xi = 1$ means a system is ferromagnetic, i.e. completely spin-polarized. ξ can be thus defined as:

$$\xi = \frac{\rho^\uparrow - \rho^\downarrow}{\rho^\uparrow + \rho^\downarrow}. \tag{2.39}$$

Under the consideration of ξ, E_x^{LSD} then becomes

$$E_x^{LSD}[\rho^\uparrow, \rho^\downarrow] = \frac{1}{2} C_x \int [\rho^{4/3}[(1+\xi)^{4/3} + (1-\xi)^{4/3}] d\vec{r}. \tag{2.40}$$

The correlation part $E_c[\rho^\uparrow, \rho^\downarrow]$ is not easily derived and cannot be written in an analytical form as a one-particle equation. The work of Vosko, Wilk and Nusair [57] regarding E_c^{LSD} is included in many functionals today, often being referred to as E_c^{VWN} which in this work from now on is used interchangeably with E_c^{LSD}.

A functional that adheres to the LSD method may therefore often feature an exchange-correlation part of the following form:

$$E_{xc}^{LSD}[\rho^\uparrow, \rho^\downarrow] = E_x^{LSD}[\rho^\uparrow, \rho^\downarrow] + E_c^{VWN}[\rho^\uparrow, \rho^\downarrow]. \tag{2.41}$$

In cases where the density is expected to vary even in a small area (such as in molecules) the accuracy of the functional can be improved by taking into account the gradient of the density as a correction. This is also often called the gradient expansion or Generalized Gradient Approximation (GGA) Therefore, E_{xc}^{GGA} includes the corrective $\vec{\nabla}\rho$ e.g. as given by Becke [58] for the exchange part E_x:

$$E_x^{GGA}[\rho^\uparrow, \rho^\downarrow, \vec{\nabla}\rho^\uparrow, \vec{\nabla}\rho^\downarrow] = E_x^{LSD} - \gamma \sum_\sigma \int \rho_\sigma^{4/3} \frac{x_\sigma^2}{(1 + 6\gamma x_\sigma \sinh^{-1} x_\sigma)} d\vec{r}, \tag{2.42}$$

$$\text{with } x_\sigma = \frac{|\vec{\nabla}\rho_\sigma|}{\rho_\sigma^{4/3}} \qquad \text{, where } \sigma \text{ denotes } \uparrow \text{ or } \downarrow \text{ spin.}$$

The empirical parameter γ in this equation is 0.0042 and was obtained by fitting to exchange energies of rare gas atoms.

An outstanding gradient correction for the E_c part was provided by Lee, Yang and Parr in 1988 [59] and is often referred to as E_c^{LYP} in the literature. The LYP gradient correction is an expansion of the Colle-Salvetti formula and has four parameters, originally dubbed a,b,c and d which have been fitted using only the HF Colle-Salvetti formula for the He atom [60]. For details and the numerical values of the parameters mentioned, see the references cited.

2.3.5 Hybrid Functionals

The approach of including the exchange integrals of HF theory as a part of the exchange correlation functional has been very successful. The most prominent example is the Becke three parameter functional B3LYP[61], which incorporates E_X^{HF} in the following way[62]:

$$E_{xc}^{B3LYP} = \mathrm{a}E_X^{HF} + (1-\mathrm{a})E_x^{LSD} + \mathrm{b}E_x^{B88} + E_c^{LSD} + \mathrm{c}(E_c^{LYP} - E_c^{LSD}), \quad \text{with a} = 0.20\ \mathrm{b} = 0.72 \text{ and c} = 0.81, \tag{2.43}$$

where E_x^{HF} is the Hartree-Fock exchange energy, sometimes called "exact exchange" and E_x^{B88} was presented as the second term in equation 2.42 above.

The parameters of B3LYP are semiempirical (obtained by a linear least squares fit to atomization energies and ionization potentials[61]) and have also been used in the BPW91 hybrid functional [61]. B3LYP was first tested on a set of small molecules and yields very accurate atomization energies, ionization potentials and geometries [61]. Combined with its relative computational efficiency, this the principal reason why it has become the de facto standard quantum chemical method for systems otherwise too expensive for correlated wave function methods but small enough to be able to afford hybrid DFT. The systems treated in this work are of this type.

2.3.6 Dispersion Correction

With hybrid functional methods such as B3LYP, dispersion interactions are not accounted for. Since such interactions are very important in even simple organic molecules (e.g. hydrocarbons with a chain length of C_8) dispersion corrected functionals have found widespread application.

The dispersion-corrected energy is evaluated by adding a dispersion energy to the Kohn-Sham total energy, given here as E_{SCF}. The dispersion-corrected energy is denoted $E_{\mathrm{DFT\text{-}D}}$.

$$E_{\mathrm{DFT\text{-}D}} = E_{\mathrm{SCF}} + E_{\mathrm{D}}. \tag{2.44}$$

The empirical dispersion potential is proportional to the distance between two nuclei $r_{\alpha\beta}^{-6}$. This describes the interaction of two induced dipoles with each other. A function f_{dmp} is used to damp the dispersion potential so that the long range effects are not overestimated.

$$E_{\mathrm{D}} = -s_6 \sum_{\alpha}^{N_\alpha - 1} \sum_{\beta=\alpha+1}^{N_\alpha} \frac{C_6^{\alpha\beta}}{r_{\alpha\beta}^6} f_{dmp}(r_{\alpha\beta}). \tag{2.45}$$

In this approach, the scaling constant s_6 and the damping coefficient $d = 20$ of the damping function (employed to avoid artifacts by adding the dispersion at too short or too great a distance, see eq. 2.46) are empirical. Another parameter that goes into this method is the van der Waals radius which is usually computed

at an ab initio level of theory (Grimme did this by taking the 0.01 a_0^{-3} electron density isocontour value for atoms in their ground state at the ROHF/TZV level of theory[63]). The expression R_r is the sum of the van der Waals radii in the following equation:

$$f_{dmp}(r_{\alpha\beta}) = \frac{1}{1 + e^{-d(r_{\alpha\beta}/R_r - 1)}}. \tag{2.46}$$

The dispersion coefficients $C_6^{\alpha\beta}$ are computed by taking the geometric mean of the atomic $C_6^{\alpha\alpha}$ values which have in turn been evaluated [63] from ionization potential and polarizability calculations by Grimme, using the PBE0 functional [64] as:

$$C_6^{\alpha\beta} = \sqrt{C_6^{\alpha\alpha} C_6^{\beta\beta}}, \tag{2.47}$$

$$C_6^{\alpha\alpha} = 0.05 Q I_p^{\alpha\alpha} \mathfrak{P}^{\alpha\alpha}. \tag{2.48}$$

Here Q is the number of electrons in a full sphere (2, 10, 18, 36 and 54 respectively), $I_p^{\alpha\alpha}$ the ionization potential of atom α and $\mathfrak{P}^{\alpha\alpha}$ the static polarizability of atom α. The constant 0.05 has been fitted and is thus the last "hidden" parameter in this whole approach.

Even more recently, Goerigk and Grimme have devised a novel $E_{\mathrm{D}}^{\mathrm{D3}}$ dispersion correction that includes the orders 6 and 8 (instead of only 6) [65]. It is defined as:

$$E_{\mathrm{D}}^{\mathrm{D3}} = -s_a \frac{1}{2} \sum_{\alpha,\alpha>\beta} \sum_{a=6,8} \frac{C_a^{\alpha\beta}}{r_{\alpha\beta}^a} f_{dmp,a}(r_{\alpha\beta}). \tag{2.49}$$

For details on how the scaling factor s_a and the damping function $f_{dmp,a}(r_{\alpha\beta})$ are to be treated for each order, see reference [65].

2.4 The Broken Symmetry DFT Ansatz

Another disadvantage of DFT methods described thus far is that open shell systems (especially open shell singlets but also higher multiplicities) cannot be treated with the typical one-determinantal Kohn-Sham DFT wave function.

Originally published by Noodleman in 1981 [66], the broken symmetry method leads to a wavefunction that is a weighted average of several Slater determinants. It can be taken to model e.g. antiferromagnetic coupling. The advantage of a broken symmetry wave function is that it is able to describe biradicals or polyradicals without using the much more expensive multiconfigurational self consistent field (MCSCF) procedure. The broken-symmetry wave function can also be reached with any kind of unrestricted SCF procedure, thus UHF or UDFT.

One drawback of broken symmetry wave functions is that they are not eigenfunctions of the $\hat{S}^2$ operator, so $\langle \hat{S}^2 \rangle$ diverges from the values 0 for a singlet, 0.75 for a doublet and so on. In other words, the resulting wave function is

contaminated by a mixture of several spin states. For example, one obtains a linear combination of singlet and triplet with coefficients ${}^1C$ and ${}^3C$:

$$ {}^1|\Psi_{bs}\rangle = {}^1C\,{}^1|\Psi_{pure}\rangle + {}^3C\,{}^3|\Psi_{pure}\rangle, \tag{2.50} $$

where the subscript "pure" will be neglected from now on.

To correct for this spin contamination, Houk and coworkers proposed an approximate method [67], examplified on biradical singlets which have a certain triplet component mixed in. The unrestricted wave function of the triplet usually does not exhibit a large spin contamination. Therefore, the $\langle\hat{S}^2\rangle$ value is taken to be 2.0 and the pure singlet energy ${}^1E$ is then corrected in the following way: One factors in the ${}^1\langle\hat{S}^2\rangle_{bs}$ and the broken symmetry singlet /"pure" triplet gap ${}^1E_{bs} - {}^3E$. This leads to the following expression for ${}^1E$:

$$ {}^1E \approx {}^1E_{bs} + \frac{{}^1\langle\hat{S}^2\rangle_{bs}}{\underbrace{{}^3\langle\hat{S}^2\rangle}_{=2} - {}^1\langle\hat{S}^2\rangle_{bs}}({}^1E_{bs} - {}^3E). \tag{2.51} $$

Likewise, the approximation for polyradicaloids is:

$$ {}^{LS}E \approx {}^{LS}E_{bs} + \frac{{}^{LS}\langle\hat{S}^2\rangle_{bs} - m(m+1)}{{}^{HS}\langle\hat{S}^2\rangle - {}^{LS}\langle\hat{S}^2\rangle_{bs}}({}^{LS}E_{bs} - {}^{HS}E), \tag{2.52} $$

where LS is low spin and HS is high spin and $m(m+1)$ is the exact $\langle\hat{S}^2\rangle$ value.

2.5 Basis Sets

Since the DFT methods used in this work all employ basis sets, it is necessary to understand which basis sets there are and for which purpose they are used. This subsection will focus on the basis sets used in this work in combination with the quantum chemical methods described before. These are primarily the split-valence (Gaussian type) basis sets developed by Pople and co-workers [68, 80], The second part of this subsection will present the two types of effective core potentials used in this work.

2.5.1 Pople Split Valence Basis Sets

Developed by Pople and co-workers [68], this class of split valence basis sets has become a standard for many quantum chemical calculations spanning a large section of the periodic table. The notation is X-YZG(*) (for double ζ basis sets) where X is the number of primitive functions to contract for the core electrons and Y and Z are the numbers of primitive functions to contract for the valence electrons. The * denotes an inclusion of additional polarization functions.

In order to arrive at the contraction scheme, one must first count the number of primitive functions given in the notation. 4-31G, for example amounts to $4+3+1 = 8s$ type functions and $3+1 = 4p$ type functions (both examples are for second-row atoms). These are then contracted to 1 core function

of s symmetry, two valence functions of s symmetry and 2 valence functions of p symmetry (this actually means 6 cartesian basis functions because there are p_x, p_y and p_z orbitals!). This contraction scheme is most frequently written as $(8s4p)/[3s2p]$.

A very common basis set used today for geometry optimizations is denoted 6-31G*. Its contraction scheme can be written as $(4s)/[2s]$ for hydrogen atoms and $(10s4p1d)/[4s2p1d]$ for second-row atoms.

In this work, the 6-31G** basis set is used for geometry optimizations. Its contraction scheme is $(4s1p)/[2s1p]$ for hydrogen atoms and $(10s4p1d)/[3s2p1d]$ for second-row atoms. The 6-31** adds 1 p function to the basis for H atoms.

While 6-31G** works well for H atoms, second and third row atoms, on the transition metal Ru a different basis set is used, involving an effective core potential (ECP). ECPs are discussed in the following subsection.

2.5.2 Effective Core Potentials (ECP)

There are two main reasons to introduce effective core potentials (ECPs) which replace the basis functions of the core electrons: The first reason is the significant reduction of computational effort since the number of basis functions for third-row elements and below in the periodic table becomes very large. The second reason is the inclusion of relativistic effects by quasirelativistic ECPs.

ECPs have to be combined with customized optimized GTO (Gaussian Type Orbital) basis sets for the valence electrons and usually the authors responsible for an ECP have also optimized the corresponding GTO valence basis set.

An ECP is of the general (Gaussian) form:

$$ECP(r) = \sum_k u_k r^{n_k} \exp[-\zeta_k r^2], \tag{2.53}$$

where the coefficients u_k and the exponents ζ_k are characteristic for each ECP and to be determined empirically.

Two types of ECP have been used in this thesis: One is the Stuttgart-Dresden-Bonn pseudopotential [69], as implemented in Gaussian09[70]. The second is the Los Alamos Type ECP [71], as implemented in Jaguar 7.6 [72]. The references cited include all u_k and ζ_k values as well as the respective optimized GTO basis sets. In the case of Ru, 28 core electrons($1s^2 2s^2 2p^6 3s^2 3p^6 3d^{10}$) are included in the respective ECP.

2.6 The Poisson-Boltzmann (PB) Implicit Solvation model

All methods discussed so far are applicable for the gas phase. Since the chemistry we aim at describing in this work takes place in solution, solvation effects must be accounted for in some way. The final subsection of the theory part of this thesis presents the solvation model used.

The PB model is a CDM approach where the solvent is described by the dielectric constant ϵ and the solvation energy is evaluated solely by electrostatic interactions between the solute, resting in a cavity, and the continuum. An extensive review of this field within the context of quantum mechanical calculations has been provided by Tomasi and co-workers [73].

The Poisson-Boltzmann model rests on the Poisson equation:

$$\epsilon\nabla^2\varphi(\vec{r}) = -\rho(\vec{r}). \tag{2.54}$$

Here φ is the electrostatic potential and ρ the charge density. In principle, ϵ may of course also vary but for our intents and purposes (aqueous solutions) we assume it to be constant. By distinguishing between the charge density of the solute $\rho_S(\vec{r})$ and the charge density of the ions in solution which may be described by a Boltzmann distribution we arrive at the non-linear Poisson-Boltzmann equation:

$$\epsilon\nabla^2\varphi(\vec{r}) = -\rho_S(\vec{r}) - \sum_i c_i^\infty z_i e \cdot \exp\left[-\frac{z_i e\varphi(\vec{r})}{\mathrm{k_B}\Theta}\right]\lambda(\vec{r}). \tag{2.55}$$

In this equation, we sum up over all ions i with c_i^∞ being the bulk concentration of ion i and $\lambda(\vec{r})$ characterizes the acessibility of a point in space $\vec{r}$ to ions. Following a series expansion where only the linear term is taken, one obtains a linear equation (2.56) . Of course, this only works when the potential is small what can safely be assumed for dilute solutions.

$$\begin{aligned} \epsilon\nabla^2\varphi(\vec{r}) =& -\rho_S(\vec{r}) + k^2\varphi(\vec{r})\lambda(\vec{r}), \\ \text{with } k^2 =& \frac{\sum_i c_i^\infty z_i^2 e^2}{\mathrm{k_B}\Theta}. \end{aligned} \tag{2.56}$$

In this equation, $k^2$is closely related to the Debye screening constant κ making the Poisson-Boltzmann model to be linked to Debye-Hückel theory[74].

For quantum mechanical continuum dielectric considerations, the Poisson-Boltzmann model has been implemented as a numerical scheme by using finite elements (e.g. denoted as "PBF" in Jaguar 7.6). The computational procedure is a self-consistent one. First, the electrostatic potential of the solute in gas phase is computed using the gas phase wave function. The potential is then represented on a grid (on and near the surface of the solute). This potential is subjected to the Poisson-Boltzmann equation, yielding an (external) density which is in turn incorporated in the Hamiltonian in the potential energy part.

The Poisson-Boltzmann model was originally developed more than 100 years ago by Gouy and Chapman independently from each other [75]. An overview of the method, concerning especially its application in biomolecular implicit solvation simulations is given in reference [76]. An additional pioneering study on the subject of quantum chemical Poisson-Boltzmann calculations is provided in reference [77]. Therein, the authors describe how the electrostatic potential, fitted from quantum chemical calculations, is used to compute the reaction field.

3 Computational Details

This section has two parts. The first, 3.1, will describe the methods for geometry optimizations, single-point energies, free energy and solvation corrections used for all systems. The second, 3.2, will present the SC-UB3LYP method for systems with spin contamination.

3.1 Methods for all systems

Initial input geometries were generated using Avogadro 1.0.3 [78]. Molecules were drawn using Avogadro's standard drawing tools. These preliminary geometries were subjected to 500 steps of steepest descent molecular mechanics pre-optimization, using Avogadro's universal force field (UFF)[79]. The preoptimized structures were then used as input geometries for subsequent quantum chemical calculations.

Geometry optimizations, frequency calculations for the gas phase were done by using the Gaussian 09 suite of programs [70]. The calculations were performed with the B3LYP[61, 62] functional as implemented therein. The basis sets[68, 80, 81] were 6-31G(d,p) for hydrogen and 6-31G(d) for second and third row elements for the optimization and frequency calculations. The Stuttgart-Dresden-Bonn pseudopotential with an $(8s7p6d)/[6s5p3d]$ basis set (Gaussian keyword: MWB28) was used for the ruthenium center[69] in these calculations. This combination of basis sets will be referred to as "B1".

For single point energy calculations a larger basis set[82] was chosen. For hydrogen atoms, the 6-311G(d,p) basis was used. For second row elements the 6-311+G(d) basis and for third row elements (S and Cl) the 6-311+G(3d) basis sets were chosen[83]. Moreover, three additional sets of functions ($2f$ and $1g$) were used at the Ru center in combination with the same effective core potential (ECP) as before, according to literature [84]. This combination of basis sets will be referred to as "B2".

Zero-point-corrections and corrections for thermal energies were taken from frequency calculations at the B3LYP/B1 level of theory since no optimization took place at the B3LYP/B2 level of theory. Reaction energies were calculated as follows:

$$\Delta_R E = \sum E_{\text{products}} - \sum E_{\text{reactants}} \tag{3.1}$$

$$\Delta_R G = \sum G_{\text{corr, products}} - \sum G_{\text{corr, reactants}} \tag{3.2}$$

where G_{corr} denotes the Gibbs free energy of the molecule in question (calculated by adding the corrections mentioned to the single point energy values attained at the B3LYP/B2 level).

Minima and transition state geometries were verified by calculating the harmonic frequencies at the B3LYP/B1 level of theory. A local minimum has only normal modes with positive eigenvalues. A transition state represents a saddle point on the potential energy surface of a molecule and has therefore exactly

one imaginary frequency pointing along the reaction coordinate connecting two local minima.

Jaguar 8.0 [72] was used to compute solvation free energies G_{PBF}. Preoptimized gas phase geometries were given as input structures. Solvation energies were obtained using the Poisson-Boltzmann solver (PBF) program within Jaguar 7.6, for theory see section 2.6. The solvent was water; accordingly, the continuum dielectric constant $\varepsilon_{\mathrm{H_2O}}$ was set tp 80.370 (for 20°C). [85] The basis set for computing the solvent correction was B1 without the ECP, which was exchanged for a Los Alamos type [71] ECP (with corresponding valence basis functions for Ru). The basis set is implemented in Jaguar as "LACVP**". This protocol of obtaining the solvent correction was originally reported in reference [86] and has shown to be one of the most accurate protocols tested for Ru anticancer compounds.

The reaction free energy in solution, $\Delta_R G_{\mathrm{sol}}$ was computed by adding the PBF solvation corrections to the corrected gas phase free energies obtained previously:

$$\begin{aligned}\Delta_R G_{\mathrm{sol}} = &\sum (G_{\mathrm{corr,\ \ products}} + G_{\mathrm{PBF,\ products}}) - \\ &\sum (G_{\mathrm{corr,\ \ \ reactants}} + G_{\mathrm{PBF,\ reactants}}).\end{aligned} \tag{3.3}$$

For every species reported with $S > 0$ the expectation value for $\hat{S}^2$ was inspected. The method employed to calculate species with multiplicities different from 1 is unrestricted B3LYP (UB3LYP). This was done in order to make sure that the $\langle \hat{S}^2 \rangle$ value did not differ more than 10 % from $m(m+1)$ which has been proposed as a rule of thumb [87], recall section 2.4.

Where dispersion-corrected DFT was used, the method will be referred to as B3LYP-D [63]. The type of dispersion correction employed is the pairwise post-SCF sixth order-only B3LYP-D [63] which is implemented in Gaussian09 [70]. For the B3LYP functional, the s_6 scaling factor is equal to 1.05 and the damping coefficient is $d = 20$.The B3LYP-D method has been used in this thesis to perform geometry optimization and frequency calculations using the B1 basis set. Single-point energies are obtained at the B3LYP-D/B2//B1 level of theory and the solvation correction is added again at the B3LYP/LACVP** level, taking the geometries optimized at B3LYP/B1 level of theory. Taking a solvation correction without dispersion correction is possible because the dispersion correction used does not depend on the density and the solvation correction is only a relative energy added at the end.

All calculations with Gaussian09 were carried out on a Linux cluster with the following specifications: 6 compute nodes with Intel®Xeon®CPU E5645 @ 2.40 GHz double hexacore machines with 48 GB RAM each.

3.2 Method for Systems with Spin Contamination

It is well-known that one-determinantal methods fail at describing dissociation processes (e.g the homolytic dissociations of H_2 [88]). One possible way to treat this problem is using the Broken Symmetry ansatz, recall section 2.4. This section provides justification for the broken symmetry and spin contamination correction procedures used in this thesis. The example displayed here is the homolytic dissociation of H_2O_2. H_2O_2 is the perfect model system for this work because the Fenton-like reactions treated in section 4.2 will adress exactly this process.

In order to compare restricted and unrestricted/broken symmetry solutions for a wave function the case study of H_2O_2 dissociation is taken (a very similar case study on the H_2 molecule has been done by Schlegel and co-workers[88]). The procedure is the following: The geometry of H_2O_2 was optimized at the B3LYP/B1 level of theory (equilibrium distance 1.46 Å). A rigid PES scan was then carried out, keeping all internal coordinates frozen except the O–O bond distance. This scan was performed at the B3LYP/6-311+G(d,p) level of theory. with Gaussian09 for the following variants:

1. Restricted B3LYP - singlet (RB3LYP)
2. Unrestricted B3LYP (broken symmetry) - singlet (BS-UB3LYP)
3. Unrestricted B3LYP (broken symmetry) - singlet with spin contamination correction [67] (SC-UB3LYP)
4. Unrestricted B3LYP - triplet (UB3LYP-triplet)

The results of this scan are given in Figure 3.1.

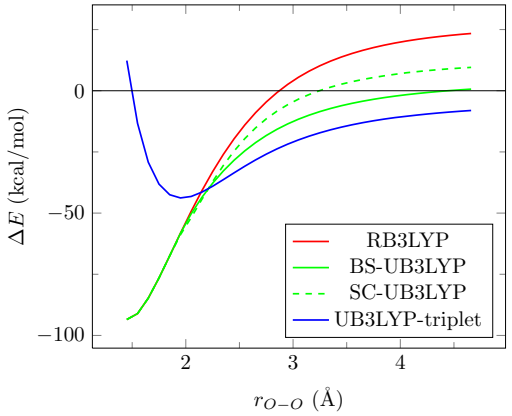

(a)

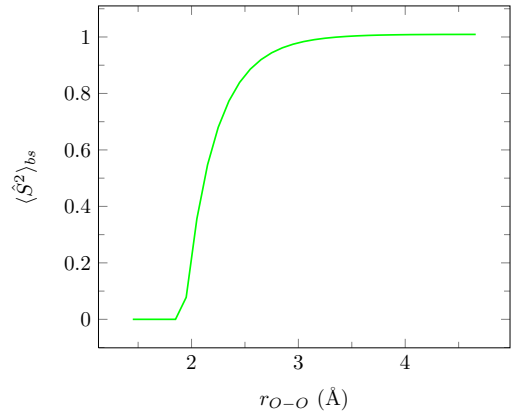

(b)

Figure 3.1: (a) Relative energies scanned along the O–O distance in H_2O_2.The reference is 2 OH radicals, calculated at infinite distance. (b) Expectation value of the $\hat{S}^2$ operator (UB3LYP/6-311+G(d,p)) on the BS-UB3LYP wave function along the O–O distance.

Clearly, the restricted singlet wave function gives the wrong asymptotic behavior and this is a well known failure of one-determinant methods, see Figure 3.1a. With the broken symmetry wave function, the trend at long distances is correct and the energy of the broken symmetry singlet subtends the 0 line for a large separation of the two OH monomers.

The curve given in Figure 3.1 (b) shows that the expectation value of $\hat{S}^2$ is 1 at the end of the scan which corresponds to a 50/50 singlet/triplet mixture. It also pinpoints the O–O distance where the RB3LYP wave function becomes unstable (1.80 Å).

The bottom line of the considerations above is that in order to describe a ho-

molytic peroxide bond cleavage, an unrestricted method (UB3LYP in this case) has to be employed, which may yield a broken symmetry solution to the given problem. Hydrogen peroxide will serve as a ligand in the following sections and its homolytic dissociation may be facilitated by the Ru complex, see below.

Despite the unrealistic asymptotic behavior that SC-UB3LYP produced in the H_2O_2 scan above, the spin contamination correction procedure proposed by Yamaguchi et al. [67] yields a good approximation to singlet-triplet gaps in two model species. The data on this subject are given in Table 1.

Table 1: Broken Symmetry spin correction data: Singlet-triplet energy gaps (UB3LYP/B2) for model systems. A positive sign denotes a triplet ground state. All energies are given in kcal/mol. The best estimate refers to a calculated value. The method used is given in the table.

system	BS-UB3LYP	$\left\langle \hat{S}^2 \right\rangle_{\text{bs}}$	SC-UB3LYP	expt.	best estimate
CH_2	6.9	0.57	9.7	9.1 [89]	9.0 [90] (CASSCF-SOCI)
NH_2^+	20.5	0.75	32.7	30.1[91]	29.9[92] (MRCI)

Since SC-UB3LYP method performs well for the singlet-triplet splitting in methylene (CH_2) and amidogen (NH_2^+), its use is justified for transition state (TS) species with an elongated O–O bond distance of > 1.8 Å, in order to arrive at a spin contamination-corrected energy for said structures.

4 Results and Discussion

In this section the main findings of this thesis will be presented. Section 4.1 will deal with the localization of local minima, with respect to torsions around the Ru–N bond. The H_2O_2 dissociation in the vicinity of Ru complexes will be discussed together with the heterolytic H_2O_2 cleavage in section 4.2. These processes may be summarized under the term "Fenton-like reactions". Finally, with the insights gained from the calculations presented in section 4.2, results on possible follow-up reactions will be presented in sections 4.3 and 4.4.

4.1 Conformational Analysis Examplified by KP1019 Anion Rotamers

The B3LYP method used in this work yields geometries comparable to the experimental structures of KP1019, see Table A1 in the appendix. This means that the B3LYP method is a good tool to explore the PES of KP1019 and similar molecules derived from KP1019.

Molecules with a large number of degrees of freedom often have many local minima in their PES. Therefore, the first general consideration regarding ruthenium compound KP1019 is the energy profile of the rotation around the Ru–N bond in both oxidation states Ru^{II} and Ru^{III}, see Figures 4.1 and4.2a.

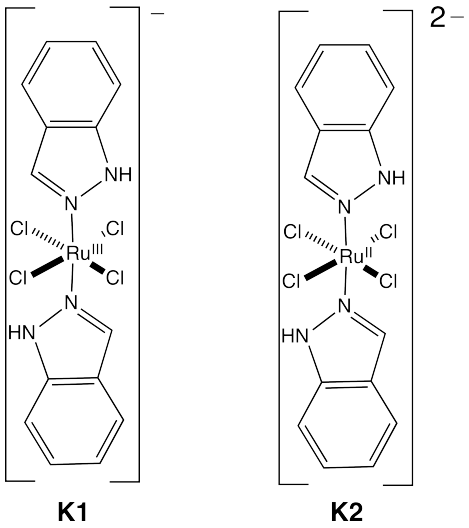

K1 **K2**

Figure 4.1: The KP1019 anion in Ru^{III} (**K1**) and Ru^{II} (**K2**) forms

.

All of the following calculations were performed with the KP1019 anion in its *trans*-$[Ru^{III}Cl_4(ind)_2]^-$(**K1**) and *trans*-$[Ru^{II}Cl_4(ind)_2]^{2-}$(**K2**) stereoisomers. Firstly, **K1** and **K2** were optimized with a dihedral angle of $\phi = 0°$, at the B3LYP/B1 level of theory. From this starting point, a rigid potential energy surface scan was carried out, incrementally varying the torsion angle ϕ, defined as the dihedral angle between the two N–N bonds of **K1** and **K2** (see Figure 4.2a) in 18 steps by 10 °. The result is presented in Figure 4.2b. The other

half-rotation must be identical for symmetry considerations. The energy was set to zero arbitrarily at $\phi = 0°$ for both **K1** and **K2**.

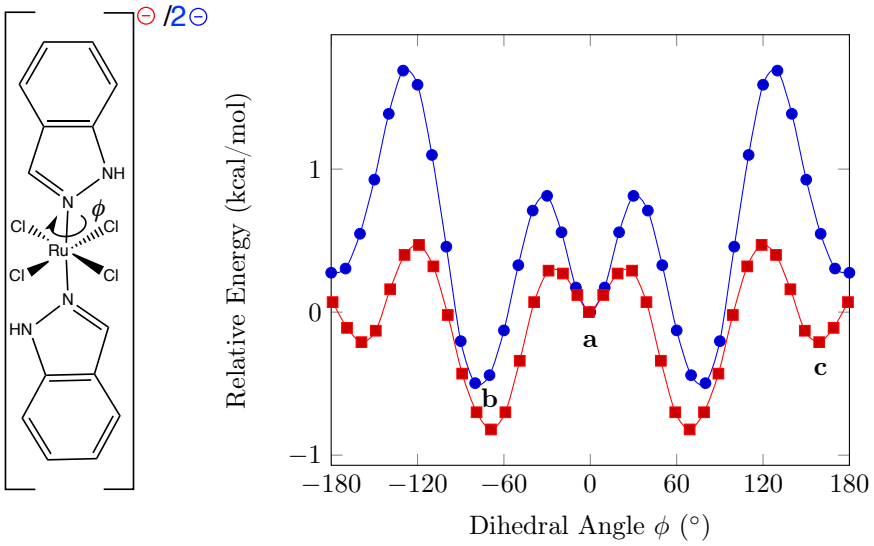

(a) (b)

.

Figure 4.2: Display of the torsional angle ϕ in the KP1019 anion (a); Rigid PES scan (b): Relative energy *in vacuo* (B3LYP/B1) along torsion angle ϕ of *trans*-$[Ru^{III}Cl_4(ind)_2]^-$ (**K1**) (■) and *trans*-$[Ru^{II}Cl_4(ind)_2]^{2-}$ (**K2**) (•). The letters a, b and c indicate estimates of local minima. The relaxed structures for **K1** and **K2** can be found in Figures 4.3 and 4.4, respectively.

The calculations indicate three minima on the torsional potential energy surface close to $\phi = 0°$, $\phi = 90°$ and $\phi = 180°$ for **K2** and similarly, for **K1**. Based on this hypothesis, geometry optimizations and frequency calculations were carried out for these values of ϕ for both **K1** and **K2**. The minima are quite similar in energy, as is shown in Table 2, and expected from Figure 4.2b. An approximation of the rotational barrier (1.3 kcal/mol for **K1** and 2.5 kcal/mol for **K2**) is given by the data presented in Figure 4.2b. Figures 4.3 and 4.4 show the three rotamer minimum structures obtained for **K1** and **K2**, respectively .

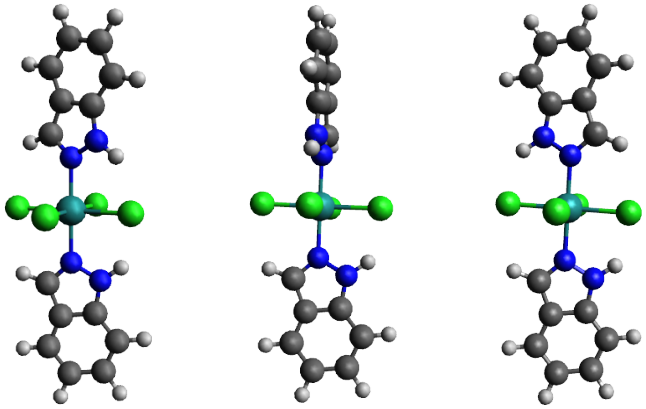

$\phi = -21.4°$ **K1a** $\phi = -93.6°$ **K1b** $\phi = 159.1°$ **K1c**

Figure 4.3: Optimized structures (B3LYP/B1) of local minima of *trans*-$[Ru^{III}Cl_4(ind)_2]^-$(**K1**)

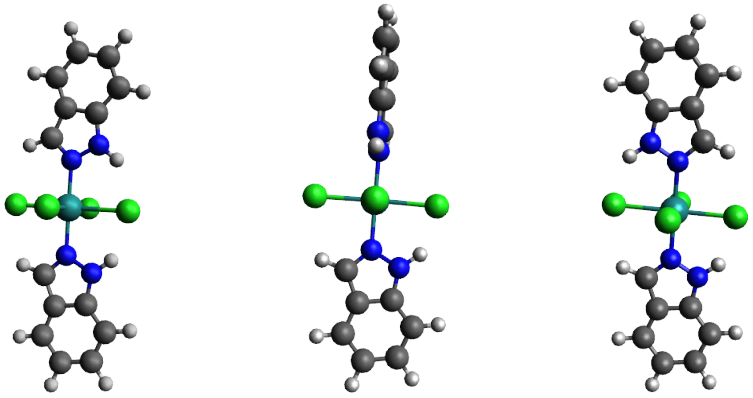

$\phi = 0.2°$ **K2a** $\phi = -96.3°$ **K2b** $\phi = 179.8°$ **K2c**

Figure 4.4: Optimized structures (B3LYP/B1) of local minima of *trans*-$[Ru^{II}Cl_4(ind)_2]^{2-}$(**K2**)

Table 2: Relative ground state energies (B3LYP/B2//B1) of optimized KP1019 rotamers given in kcal/mol. G values include the B3LYP/B1 free energy correction and G_{sol} include the free energy and solvent corrections

	ϕ	E	G	G_{sol}
K1a	$-21.4°$	0.0	0.0	0.0
K1b	$-93.6°$	-1.6	-2.9	-1.8
K1c	$159.1°$	-0.6	-2.2	-2.0
K2a	$0.2°$	0.0	0.0	0.0
K2b	$-96.3°$	-2.1	-1.3	$+0.3$
K2c	$179.8°$	-1.1	-1.8	-0.9

Table 2 shows that the global minimum *in vacuo* for **K1** and **K2** have a dihedral angle ϕ of -93.6° and 179.8°, respectively. Adding all corrections as described above, *trans*-$[\mathrm{Ru^{III}Cl_4(ind)_2}]^-$ is predicted to most likely occur at $\phi = 159.1°$ (**K1c**) in solution . This "twisted" conformation is consistent with the crystal structure of the $\mathrm{P(Ph)_4^+}$ salt of *trans*-$[\mathrm{Ru^{III}Cl_4(ind)_2}]^-$[93].

However since the difference between the local minima is only 2.0 kcal/mol, the torsional minima are not experimentally distinguishable. The torsional barrier height (estimated at 1.3 kcal/mol for **K1** and 2.5 kcal/mol for **K2**) is so low that the indazole rings may be considered to rotate freely around the Ru–N bonds.

Nonetheless, since one has to choose one of the conformational isomers for the further exploration of the reactive pathways of KP1019 derivative compounds, the search for local minima (with regard to the torsion around the Ru–N bonds) was carried out for KP1019 derivative structures (denoted always by the prefix **K** and sequential numbering; for structures, see Figure 4.5). This was done in order to identify the most probable reaction pathway. The local minimum with the lowest absolute energy (E, because the optimization was with respect to E) was then taken to be the reactant in every respective reaction.[3]

4.2 Fenton-like Reactions: Heterolytic vs. Homolytic Peroxide Bond Cleavage

Fenton-like reactions discussed in section 1.4.2 were calculated for KP1019 and NAMI-A derivatives, starting at both $\mathrm{Ru^{II}}$ and $\mathrm{Ru^{III}}$ oxidation states. A thorough analysis on rotamers as discussed in section 4.1 was carried out on each structure with two indazole ligands, with the structures shown in the figures below being the ones with the lowest calculated energies. The ground state of KP1019, NAMI-A and derivatives thereof is generally the low spin state (see reference [94], section 9), thus $S = 0$ for d^6 ($\mathrm{Ru^{II}}$) systems and $S = \frac{1}{2}$ for d^5 ($\mathrm{Ru^{III}}$) systems.

[3] In compounds with reduced symmetry the two torsions of the N-heterocyclic rings are not equivalent and both torsions were considered in increments of 90° , respectively.

Figure 4.5 displays all structures treated in this part of the thesis. The **K** compounds are all KP1019 derivatives and the **N** compounds are NAMI-A derivatives. For simplicity, in all the following reaction schemes (beginning with Figure 4.6), the following labels for axial ligands are used: For **K** compounds L_1=L_2=ind. For **N** compounds, L_1=im and L_2=S-dmso.

In the following next sections, 4.2.1, 4.2.2 and 4.2.3, we will go through the reactions connecting the compounds shown in Figure 4.5 step by step. At the end of section 4.2.3, the global summary will be provided in a table (Table 3) contaning all relative E, G and G_{sol} values and a diagram , visualizing the data (Figure 4.11).

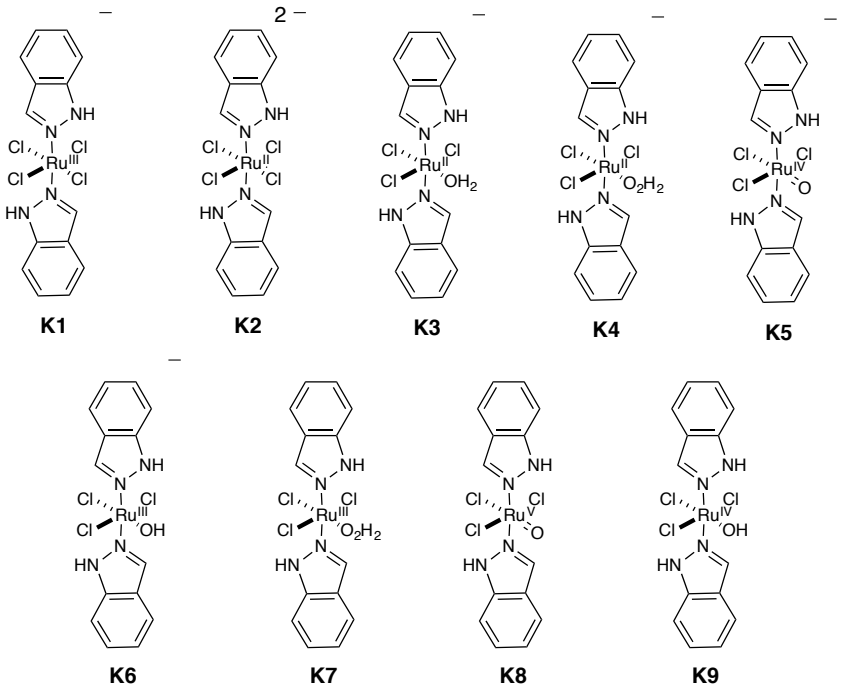

(a) All KP1019 derivative structures treated in section 4.2.

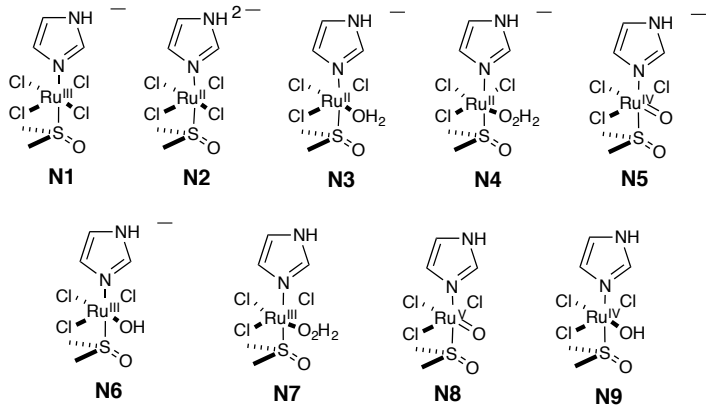

(b) All NAMI-A derivative strucutres treated in section 4.2.

Figure 4.5: Global overview of KP1019 and NAMI-A derivative structures in this section. From now on, the indazole ligands are denoted by "ind", the imidazoles by "im" and S-coordinated DMSO by "S-dmso".

4.2.1 Prelude: Aquation and Perhydrolysis of KP1019 and NAMI-A derivatives

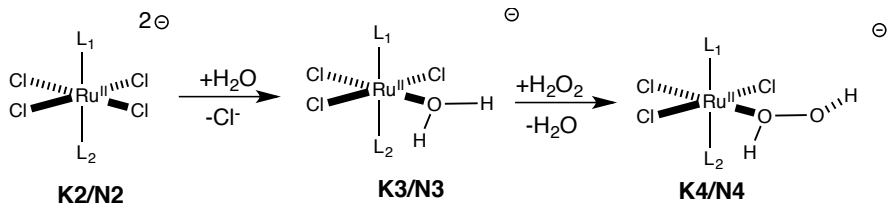

Figure 4.6: Aquation/perhydrolysis of KP1019 and NAMI-A derivatives.

KP1019 and NAMI-A are readily reducible and undergo equatorial ligand exchange in vitro (NAMI-A, [18]) and (a very recent discovery) in target tissue (KP1019, [95]), yielding the monoaquated species (**K3**/**N3**). Our calculations show that it is thermodynamically plausible to exchange one water ligand against H_2O_2, which gives the monohydroperoxide derivatives **K4**/**N4**, see Figure 4.6.

In order to clarify whether the (Ru^{II}) monoaqua (**K3**/**N3**) and monohydroperoxide (**K4**/**N4**) compounds have a similar Ru–O coordination, the Ru–O distance has to be investigated. For **K3**/**N3**, this value is 2.22/2.24 Å. For **K4**/**N4**, it amounts to 2.15/2.20 Å, respectively. Therefore, binding modes of H_2O and H_2O_2 are similar, as they have the same donor atom, albeit in a different oxidation state.

The calculated $\Delta_R G_{\mathrm{sol}}$ values (B3LYP/B2//B1, including all corrections) for **K3**+$\mathbf{H_2O_2}$→**K4**+$\mathbf{H_2O}$ and **N3**+$\mathbf{H_2O_2}$ → **N4**+$\mathbf{H_2O}$ are -0.6 and +0.7 kcal/mol, respectively. These results shows that perhydrolysis of **K3**/**N3** compounds (that have been characterized experimentally) is thermodynamically possible. After perhydrolysis, the inner-sphere oxidation of Ru compounds by H_2O_2 is to be investigated.

Therefore, the Fenton-like reactions for *mer,trans*-$[Ru^{II}Cl_3(ind)_2(O_2H_2)]^-$ **(K4)** and *mer*-$[Ru^{II}Cl_3(im)(O_2H_2)(S{-}dmso)]^-$ **(N4)**[4], have been treated computationally and the results are shown section 4.2.2.

Additionally, since the same aquation/perhydrolysis process might happen in the Ru^{III} oxidation state as well, the oxidation of the monohydroperoxide **K7**/**N7** compounds by H_2O_2 has also been calculated and the findings are presented in section 4.2.3.

[4]For all **N** compounds, the *mer*- prefix refers to the three chlorido ligands. The other ligands are given in alphabetical order according their donor atoms, with the imidazole and the S-dmso ligand always being in *trans*- position to each other, like in the parent compound NAMI-A.

4.2.2 Oxidation of Ru^{2+} Compounds

As discussed in section 1.4.2, there are two proposals on the mechanism of the Fenton reaction, equivalent to homolytic and heterolytic peroxide bond cleavages. This work contains calculations on both suggested pathways, focussing at first on the heterolytic pathway, then on the homolytic one. As each pathway will be discussed step by step, there will be a figure containing the optimized geometries and the ΔG_{sol} values (because the values for ΔG_{sol} are experimentally accessible) for each pathway. The discussion of the geometries and the energies will be in the text.

Figure 4.7 shows a heterolytic O–O bond cleavage model mechanism for the oxidation of Ru^{II} to [Ru^{IV}=O] ("ruthenyl") by H_2O_2. In this process, the O–O bond length of the reactant **(K4/N4)** is elongated and the proximal proton is abstracted in a concerted, two electron process *via* the transition state (TS **K4-K5** and TS **N4-N5**), yielding the ruthenyl species (**K5/N5**) and H_2O.

The optimized geometries in Figure 4.7 illustrate that the O–O bond length is slightly elongated already in the **K4/N4** structure (1.48/1.47 Å vs. 1.46 Å [B3LYP/B1] equilibrium bond length in free H_2O_2) and that the Ru–O distance decreases along the reaction coordinate. Among the Ru–Cl and Ru–N distances the Ru–Cl distance of the Cl ligand in *trans*-position to the proximal O undergoes the greatest change. It is elongated from 2.45/2.44 Å in **K4/N4** to 2.57/2.55 Å in **K5/N5**. The calculated Ru–O bond distances in the **K5/N5** compounds of 1.78 Å compare well to a recently reported ruthenyl compound [96] where for a hexacoordinated Ru^{IV}=O system with a first coordination sphere of 5 N atoms and a chloride anion the authors have reported a Ru–O distance of 1.77 Å.

The heterolytic peroxide bond cleavage mechanism is both thermodynamically and kinetically very favorable. However, there is a problem with the relative energies for TS **K4-K5** and TS **N4-N5** which are almost zero or even negative with respect to **K4/N4**.[5] The only conclusion that can be drawn here is that while the activation barrier is not quantifiable by the used method it must nonetheless be very low. More importantly, thermodynamically, the reaction is predicted to be very favorable with the equilibrium shifted overwhelmingly to the right side at -64.3 (**K5**+H_2O) and -58.4 (**N5**+H_2O) kcal/mol respectively. These energies are for the electronic ground states of compounds **K5/N5**, which are both triplet states.

The homolytic peroxide bond cleavage at the **K4/N4** compounds may be treated as a peroxide dissociation. Details on this mechanism are given in Figure 4.8.

[5] Negative TS energies point to a failure of the method. The geometries were optimized on a different level (B3LYP/B1) than the single-point energy was taken (B3LYP/B2) and the implicit assumption is that the PES does not change with the change in basis (B1 to B2). However, exactly this appears to have happened for TS **K4-K5** and TS **N4-N5** (differential correlation). A negative activation barrier is unphysical, and therefore the negative value for TS **K4-K5** has been set to 0.0 kcal/mol.

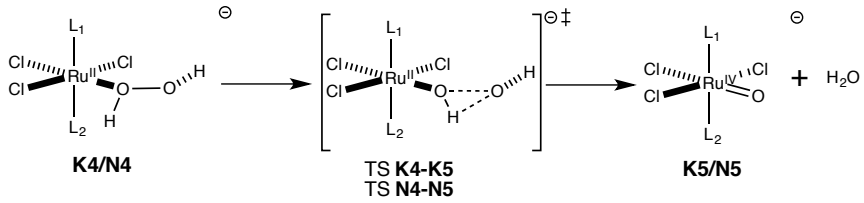

(a) Scheme of the mechanism. For **K** compounds L_1=L_2=ind. For **N** compounds, L_1=im and L_2=S-dmso.

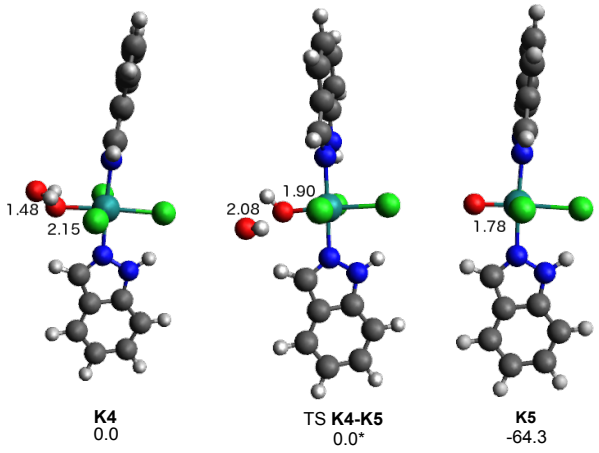

(b) Optimized structures (B3LYP/B1) for KP1019 derivatives. Ru–O and O–O distances are given in Å. Relative free energies in aqueous solution (B3LYP/B2//B1, including all corrections) are given in kcal/mol. * -1.9 kcal/mol set to 0.0, see text.

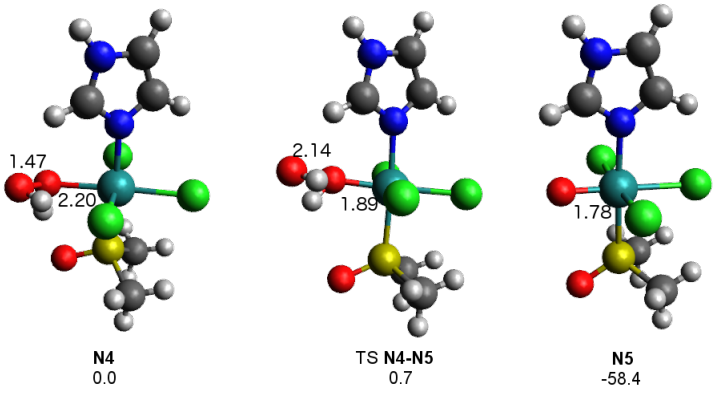

(c) Optimized structures (B3LYP/B1) for NAMI-A derivatives. Ru–O and O–O distances are given in Å. Relative free energies in aqueous solution (B3LYP/B2//B1, including all corrections) are given in kcal/mol.

Figure 4.7: Details on the heterolytic peroxide bond cleavage mechanism for Ru^{II} compounds .

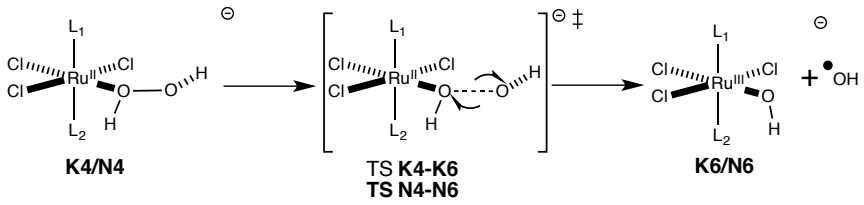

(a) Scheme of the mechanism. For **K** compounds L_1=L_2=ind. For **N** compounds, L_1=im and L_2=S-dmso.

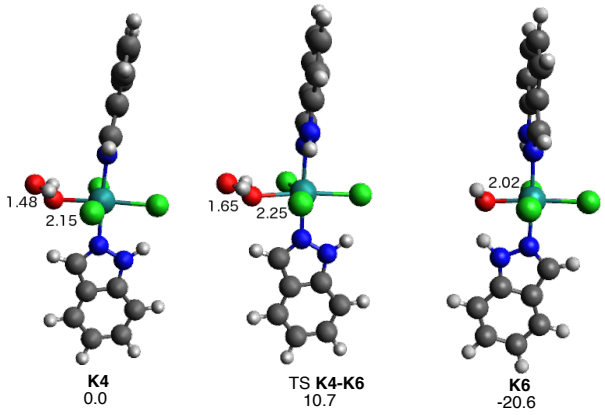

(b) Optimized structures (B3LYP/B1) for KP1019 derivatives. Ru–O and O–O distances are given in Å. Relative free energies in aqueous solution (B3LYP/B2//B1, including all corrections) are given in kcal/mol.

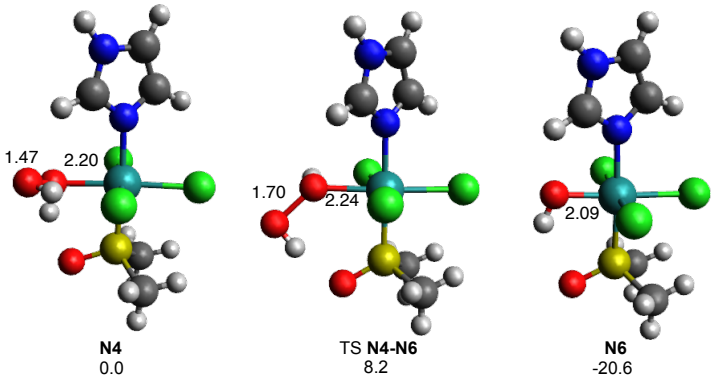

(c) Optimized structures (B3LYP/B1) for NAMI-A derivatives. Ru–O and O–O distances are given in Å. Relative free energies in aqueous solution (B3LYP/B2//B1, including all corrections) are given in kcal/mol.

Figure 4.8: Details on the homolytic peroxide bond cleavage mechanism for Ru^{II} compounds.

Like in the case of the heterolytic peroxide bond cleavage, the O–O distance increases along the homolytic cleavage reaction coordinate. However, the O–O distances in TS **K4-K6** and TS **N4-N6** are shorter than in TS **K4-K5** and TS **N4-N5**: 1.65/1.70 Å for TS **K4-K6**/TS **N4-N6**. The Ru–O distances in the **K6**/**N6** (monohydroxido Ru^{III} compounds) are 2.02 and 2.09 Å, respectively.

The TS energies presented in Figure 4.8 have been calculated by the SC-UB3LYP method of section 3.2. First, the transition state for the homolytic O–O bond dissociation (TS **K3**/**N3-K5**/**N5**) was located on the triplet PES. Then, the symmetry was broken at the attained geometry and the method described in section 3.2 was employed. The spin contamination correction in this case was minor because the $\langle \hat{S}^2 \rangle$ value was close to 0 ($^1\langle \hat{S}^2 \rangle = 0$). After the approximation of the pure singlet energy, the free energy and solvent corrections were added. These calculations show that the barrier for the homolytic process is between 8.2 and 10.7 kcal/mol for the 2 sets of compounds treated, with $\Delta_R G_{\text{sol}} = -20.6$ kcal/mol for both cases.

Summarizing the findings presented in figures 4.7 and 4.8, the heterolytic, concerted, two-electron reactive pathway is predicted to be the dominant one. It is also thermodynamically favored for both sets of compounds tested, (pertaining to derivatives of anticancer drugs KP1019 and NAMI-A). Therefore, the rise of a ruthenyl species by H_2O_2-dependent oxidation of Ru^{II} compounds is hereby proposed.

4.2.3 Oxidation of Ru^{3+} Compounds

It is possible that H_2O_2 can also oxidize Ru^{III} compounds **K7** and **N7** see optimized geometries in Figures 4.9 and 4.10 below. Analogously to the previous section the heterolytic path with a Ru^{V} compound as the product will be investigated first, followed by the homolytic peroxide bond cleavage reactive pathway.

The products formed by the heterolytic pathway are the oxidation of Ru^{III} compounds are **K8** and **N8** and water. The details are given in Figure 4.9.

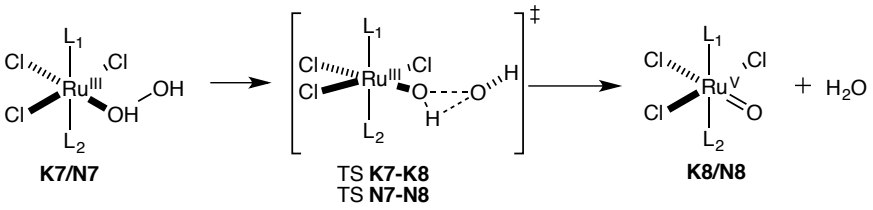

(a) Scheme of the mechanism.

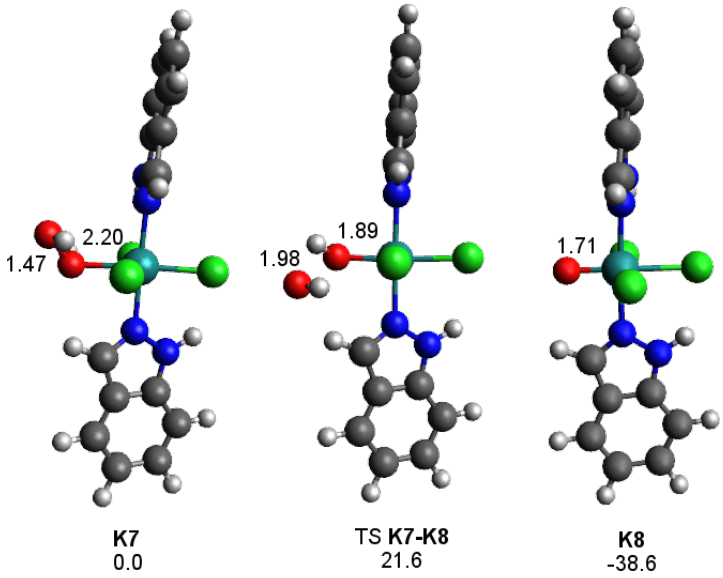

(b) Optimized structures (B3LYP/B1) for KP1019 derivatives. Ru–O and O–O distances are given in Å. Relative free energies in aqueous solution (B3LYP/B2//B1, including all corrections) are given in kcal/mol.

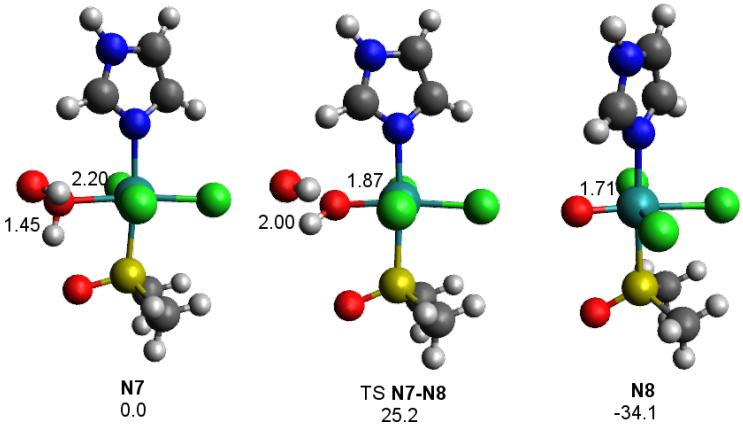

(c) Optimized structures (B3LYP/B1) for NAMI-A derivatives. Ru–O and O–O distances are given in Å. Relative free energies in aqueous solution (B3LYP/B2//B1, including all corrections) are given in kcal/mol.

Figure 4.9: Details on the heterolytic peroxide bond cleavage mechanism for Ru^{III} compounds.

The optimized geometries along the heterolytic O–O bond cleavage reaction coordinate for Ru^{III} compounds show an elongation of the O–O distance to 1.98 (TS **K7-K8**) and 2.00 (TS **N7-N8**) Å similarly to the analogous reaction for Ru^{II} compounds discussed above. The Ru–O bond distance in the Ru^{V} **K8**/**N8** compounds is shorter than in the Ru^{IV} compounds **K5**/**N5**. While there has been evidence of Ru^{V} compounds presented in literature (see reference [97] for an extensive overview), the calculated Ru–O bond length of 1.71 Å cannot be compared to any experimental structure (with similar ligands) to date. However, a shorter [Ru^{V}=O] bond distance with a higher metal oxidation state in comparison with [Ru^{IV}=O] is plausible for the **K8**/**N8** and **K5**/**N5** species. This is based on the experimental findings on Ru^{V} oxo compounds reported in reference [97].

The activation barriers for TS **K7-K8** and TS **N7-N8** are surprisingly very high ($\Delta G^{\ddagger}_{sol}$> 20 kcal/mol), especially when compared to the heterolytic peroxide bond cleavage mechanism at Ru^{II} compounds discussed before. The **K8**/**N8** compounds with a formal oxidation state of +5 are, however, stable. Nevertheless, because of the extent of the activation barrier, the heterolytic H_2O_2 bond cleavage process is deemed unlikely for Ru^{III} compounds because of the extent of the activation barrier.

The results of the calculations on the homolytic O–O bond cleavage process at the **K7**/**N7** compounds, are shown in figure 4.10. Along the homolytic peroxide bond cleavage mechanism for the **K7**/**N7** compounds, the O–O bond distance is elongated from 1.45/1.47 Å to 1.84 (TS **K7-K9**) and 1.91 (TS **N7-N9**) Å. In the resultant **K9**/**N9** compounds, the Ru–O distance is shortened to 1.92 (**K9**) and 1.90 (**N9**) Å. The **K9**/**N9** compounds are Ru^{IV} compounds.

The doublet transition states (TS **K7-K9** and TS **N7-N9**) attained with the UB3LYP formalism show high spin contamination with the $\langle \hat{S}^2 \rangle$ values at 1.26 (TS **K7-K9**) and 1.35 (TS **N7-N9**). This means that the transition state structure for the oxidation of Ru^{III} compounds has a dissociating OH radical fragment. The computed Mulliken spin densities for the distal oxygen atoms (B3LYP/B2) are -0.56 (TS **K7-K9**) and -0.65 (TS **N7-N9**), which points to an antiferromagnetically coupled OH radical in the TS structures, see Figure 4.10. The barrier heights of 3.1 (TS **K7-K9**) and 6.5 (TS **N7-N9**) kcal/mol are different for the **K** and **N** compounds, with the **K7** compound being more easily oxidized than the **N7** compound. The products of the reaction (the hydroxyl radical and the hydroxo Ru^{IV} compound) have been calculated at their respective triplet and a doublet (OH radical) ground states at infinite separation. The computed overall reaction free energy in solution is slightly negative in both cases.

From these results it can be concluded that Ru^{III} compounds can be oxidized by H_2O_2, this time in a homolytic peroxide bond cleavage process, provided the ligand exchange preceding the oxidation reactions is sufficiently fast, yielding a hydroxo-Ru^{IV} species and a highly reactive hydroxyl radical, with compound **K7** exhibiting a lower barrier height and more favorable thermodynamics than **N7**.

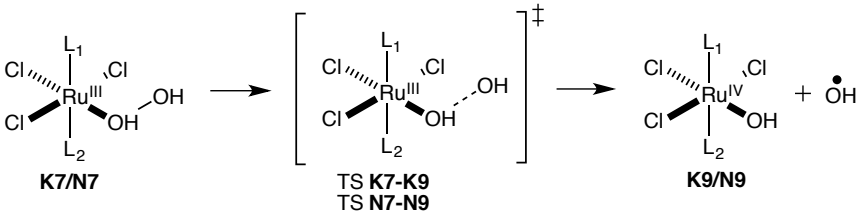

(a) Scheme of the mechanism.

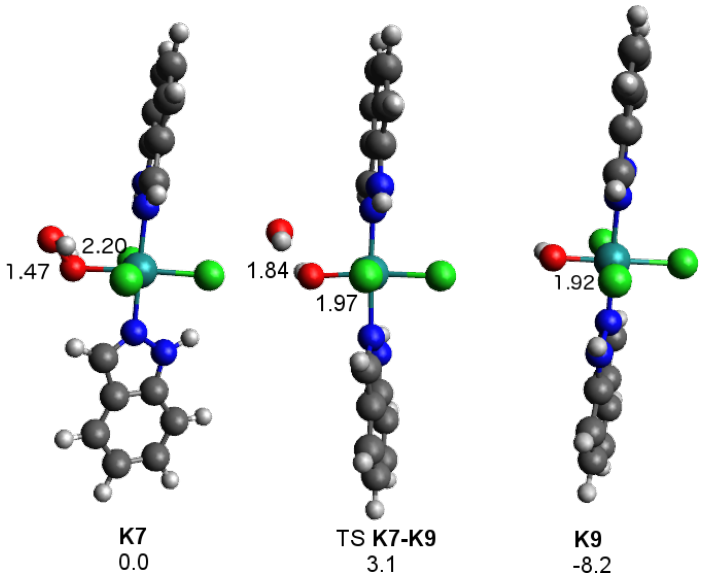

(b) Optimized structures (B3LYP/B1) for KP1019 derivatives. Ru–O and O–O distances are given in Å. Relative free energies in aqueous solution (B3LYP/B2//B1, including all corrections) are given in kcal/mol.

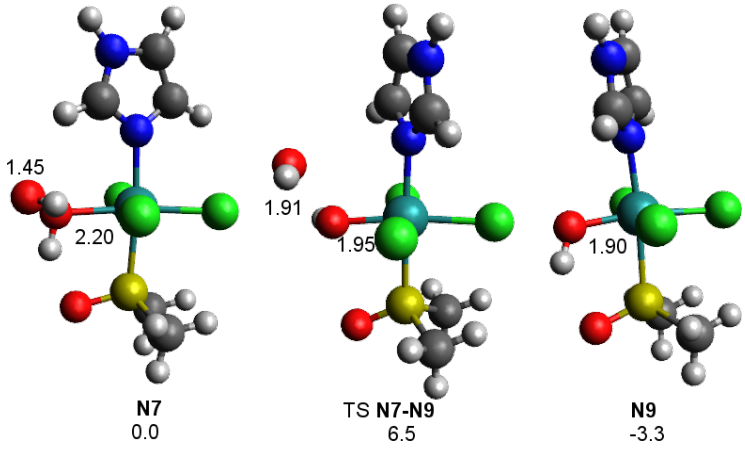

(c) Optimized structures (B3LYP/B1) for NAMI-A derivatives. Ru–O and O–O distances are given in Å. Relative free energies in aqueous solution (B3LYP/B2//B1, including all corrections) are given in kcal/mol.

Figure 4.10: Details on the homolytic O–O bond cleavage mechanism for Ru^{III} compounds.

In conclusion, the oxidations of Ru^{II} and Ru^{III} compounds are assumed to compete with each other in a reductive environment and it depends on the different reaction rates which products are eventually formed. Figure 4.11 presents the results on Fenton-like reactions globally, taking into account all pathways described above. In order to link the results for Ru^{III} compounds to Ru^{II} compounds, the reduction potential of glutathion (GSH) of -263 mV at pH=7.0 in 0.1 M phosphate buffer against the normal hydrogen electrode (NHE) [98] was taken into account.This was then compared with the calculated reduction potential of **K7**/**N7** to **K4**/**N4**, using the ΔG_{sol} values from our calculations, and an externally determined NHE correction of 4.28 V [99][6]. Setting the G_{sol} values of **K4**/**N4** to 0.0 kcal/mol arbitrarily, we arrive at the scheme presented in Figure 4.11 and the data presented in Table 3. The most likely reactive pathway (i.e. the one with the minimum energy) is predicted to proceed from the **K4**/**N4** compounds to **K5**/**N5** which are both "ruthenyl" type compounds.

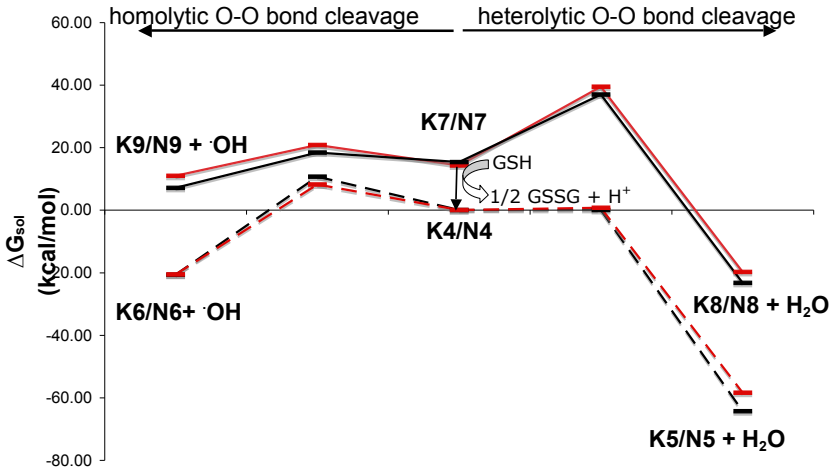

Figure 4.11: Reaction profile for the Fenton-like reactions of **K4** (- - -), **K7** (—), **N4** (- - -) and **N7** (—) . GSH is gluthathion and GSSG is the oxidized glutathion dimer

[6]The calculated reduction potentials against NHE for **K7**/**N7** + e^- → **K4**/**N4** are 0.40/0.36 V. The overall reaction is **K7**/**N7** + GSH → **K4**/**N4** + $\frac{1}{2}$ GSSG + H^+.
GSH is glutathion and GSSG stands for the oxidized glutathion dimer.

Table 3: Computed energies given in kcal/mol (B3LYP/B2//B1) of all compounds shown above and in Figure 4.11 . The highlighted rows show the most likely reactive pathway. Asterisks mark the values for TS **K4-K5** and TS **N4-N5** that have been set to 0.0 kcal/mol, see Footnote 5

		K-compounds			**N-compounds**		
No.	Formula	ΔE	ΔG	ΔG_{sol}	ΔE	ΔG	ΔG_{sol}
4	$[Ru^{II}Cl_3(O_2H_2)L_1L_2]^-$	0.0	0.0	0.0	0.0	0.0	0.0
TS **4-5**		0.0*	0.0*	0.0*	1.1	0.0*	0.7
5 + H_2O	$[Ru^{IV}Cl_3OL_1L_2]^-$	-39.6	-52.4	-64.3	-32.2	-46.0	-58.4
TS **4-6**		11.4	10.0	10.7	10.8	8.0	8.2
6 + OH	$[Ru^{III}Cl_3(OH)L_1L_2]^-$	-1.5	-14.7	-20.6	0.8	-14.6	-20.6
7	$[Ru^{III}Cl_3(O_2H_2)L_1L_2]$	15.4	15.4	15.4	14.3	14.3	14.3
TS **7-8**		39.4	37.0	37.0	44.5	40.5	39.5
8 + H_2O	$[Ru^{V}Cl_3OL_1L_2]$	-4.8	-17.8	-23.3	3.3	-11.2	-19.8
TS **7-9**		21.2	19.1	18.5	27.0	23.2	20.8
9 + OH	$[Ru^{IV}Cl_3(O_2H_2)L_1L_2]$	24.6	10.3	7.2	34.6	18.2	11.0

We compare these results to the calculations of Buda et al [38] who proposed a two-step mechanism of the Fenton-reaction of $[Fe(H_2O)_5(H_2O_2)]^{2+}$ with an initial barrier of 6 kcal/mol. While the computational method and the proposed mechanistic model are different from ours, the essential conclusions read very similar: The proposed product for the Fenton reaction is ferryl $[Fe^{IV}=O]$ (in this work $[Ru^{IV}=O]$ is proposed), and the activation barriers are < 10 kcal/mol. In this work the activation barrier is negligible.

Accordingly, in the following sections the chemistry of $[Ru^{IV}=O]$ compounds will be further explored. Two different types of subsequent reactions involving $[Ru^{IV}=O]$ compounds have been treated. Firstly, the possibility of direct oxygen transfer to dimethyl sulfide (DMS) was investigated. DMS serves as a simple model for thioethers, a functional group found in the amino acid methionine which may be of importance in possible protein targets of Ru anticancer compounds. These results are shown in section 4.3. Secondly, the Hydrogen Atom Transfer (HAT)-type mechanism was investigated for several substrates, including simple alkanes, primary amines and methanethiol. These compounds all serve as simple models for possible biochemical substrates which contain the same functional groups. These results are presented in section 4.4.

4.3 Oxygen Atom Transfer (Singlet PES)

The possibility of oxygen transfer from singlet ruthenyl compounds to dimethyl sulfide (DMS) in a catalytic cycle has been studied according to the scheme shown in Figure 4.12. Starting from *trans*-$[Ru^{II}Cl_4(ind)_2]^{2-}$(**K2**) and *trans*-$[Ru^{II}Cl_4(im)(S{-}dmso)]^{2-}$(**N2**) the first half of the cycle follows the heterolytic type Fenton-like reaction discussed in the previous section. Subsequently, ^{1}**K5**/^{1}**N5** (the singlet states of the ruthenyl compounds) react with DMS *via* an oxygen atom transfer type transition state (TS ^{1}**K5-K10** / TS ^{1}**N5-N10**). This reaction yields dimethyl sulfoxide (DMSO) as a ligand which can coordinate to ruthenium via its oxygen or sulfur donor atoms (**K10**/**N10** for O-DMSO and **K11**/**N11** for S-DMSO). The last step is a hydrolysis back to the aqua compound (**K3**/**N3**). The net reaction of the cycle is therefore DMS + H_2O_2 → DMSO + H_2O.

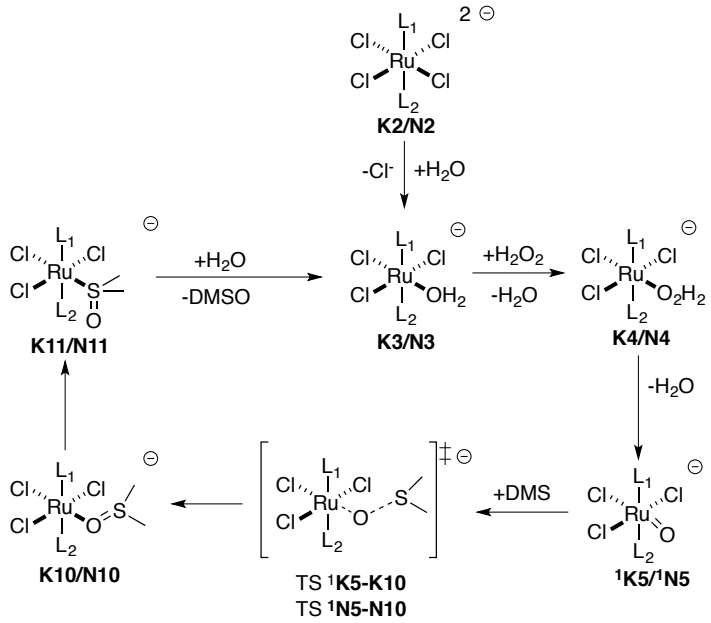

Figure 4.12: Catalytic cycle scheme for the oxygen transfer reaction

The ^{1}**K5**/^{1}**N5** compounds are structurally similar to their analogous ^{3}**K5** / ^{3}**N5** compounds. The Ru–O distances of 1.77 Å (^{1}**K5**) and 1.78 (^{1}**N5**) Å virtually do not differ from the triplet state geometries (1.78 Å in ^{3}**K5**/1.78 Å in ^{3}**N5**).

The first step to investigate is the oxygen atom transfer step itself which takes place via the transition states TS ^{1}**K5-K10** and TS ^{1}**N5-N10**. The linkage isomers **K10**/**N10** and **K11**/**N11** contain dimethyl sulfoxide (DMSO) as a ligand after the oxygen transfer step. Optimized geometries of TS **K5-K10** / TS **N5-N10**, **K10**/**N10** and **K11**/**N11** are shown in Figures 4.13a and 4.13b.

These structures show that the Ru–O distance increases along the oxygen atom transfer reaction coordinate from 1.77/1.78 Å in **K5/N5** to 1.89/1.87 Å in the transition state structures TS **K5-K10** / TS **N5-N10**. Finally, in the **K10/N10** compounds, the Ru–O distance is 2.21/2.19 Å, similar to the Ru^{II} compounds discussed before. For the **K11/N11** linkage isomers, the Ru–S distance is 2.27 Å (**K11**) and 2.30 Å (**N11**). Interestingly, there is no difference in the Ru–S distances in compound **N11** for both S-DMSO ligands. Yet, both Ru–S distances are widened from 2.19/2.24 Å to 2.30 Å each.

The **K11/N11** compounds are thermodynamically stabilized in comparison with the **K10/N10** compounds. The stabilization effect is sizeable (-9.3 kcal/mol for **K10→K11** and -8.9 kcal/mol for **N10→N11**), revealing that S is the thermodynamically preferred donor atom, which may be ascribed to back-donation effects. This finding also corresponds to the empirical Hard and Soft Acids and Bases (HSAB) concept [100], with Ru^{II} as a "soft" acid and the S atom as a "soft" base.

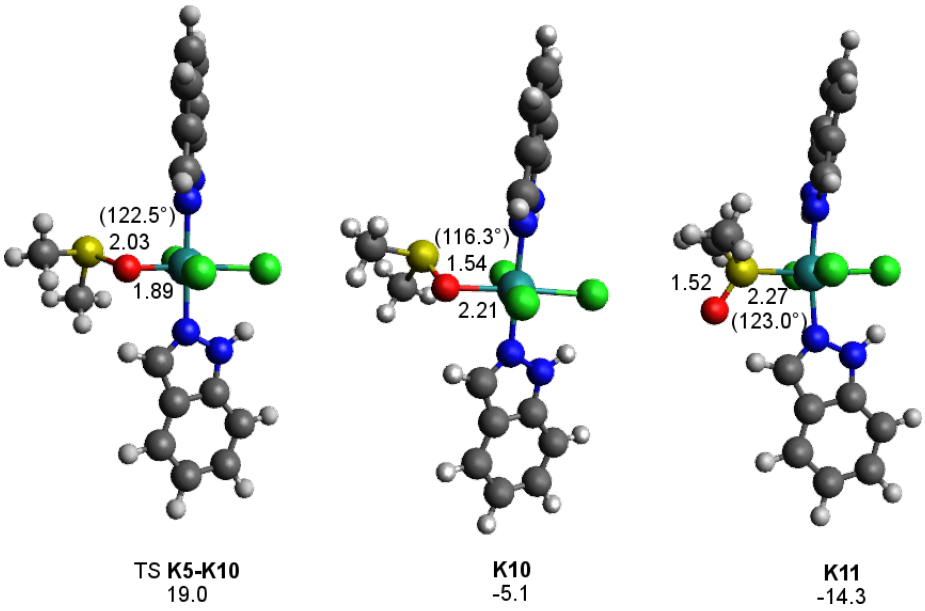

(a) Optimized structures for KP1019 derivatives.The Ru–O, Ru–S and O–S distances are given in Å. The Ru–O–S angle is given in degrees. Free energies in solution (B3LYP/B2//B1, including all corrections) are given in kcal/mol with respect to ^{1}**K5**+**DMS**.

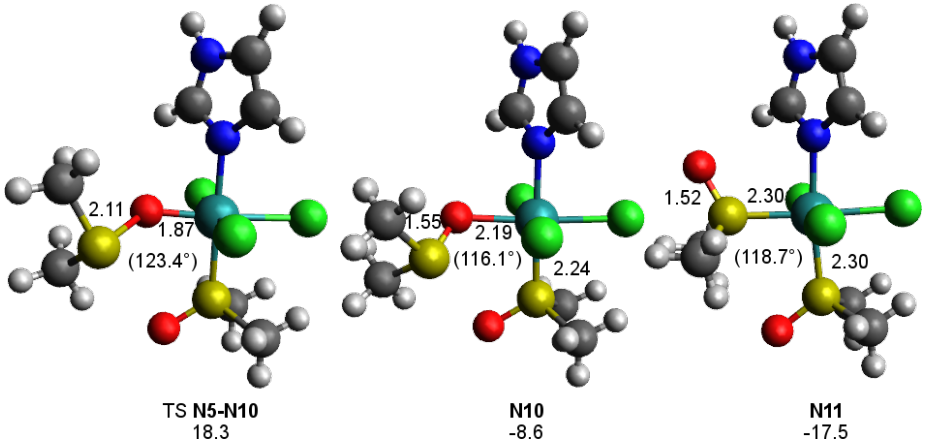

(b) Optimized structures for NAMI-A derivatives. The Ru–O, Ru–S and O–S distances are given in Å. The Ru–O–S angle is given in degrees. Free energies in solution (B3LYP/B2//B1, including all corrections) are given in kcal/mol with respect to ^{1}**N5**+**DMS**.

Figure 4.13: Optimized geometries and energies of the oxygen atom transfer to DMS.

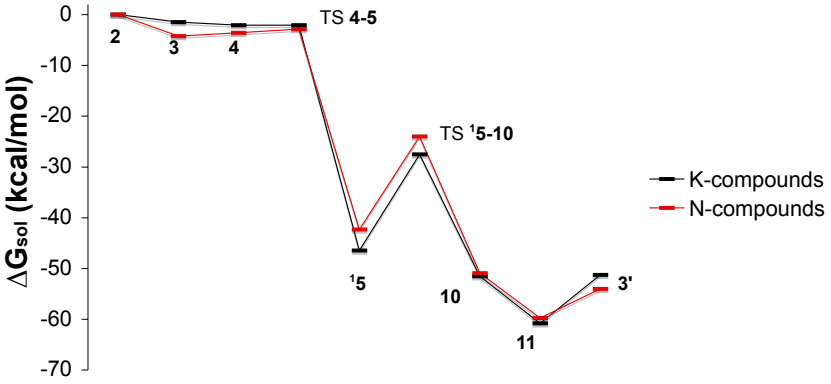

Figure 4.14: Calculated free energy profile (B3LYP/B2//B1, including all corrections) for the species of the cycle depicted in Figure 4.12. The net reaction $H_2O_2 + DMS \rightarrow H_2O + DMSO$ from **3** to **3'** ($\Delta_R G_{sol}$ =-49.8 kcal/mol) is implied.

The calculated free energy profile in Figure 4.14 reveals that the net reaction free energy in solution (B3LYP/B2//B1, including all corrections, from **3** to **3'**) is -49.8 kcal/mol. The oxygen transfer step itself has a barrier of 19.0 kcal/mol (TS **K5-K10**) and 18.3 kcal/mol (TS **N5-N10**). These values are higher than the activation barrier ($\Delta G^{\ddagger}_{sol}$) of oxidation of DMS by H_2O_2 of 12.7 kcal/mol at the MP4//B3LYP/6-31++G(d,p) level of theory [101]. However, since the authors in reference [101] used a different model with explicit water molecules and the obtained values of reference [101] and of this work differ strongly, it is difficult to compare them. Instead, the activation barriers for O atom transfer from Ru compounds **K5**/**N5** to DMS calculated in this work are comparable to an experimental value of 21.0 kcal/mol for the oxidation of thioxane by H_2O_2 in aqueous solution at 298 K [102]. As thioxane is quite similar to DMS with regard to the chemical surroundings of the sulfur atom, the experimental study [102] is considered appropriate and comparable in this case.

The electronic ground state of **K5**/**N5** structures does not have a singlet but a triplet character. Therefore, the effective activation barrier for the oxygen atom transfer (from compound **K5**/**N5** to TS **K5-K10**/TS **N5-N10**) is predicted to be augmented by the energy of the singlet-triplet gap (B3LYP/B2//B1, including all corrections) of 21.1 (^{3}**K5**-^{1}**K5**) and 19.6 (^{3}**N5**-^{1}**N5**) kcal/mol. This makes the **K5**/**N5** compounds "thermodynamic traps" (compounds that are too stable for the reaction to proceed along the reaction coordinate for oxygen atom transfer because the TS **K5-K10** / TS **N5-N10** are both too high in energy).

Summarizing the findings in this section, the likelihood of $^{1}[Ru^{IV}{=}O]$ compounds reacting *via* the oxygen transfer mechanism route have been predicted to be low. As the effective activation barriers are considerably lower for free H_2O_2 in aqueous solution, the O-transfer catalytic cycle presents a redundant path of H_2O_2 activation and one must therefore look to different types of mechanisms such as HAT which will be discussed in the following section.

4.4 Hydrogen Atom Transfer (HAT) to Ruthenyl Compounds

The reactive pathways of H-abstraction involve two reactant species: the $[Ru^{IV}=O]$ species and a substrate molecule which is called Y–H. The proposed catalytic cycle involving a HAT-type mechanism is depicted in Figure 4.15. The pool of substrates treated in this work is given in Figure 4.16 and comprises (i) simple alkanes, (ii) primary amines and (iii) methyl thiol. These molecules serve as computational models for (i) aliphatic side chain moieties of amino acids and triglycerides (ii), the side chain of lysine, and (iii) the side chain of cysteine. The chemistry is taking place at the functional group and the surroundings may have a chemical effect but for e.g. primary amines (as shown below), this effect is marginal.

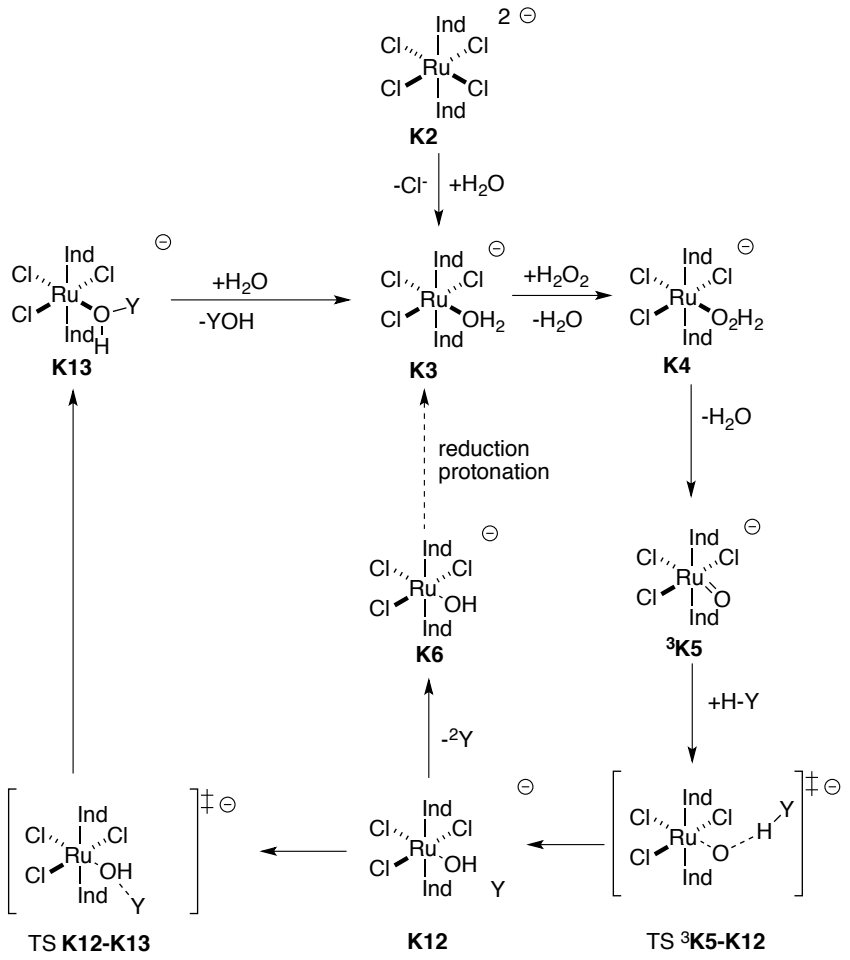

Figure 4.15: Proposed catalytic cycle for the HAT mechanism. The various substrates (H-atom donors) are labeled Y-H and comprise alkanes, amines and methyl thiol (see Figure 4.16).

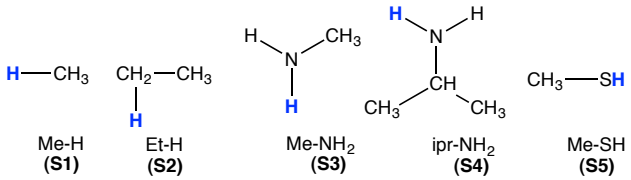

Figure 4.16: Substrates (Y–H). The **H**-atom to be abstracted is marked.

For this reaction, we focus on the KP1019 derivative compounds although we expect similar results for NAMI-A derivatives. For the catalatytic cycle in Figure 4.15, we start again with **K2** *via* the aquated compound (**K3**) and the Fenton-like reaction to the **K5** compound which is a ruthenyl species and has a triplet ground state (as discussed ion section 4.2). **K5** may abstract a hydrogen atom from a substrate Y–H (TS ^{3}**K5-K12**). The compound **K12** is an intermediate species where the substrate radical ^{2}Y can be either set free (yielding **K6** and the free radical) or further react *via* TS **K12-K13** to give the hydroxylated substrate as a ligand (**K13**) which can then be replaced by an aqua ligand, thereby returning to **K3**.

In the following, first the optimized geometries along the HAT reaction coordinate for the various substrates are going to be presented and discussed. Subsequently, the energetics of the HAT mechanism with Ru compounds will be discussed and finally, the energy profile of the whole catalytic cycle will be shown.

The results presented in this section have been produced using the B3LYP-D as well as non-dispersion corrected methods. The reason for this is the presence of (short) alkyl side chains. Geometries involving these traits (such as those involving isopropylamine as a substrate) are only efficiently optimized by including dispersion interactions, as they help orientate the alkyl chains. Dispersion-corrected energy values as well as non-dispersion corrected energies are reported (for geometries optimized with non-dispersion corrected B3LYP, where possible).

4.4.1 Structures of the HAT Mechanism

4.4.1.1 HAT with Simple Alkanes

Methane and ethane were chosen as substrates. The optimized geometries involved in the HAT-type mechanism for methane (**S1**) and ethane (**S2**) are found in figures 4.17a and 4.17b, respectively. The optimized geometries in these figures illustrate that along the path from TS **K5-K12** to **K13** the Ru–O distance steadily increases. In the intermediate species (**K12**) the methyl/ethyl radical is weakly bound by dispersion interactions to the indazole rings of the the monohydroxo complex with a typical O–H bond length in the **K12** compounds of 0.97 Å. The **K13** compounds show methanol/ethanol as ligands to the Ru complex.

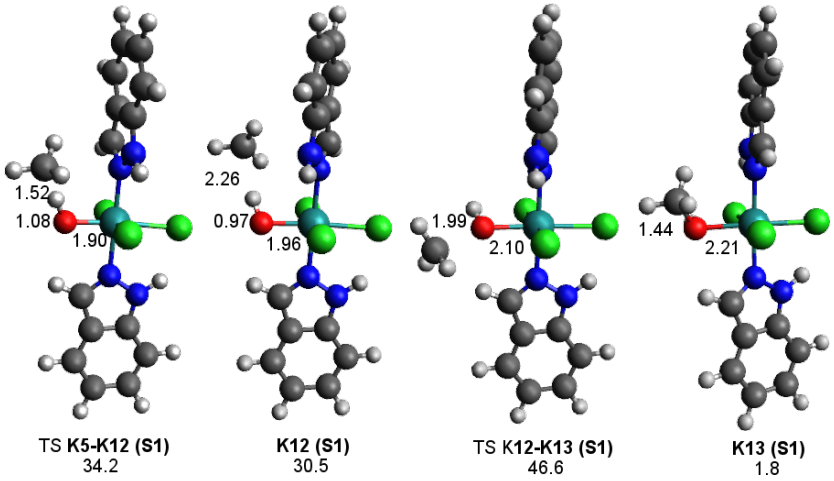

(a) Optimized geometries (B3LYP-D/B1) of the HAT mechanism with CH_4 (**S1**). The Ru–O, O–H, C–H and C–O distances are given in Å. Relative free energies in solution (B3LYP-D/B2//B1, including all corrections) are given in kcal/mol. The reference is ^{3}**K5**+**S1**.

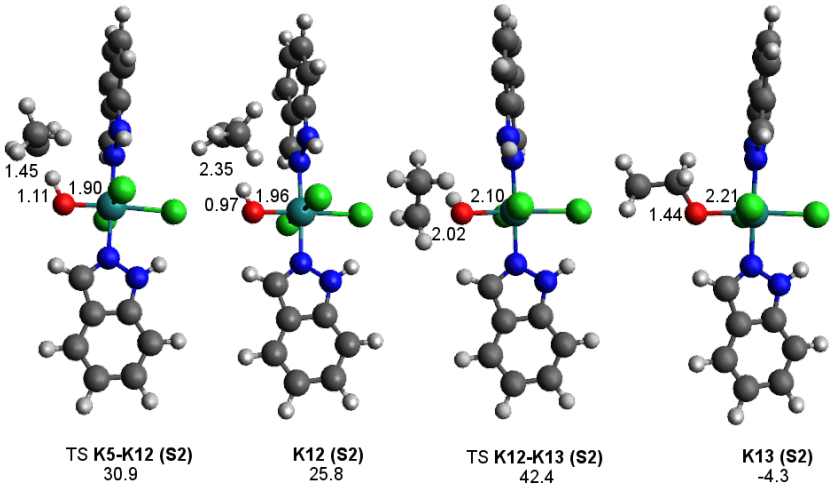

(b) Optimized geometries (B3LYP-D/B1) of the HAT mechanism with CH_3CH_3 (**S2**).The Ru–O, O–H, C–H and C–O distances are given in Å. Relative free energies in solution (B3LYP-D/B2//B1, including all corrections) are given in kcal/mol. The reference is ^{3}**K5**+**S2**.

Figure 4.17: Optimized geometries of the HAT mechanism with simple alkanes.

4.4.1.2 HAT with Primary Amines

Similarly to the choice of CH_4 as the first substrate in modeling alkyl H-abstraction reaction mechanisms, methylamine (**S3**) was selected as the first amine to treat. The second substrate was isopropyl amine (**S4**).

The optimized structures (B3LYP-D/B1) for the HAT-type mechanism with **S3** and **S4** are found in figures 4.18a and 4.18b.

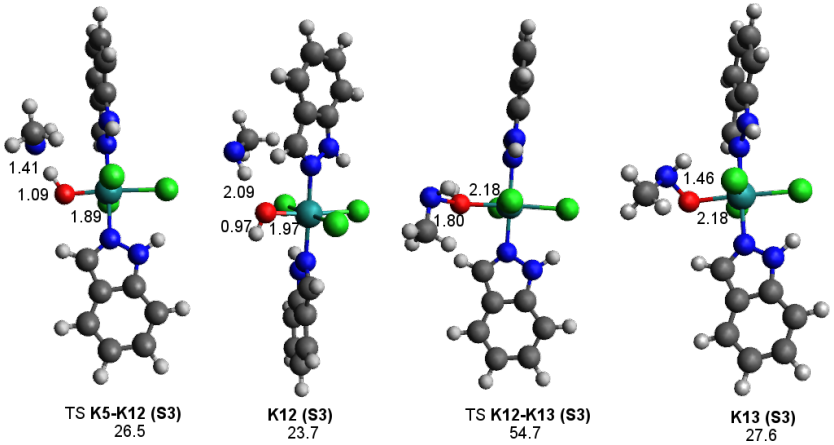

(a) Optimized geometries (B3LYP-D/B1) of the HAT mechanism with $NHCH_3$ (**S3**). Ru–O, O–H, H–N and O–N distances are given in Å. Relative free energies in solution (B3LYP-D/B2//B1, including all corrections) are given in kcal/mol. The reference is ^{3}**K5**+**S3**

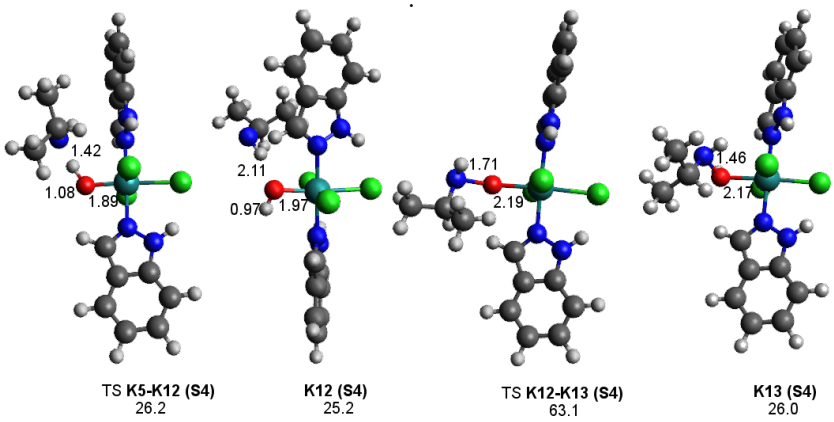

(b) Optimized geometries (B3LYP-D/B1) of the HAT mechanism with $(CH_3)_2CHNH_2$ (**S4**). Ru–O, O–H, H–N and O–N distances are given in Å. Relative free energies in solution (B3LYP-D/B2//B1, including all corrections) are given in kcal/mol. The reference is ^{3}**K5**+**S4**

Figure 4.18: Optimized geometries of the HAT mechanism with primary amines.

For substrates **S3** and **S4**, the Ru–O distance increases along the reaction path from **K5** to **K13**. The intermediate species **K12** also has the amine radical weakly bonded by dispersion interactions to the indazole rings. Remarkably, there is hardly any structural difference between the compounds for **S3** and **S4**. This is also reflected in the energies discussed in section 4.4.2.

4.4.1.3 HAT with Methyl Thiol

Methyl thiol (CH_3SH, **S5**) was chosen as a substrate because of its simplicity and adequacy as a model compound for thiols. The optimized structures can be found in Figure 4.19.

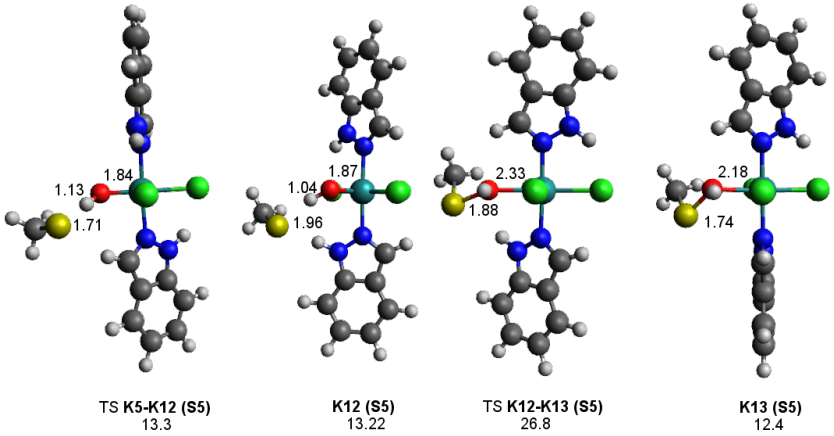

Figure 4.19: Optimized geometries (B3LYP-D/B1) of the HAT mechanism with $SHCH_3$ (**S5**). The Ru–O, O–H, H–S and S–O are given in Å. Relative free energies in solution (B3LYP-D/B2//B1, including all corrections) are given in kcal/mol. The reference is ^{3}**K5**+**S5**

In this case, the intermediate **K12** exhibits a hydrogen bonded sulfur radical with the O–H distance significantly elongated to 1.04 Å. The TS **K12-K13** geometry also features an elongated Ru–O distance of 2.33 Å. Overall, the Ru–O distance increases from 1.78 Å (**K5**, see previous sections) to 2.18 Å (**K13**) and the sulfenic acid tautomer is bound coordinatively to the Ru complex in **K13**.

4.4.1.4 Discussion of the Optimized Geometries

Comparison of the geometries for the TS **K5-K12** structures, depending on the substrates (see Figure 4.21) suggests a π-type path for the hydrogen abstraction reaction, as recently described by Usharani et al. [103] in the context of hydrogen-abstraction reactions of high oxidized iron compounds. To understand the electronic structure and the reactivity of a ruthenyl compound, it is useful to look at a molecular orbital (MO) diagram. The qualitative MO diagram for a d^4 Ru=O bond is found in Figure 4.20. The π-type path for the HAT mechanism may be described qualitatively by the overlap of the π^* orbital at the [Ru^{IV}=O] compound and the σ orbital of the C–H, N–H or S–H bond respectively. The angle Ru–O–H is obtuse. The Ru–O and H–C (H–N, H–S) distances depend of course on the nature of the substrate. The calculated structural data and a scheme of the π-type transition state are given in Figure 4.21.

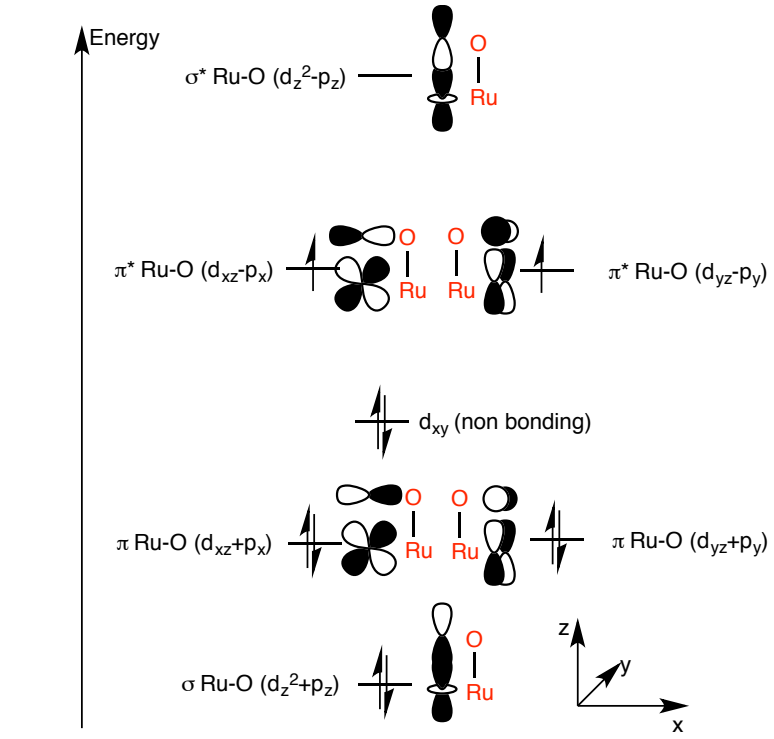

Figure 4.20: Qualitative MO diagram of a [Ru^{IV}=O] compound with electron occupation indicated.

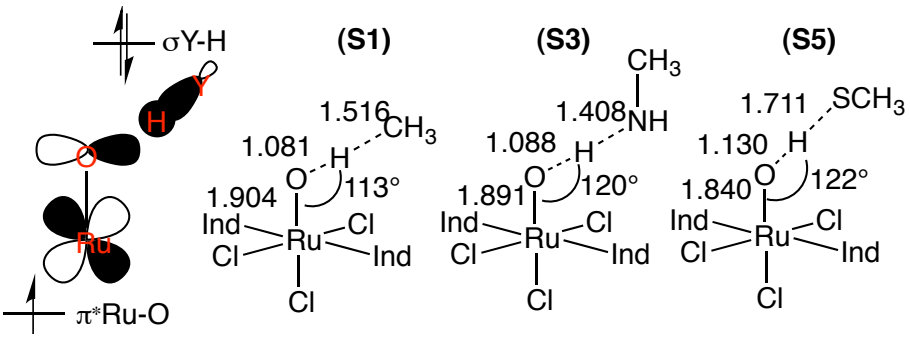

Figure 4.21: Examplified qualitative H-abstraction schematic for TS **K5-K12** and **S1**/**S3**/**S5**. Calculated bond lengths (B3LYP-D/B1) in Å and angles in degrees. One negative charge has been omitted for clarity.

The intermediate (**K12**) involves the newly formed substrate radical (^{2}Y). This radical positions itself somewhere favorably close to the Ru complex. From **K12**, the reaction may proceed along two paths: One is the dissociation of the radical formed, yielding the free substrate radical ^{2}Y and the mono-hydroxo Ru^{III} compound **K6**. This compound may be reduced by an outer sphere mechanism to the monoaquated species **K3**, thereby completing a catalytic cycle.

This process depends on the stability of the substrate radical ^{2}Y.

TS **K12-K13** may be described as the "oxygen rebound" [104] transition state where the oxygen is transferred in our case to the C, N or S atom. This process yields the hydroxylated substrate Y–OH. The calculated structural data for TS **K12-K13** with substrates **S1**, **S3** and **S5** are presented in Figure 4.22. The structural features of the TS **K12-K13** geometries indicate that there is a hydroxo complex species with a Ru–O distance of 2.1 to 2.3 Å and the imaginary modes resulting from the frequency calculations point along the oxygen transfer coordinate from the ruthenium center to the intermediate species reacting. The angle Ru–O–C (Ru–O–N, Ru–O–S) varies from 138° to 154°.

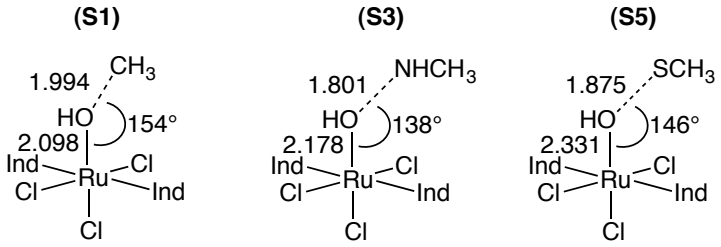

Figure 4.22: Key geometrical features at the B3LYP-D/B1 level of theory for TS **K12-K13** ("oxygen rebound"), with substrates **S1**, **S3** and **S5**. Bond lengths are given in Å and angles in degrees. One negative charge has been omitted for clarity.

4.4.2 The Energetics of the HAT Mechanism

This part of the thesis sums up the results on the HAT-type mechanism for ruthenyl compounds. The reaction profiles are presented and discussed, followed by a comparison to computational studies on the chemistry of ferryl compounds. At the end, the energy profile of the entire catalytic cycle in Figure 4.15 will be shown and discussed.

Table 4: Non-dispersion corrected ΔG_{sol} values (B3LYP/B2//B1, including all corrections, kcal/mol) for the HAT-type mechanism ordered by compounds and substrates. For isopropylamine **(S4)** there exist no non dispersion-corrected data. The last line shows the energy calculated for the net reaction of the catalytic cycle.

	Me–H (**S1**)	Et–H (**S2**)	$MeNH_2$ (**S3**)	$iprNH_2$ (**S4**)	Me-SH (**S5**)
^{3}**K5** + Y–H	0.00	0.00	0.00	–	0.00
TS **K5-K12**	38.56	37.02	35.24	–	18.00
K12	33.92	29.76	28.73	–	17.34
K6+Y	27.43	21.18	20.51	–	9.56
TS **K12-K13**	51.82	46.99	66.74	–	34.33
K13	9.39	3.00	35.16	–	18.03
$Y{-}H + H_2O_2 \rightarrow Y{-}OH + H_2O$	-58.12	-63.96	-32.47	–	-51.65

Table 5: Dispersion corrected ΔG_{sol} (B3LYP-D/B2//B1, including all corrections, kcal/mol) for the HAT-type mechanism ordered by compounds and substrates. The last line shows the energy calculated for the net reaction of the catalytic cycle.

	Me–H (**S1**)	Et–H (**S2**)	$MeNH_2$ (**S3**)	$iprNH_2$ (**S4**)	Me-SH (**S5**)
^{3}**K5** + Y–H	0.00	0.00	0.00	0.00	0.00
TS **K5-K12**	34.17	30.90	26.46	26.17	13.28
K12	30.48	25.82	23.71	25.19	13.22
K6+Y	26.01	20.35	19.37	20.07	8.46
TS **K12-K13**	46.59	42.42	54.68	63.11	26.78
K13	1.78	-4.25	27.56	26.03	12.39
$Y{-}H + H_2O_2 \rightarrow Y{-}OH + H_2O$	-57.41	-60.97	-31.00	-24.89	-50.04

The energies were all calculated in the electronic ground state of the respective compounds. For compounds **K2-K4** and **K13**, this is the singlet low spin state, for compounds **K5** (the ruthenyl compound), TS **K5-K12**, **K12**, TS **K12-K13**, this is the triplet intermediate spin state and for **K6**, this is the doublet low spin state. The B3LYP(-D) ground state predictions are low spin for all Ru^{II} and Ru^{III} compounds and the triplet state was reported to be the ground state for a Ru^{IV}=O compound previously [96].

All calculated free energies in solution of the HAT-type mechanism (dispersion-corrected and non dispersion-corrected) can be found in Tables 4 and 5. The data in these tables start at the **K5** compounds (setting the energies of **K5** + Y–H to 0.0 kcal/mol) and go until the **K13** structures, after which the cycle is completed by hydrolysis. The resulting energy profiles are visualized in Figure 4.23.

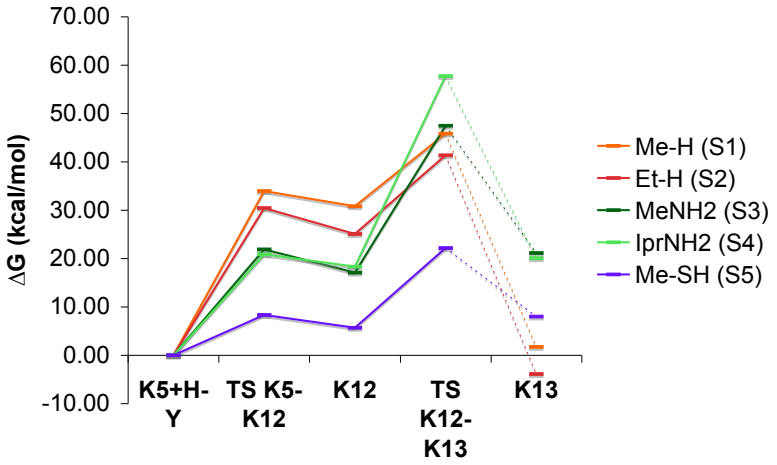

Figure 4.23: Calculated reaction profiles (detail of the catalytic cycle in Figure 4.24) in solution (B3LYP-D/B2//B1, including all corrections) for the HAT mechanism with all substrates. The **K13** compounds are connected by dotted lines because of different multiplicity.

By comparison of the B3LYP results to the B3LYP-D results, it can be seen that the effect of the dispersion correction is lowering the energy of the TS **K5-K12**, **K12**, TS **K12-K13** and **K13** compounds of 4.0 to 12.0 kcal/mol. The **K6**+**Y** and net reaction free energies are affected to a lesser extent (1.0 to 3.0 kcal/mol). This effect may be explained by the lack of intermolecular dispersion in the latter cases as the energies were taken at infinite separation of the respective product species.

The discussion of the energetics is structured by the substrate classes (alkanes, primary amines and methyl thiol).

The alkanes (**S1, S2**) show a very high first barrier (TS **K5-K12**).The **K12** species may also set free the alkyl radical, an overall endergonic process, yet the energy of **K6**+Y is lower than the second activation barrier of TS (**K12-K13**). The energies for **K6**+Y reflect the relative stability of the ethyl radical vs. the methyl radical. The overall reaction free energy from **K5** to **K13** is only slightly positive (**S1**) or even negative (**S2**). This finding leads to the conclusion that [Ru^{IV}=O] compounds may indeed be able to hydroxylate alkanes with longer aliphatic chains and in activated positions, e.g. allylic, benzylic. The more stable the alkyl radical becomes the lower is the barrier for TS **K5-K12**. Further implications of this finding are discussed in the outlook.

For primary amines (**S3, S4**), the results are different. Although the first

barrier (TS **K5-K12**) is somewhat lower than in the cases of **S1, S2**, the highest relative energy along the way (TS **K12-K13**) is higher than for the alkanes and importantly, the overall reaction free energy from **K5** to **K13** is clearly positive (>25 kcal/mol in solution). For **S3, S4** it is also energetically more favorable to release the amine radical and form **K6**+Y than to form the TS **K12-K13**.

Finally, H-abstraction from methyl thiol (**S5**) has the lowest lying first transition state (TS **K5-K12** at +13.3 kcal/mol in solution). However, the overall reaction free energy from **K5** to **K13** is still positive (+12.4 kcal/mol reaction free energy in solution), rendering the hydroxylation of thiols by [Ru^{IV}=O] compounds unlikely. For methyl thiol, the release of the sulfur radical from the **K12** is by far the most energetically favorable, at +8.5 kcal/mol in solution.

Comparing the computational results of the HAT mechanism with Ru compounds, one can postulate a correlation between reaction free energies and activation barriers. The results presented above lead to the conclusions that (i) the more favorable the overall catalysed reaction ($Y{-}H + H_2O_2 \rightarrow Y{-}OH + H_2O$) is, the more favorable are the energies of the HAT mechanism from species **K5** to **K13** (ii) the more stable a substrate radical ^2Y is, the lower is the initial activation energy (TS **K5-K12**).

The energy profile in solution for the entire catalytic cycle proposed in Figure 4.15 is found in Figure 4.24. Therein, it becomes clear that the liberation of the substrate radical ^2Y is energetically favorable to the intermediate species **K12** with the given radical. The liberation of ^2Y is indicated by the dashed lines. The "oxygen rebound" cycle continues *via* the **K12** species. Additionally, the correlation between high barrier heights and less favorable thermodynamics becomes clear, concerning the amines and simple alkane substrates. Methyl thiol plays a somewhat different role with the lowest energy barriers. This may be attributed to the postulated correlation between thermodynamics and activation energies, see calculated free energies in solution on methyl thiol oxidation by H_2O_2 in the Tables 4 and 5.

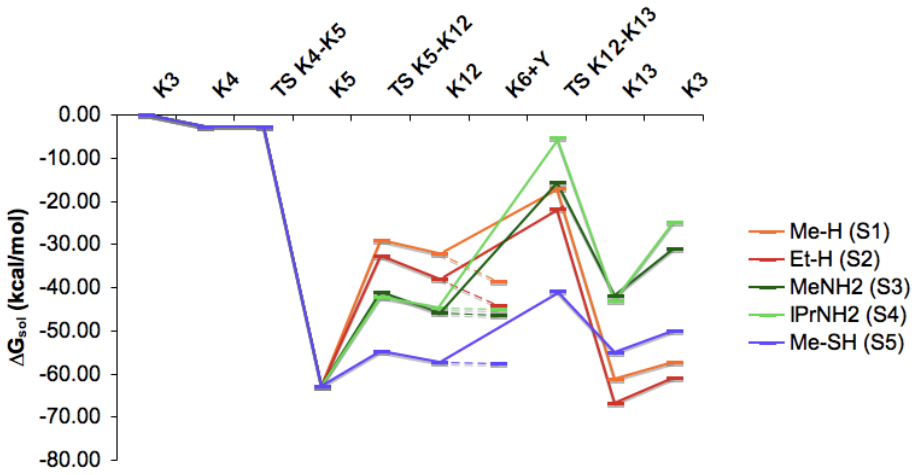

Figure 4.24: Energy profile of the HAT catalytic cycle in solution (B3LYP-D/B2//B1, including all corrections) for the HAT mechanism with all substrates.

The treatment of HAT-mechanisms with [Ru^{IV}=O] invites the comparison with the chemistry of high-oxidized iron-oxo species that occur in the active centers of various oxidase enzymes such as members of the cytochrome P 450 class of enzymes.[105]

The CH_4 molecule has previously served in the evaluation of ferryl chemistry, following the Fenton reaction [106]. Ensing et al. have found a "rebound" type mechanism by which the ferryl species can oxidize methane to methanol with relatively low activation barriers considerably lower than 10 kcal/mol [106].

We compare our findings on the amine-substrates to the DFT results of Olsen and co-workers [107, 108] and a very recent study by Ji and Schüürmann [109] who have both concluded that the hydroxylation of primary amines by [Fe^{IV}=O] compounds in cytochrome P450 enzymes is likely to proceed *via* the HAT-mechanism. Contrary to [Fe^{IV}=O] compounds, the [Ru^{IV}=O] compounds treated in this study are not predicted to be able to hydroxylate primary amines because of (i) high activation barriers (ii) an overall positive reaction free energy.

Summing up the comparisons, we have found that the reactivity of ferryl compounds (references cited above) is substantially higher than that of ruthenyl compounds concerning HAT (and subsequent hydroxylation) reactions with simple organic substrates. The [Ru^{IV}=O] compounds examined in this work exhibit high activation barriers for the same type of reactions and even positive computed reaction free energies for amines and thiols.

5 Conclusion and Outlook

The high presence of hydrogen peroxide in certain human cancer cell lines [29, 46, 49] has prompted us to investigate the redox behavior of selected derivatives of anticancer complexes KP1019 and NAMI-A in the presence of H_2O_2 using DFT methods.

The two assumptions that (i) KP1019 and NAMI-A are reduced in vitro and in vivo and that (ii) at least one ligand is exchanged are supported by experimental evidence [18, 19, 95]. In this work, the optimized structures of hydroperoxide derivatives of NAMI-A and KP1019 show that H_2O_2 can coordinate Ru complexes just like H_2O does.

A visualization of the reactive pathways treated in this thesis, highlighting its main focus areas, is given in Figure 5.1, examplified for the KP1019 derivative structures (the **K** compounds). As shown in Figure 5.1, our first finding has been that both Ru^{II} and Ru^{III} compounds can be oxidized by hydrogen peroxide after H_2O_2 coordination. Both Ru^{II} KP1019 and NAMI-A derivatives are predicted to react with H_2O_2 in a heterolytic, concerted, two electron process with virtually no activation barrier to give ruthenyl compounds. These $[Ru^{IV}{=}O]$ (ruthenyl) compounds are predicted to have a triplet ground state. The heterolytic process is favored energetically over the homolytic peroxide bond cleavage mechanism by a lower activation energy and more favorable thermodynamics. On the other hand, for *mer,trans*-$[Ru^{III}Cl_3(ind)_2(O_2H_2)]$ and *mer*-$[Ru^{III}Cl_3(im)(O_2H_2)(S{-}dmso)]$ the homolytic peroxide bond cleavage process is preferred, yielding a hydroxo-Ru^{IV} species and a highly reactive hydroxyl radical. For Ru^{III} compounds, the homolytic peroxide bond cleavage process is favored over the heterolytic one.

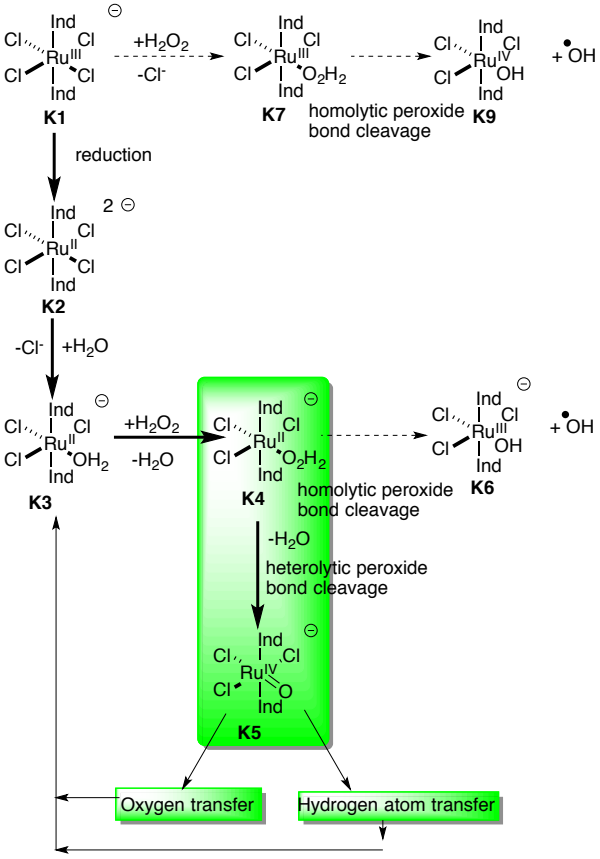

Figure 5.1: Reactive pathways of KP1019 derivatives treated in this thesis. The thick arrows show reactive pathways with a high probability based on very recent experimental work [95] and this work. The green parts represent the main focus areas of this thesis, namely the heterolytic H_2O_2 bond cleavage at Ru^{II} and the possible follow-up reactions. The dotted arrows show alternative reactive pathways also treated herein. All pathways above except the Hydrogen Atom Transfer have also been investigated for NAMI-A derivatives and are reported herein.

This study then focusses on two possible reactive pathways of $[Ru^{IV}{=}O]$ compounds, namely oxygen atom transfer and hydrogen atom transfer (HAT).

For oxygen atom transfer the substrate dimethyl sulfide (DMS) was chosen as a model for sulfur compounds such as the side chain of methionine. Our findings on oxygen atom transfer are as follows: There is a reaction pathway for *mer,trans*-$[Ru^{IV}Cl_3(ind)_2O]^-$ and *mer*-$[Ru^{IV}Cl_3(im)O(S{-}dmso)]^-$ in their singlet states to oxidize DMS so as to yield DMSO. However, the singlet states of *mer,trans*-$[Ru^{IV}Cl_3(ind)_2O]^-$ and *mer*-$[Ru^{IV}Cl_3(im)O(S{-}dmso)]^-$ are not the electronic ground states but the first excited states. Taking the additional barrier of the triplet-singlet gap into account, the activation energies for oxygen

transfer are higher than the ones both calculated[101] and measured [102] for oxygen transfer from free hydrogen peroxide. Therefore, the oxygen transfer pathway for [Ru^{IV}=O] compounds is predicted to be an unlikely one.

We have investigazed the HAT-type mechanism. We have found on a [Ru^{IV}=O] compound with a variety of substrates that the activation energies are high. Hydrogen atom transfer to ruthenyl compounds may therefore only occur for certain substrates in activated positions. The reaction is predicted to be thermodynamically favorable for most alkanes, but not for primary amines or thiols. Juxtaposing the calculations on HAT-type mechanisms for [Ru^{IV}=O] compounds and [Fe^{IV}=O] compounds[107, 109] reveals that [Ru^{IV}=O] compounds are predicted to be less reactive towards the substrates tested.

The outlook regarding the HAT-type mechanism is to provide results for the NAMI-A derivatives and expand the library of substrates. Cumene is a good testing agent for the oxidative power of Ru^{IV} complexes (see reference [96]). Future calculations could predict whether a Ru^{IV} compound is able to hydroxylate these compounds, which would put an entirely different, novel use to the ruthenium compounds KP1019 and NAMI-A or certain analogues thereof.

Also, the possible formation of certain stabilized radicals (such as the methyl thiol radical) that could be released after the first step of the HAT-type mechanism is still to be scrutinized.

Experimental cooperation has been initiated on Fenton-like reaction of ruthenium anticancer compounds within the working group of Prof. V. Arion at the institute of Inorganic Chemistry at the University of Vienna. With the appropriate experimental methods the predicted rise of a ruthenyl intermediate species when Ru anticancer compounds are exposed to significant levels of H_2O_2 may be detected. In addition, the possibility of an oxidative catalytic activity of Ru anticancer compounds in the presence of H_2O_2 may be assessed using various substrates, such as cyclohexane or cumene.

If theoretical and experimental results correspond well, the implication of an oxidative ruthenyl species is suggested thereby in the mode of action of Ru anticancer compounds KP1019 and NAMI-A. The Ru^{IV} compound could be involved in a catalytic cycle where one molecule may be involved in oxidative damage to a large number of biological targets such as DNA or proteins, which may ultimately lead to tumor cell apoptosis. Involvement of Ru^{IV} compounds remains to be investigated in the future.

6 Acknowledgment

An erster Stelle danke ich meinen Eltern Alexander und Cezarina für ihre Unterstützung meines Studienweges an der Fakultät für Chemie. Sämtliche akademische Aspirationen meinerseits sind allein auf Grund ihrer jahrelangen konsequenten Förderung möglich gewesen.
Ebenfalls danke ich Ass. Prof. Dr. Dirk Deubel für den Themenvorschlag, die direkte Supervision und die Computer-Ressourcen sowie Univ. Prof. Dr. Leticia González für die Bereitschaft, diese Arbeit in offizieller Art und Weise zu betreuen.
Mein ausgesprochener Dank gilt weiterhin den Mitgliedern der Arbeitsgruppe "Theochem" an der Universität Wien für das tägliche Spektakel, mit ihnen arbeiten zu dürfen.
Weiterhin danke ich Univ. Prof. Dr. Othmar Steinhauser und Univ. Prof. Dr. Annette Rompel für ihre wertvollen Ratschläge entlang meines Studienweges.

First and foremost I would like to thank my parents Alexander and Cezarina for supporting me on my way through my studies of chemistry. All my academic endeavors have been made possible by their continuing encouragement and financial endowment.
I would also like to thank Ass. Prof. Dr. Dirk Deubel for suggesting the topic, the direct supervision and the computation ressources and Prof. Dr. Leticia González for being the official adviser to this thesis.
Moreover, I would like to thank the members of the "theochem" working group at the University of Vienna. It has been a spectacle for me to work with you.
Finally, thanks to Prof. Othmar Steinhauser and Prof. Annette Rompel at the University of Vienna for the valuable advice along my way.

7 Glossary

In order to increase readability, a glossary of abbreviations and symbols is given herein.

Acronyms:
ASC... Apparent Surface Charge
B3LYP...Becke 3 Parameter Lee-Yang-Parr hybrid functional
BS...Broken Symmetry
CASSCF...Complete Active Space Self Consistent Field
CASSCF-SOCI...Complete Active Space Self Consistent Field - Spin Orbit Configuration Interaction
DFT...Density Functional Theory
HAT...Hydrogen Atom Transfer
HSAB...Hard and Soft Acids and Bases
HF...Hartree-Fock
KS...Kohn-Sham
MCSCF...Multiconfigurational Self Consistent Field
MRCI...Multireference Configuration Interaction
PBF...Poisson-Boltzmann Finite Elements
PES...Potential Energy Surface
ROS...Reactive Oxygen Species
SCF...Self Consistent Field
SC-UB3LYP...Spin Corrected Unrestricted B3LYP (see reference [67])
SOD...Superoxide Dismutase
TISE...Time-Independent Schrödinger Equation

Abbreviations for organic molecules and ligands:
DMS...dimethyl sulfide
Im...Imidazole
Ind...Indazole
O-dmso...O-coordinated dimethyl sulfoxide
S-dmso...S-coordinated dimethyl sulfoxide

Me–H...methane
Et–H...ethane
$MeNH_2$...methylamine
$IprNH_2$...isopropylamine
Me–SH...methyl thiol

Symbols

$\widehat{H}$...Hamilton Operator (Hamiltonian)
Ψ...Wave Function of the total system
E...energy
$\hat{T}$...Kinetic energy operator
$\hat{V}$...Potential energy operator
h...Planck's constant
$\hbar = \frac{h}{2\pi}$...Planck's constant divided by $2\pi = 1$ in atomic units

N_α...total number of nuclei. Nuclei have greek indices
$\sum_{\alpha=1}^{N_\alpha}$...Sum running over all nuclei α
$\nabla_\alpha^2 = \frac{\partial^2}{\partial x_\alpha^2} + \frac{\partial^2}{\partial y_\alpha^2} + \frac{\partial^2}{\partial z_\alpha^2}$...Laplace Operator (for Cartesian coordinates α).
m_α...mass of nucleus α
m_e...mass of an electron = 1 in atomic units
$\sum_{i=1}^{n}$...Sum running over all electrons i
n...total number of electrons
ϵ_0...vacuum permittivity
z_α...charge number of nucleus α
e...elementary charge = 1 in atomic units
$\vec{r}$...general spatial coordinate
$\vec{r}_i$...vector giving the position i
$\vec{r}_\alpha$...vector giving the position of nucleus α
$r_{ij} = |\vec{r}_i - \vec{r}_j|$...distance between positions i and j
$r_{i\alpha} = |\vec{r}_i - \vec{r}_\alpha|$...distance between positions i and α
$r_{\alpha\beta} = |\vec{r}_\alpha - \vec{r}_\beta|$...distance between positions α and β
$\widehat{H}_{\mathrm{el}}$...electronic Hamiltonian
Ψ_{el}...electronic wave function
E_{el}...electronic energy
$\vec{x}_i$...vector giving the spin coordinates of electron i
$|\Psi\rangle$...Slater Determinant
$\chi_a(i)$...spin orbital a for electron i
E_0...ground state energy
$\hat{f}$...Fock operator
ε...one-electron energy
$\hat{v}^{\mathrm{HF}}$...Hartree-Fock potential
$\hat{h}$...core Hamiltonian
$\hat{j}$...Coulomb operator
$\hat{k}$...exchange operator
E_{HF}...Hartree-Fock energy
ρ...density
n...total number of electrons in the free electron system
$\mathfrak{E}$... energy levels of the free particle
n_x, n_y, n_z...quantum numbers in x, y and z directions
l...length
$\mathfrak{f}$...Fermi-Dirac distribution
μ...chemical potential
$\mathrm{k_B}$...Boltzmann constant
Θ...absolute temperature
$g(\mathfrak{E})$...density of states
$\mathfrak{E}_F$...Fermi energy
$\varkappa$..."condensed" constants
$T_{\mathrm{TF}}[\rho]$...Thomas-Fermi kinetic energy functional
C_{F}...Thomas-Fermi constant
V...general (external) Potential
$E[\rho]$...energy as a functional of the density
$T[\rho]$...kinetic energy functional

$V_{\mathrm{ne}}[\rho]$...potential energy functional between the nuclei and the electrons
$V_{\mathrm{ee}}[\rho]$...potential energy functional between the electrons
$F_{\mathrm{HK}}[\rho]$...Hohenberg-Kohn functional
$T_{\mathrm{KS}}[\rho]$...Kohn-Sham kinetic energy functional
σ...general spin coordinate
$\uparrow$...up spin
$\downarrow$...down spin
$\sum_{\sigma}$...sum over the spin coordinates
$F_{\mathrm{KS}}[\rho]$...Kohn-Sham functional
$J[\rho]$...coulomb functional
$E_{xc}[\rho]$...exchange-correlation functional
$V_{\mathrm{eff,KS}}$...effective Kohn-Sham potential
V_{xc}...exchange-correlation potential
$\hat{f}^{\mathrm{KS}}$...Kohn-Sham Fock operator
$\rho^{\uparrow}$...up spin density
$\rho^{\downarrow}$...down spin density
E_x...exchange energy
E_c...correlation energy
ξ...spin polarization
$\vec{\nabla}$...gradient
E_{SCF}...self consistent field energy, depending on method and basis set
s_a...a^{th} order scaling coefficient
$C_a^{\alpha\beta}$...a^{th} order dispersion coefficient between atoms α and β
f_{dmp}...damping function
a_0...Bohr radius = 1 in atomic units
I_p...ionization potential
$\mathfrak{P}$...static polarizability
m...multiplicity
$^m|\Psi\rangle$...Slater determinant for given m
C...generalized constant
$\langle\hat{S}^2\rangle$...expectation value of the $\hat{S}^2$ operator
e...base of the natural logarithm (Euler Number)
ϵ...dielectric constant
φ...electrostatic potential
ρ_S...solute charge density
c_i^{∞}...bulk concentration of ion i
λ...accessibility
ΔE...energy difference
ΔG...free energy difference
$\Delta_R G_{\mathrm{sol}}$...reaction free energy in solution

Appendix A

In this appendix the calculated (B3LYP/B1) and the experimental structures of **K1** are compared. The X-ray data of **K1** are from reference [93]. In reference [93], the PPh_4^+ salt of **K1** was measured.

Table A1: Selected experimental and calculated (optimized at the B3LYP/B1 level of theory) structural features of the **K1** compound, the KP1019 anion (one negative charge). Distances are given in Å. Angles are given in degrees.

Geometry (B3LYP/B1)	Feature	calculated	experimental [93]
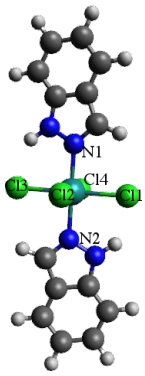	Ru–Cl1	2.44	2.37
	Ru–Cl2	2.39	2.36
	Ru–Cl3	2.44	2.36
	Ru–Cl4	2.39	2.36
	Ru–N1	2.09	2.05
	Ru–N2	2.09	2.07
	N1-Ru-N2	178.33	179.86
	N1-Ru-Cl1	90.59	90.33
	N1-Ru-Cl2	90.07	89.63
	Cl1-Ru-Cl2	90.36	89.85
	Cl1-Ru-Cl3	179.28	177.78
	Cl2-Ru-Cl4	180.00	177.44

As Table A1 shows, the experimental and computational geometries agree reasonably . Only some of the Ru–Cl bond lengths differ by more than 0.04 Å. This is remarkable when one considers that the B3LYP/B1 method is for the gas phase and the experimental data are from X-ray crystallography.

Appendix B: Zusammenfassung der Arbeit in deutscher Sprache

Diese Masterarbeit behandelt die Reduktions-Oxidationschemie von Rutheniumkomplexen in der Gegenwart von reaktiven Sauerstoffspezies (ROS). KP1019 und NAMI-A, zwei Rutheniumverbindungen, die sich zur Zeit in klinischen Studien befinden, wurden als Modellssysteme zur Untersuchung chemischer Reaktionen mittels einer Dichtefunktionaltheorie (DFT)- Methode verwendet. Der Zweck dieser Arbeit ist es, Wissen über die Chemie dieser Verbindungen in der Gegenwart von Wasserstoffperoxid zu erlangen und eventuelle Folgereaktionen zu studieren. Damit wollen wir dazu beitragen, die Reaktionsmechanismen von KP1019 und NAMI-A mit ROS aufzuklären. Letztenendes ist das Ziel, Schlussfolgerungen über die möglichen redoxchemischen Wirkmechanismen von Rutheniumantikrebsverbindungen *in vivo* zu ziehen.

References

[1] Graf, N. and Lippard, S. J. Redox activation of metal-based prodrugs as a strategy for drug delivery. *Advanced Drug Delivery Reviews*, 64:993–1004, 2012.

[2] Jungwirth, U.; Kowol, C.; Keppler, B.; Hartinger, C.; Berger, W. and Heffeter, P. Anticancer activity of metal complexes: involvement of redox processes. *Antioxidants and Redox Signaling*, 15:1085–1127, 2011.

[3] Rosenberg, B.; Vancamp, L. and Krigas, T. Inhibition of cell division in Escherichia coli by electrolysis products from a platinum electrode. *Nature*, 205:698–699, 1965.

[4] Rosenberg, B.; Vancamp, L.; Troso, J. E. and Mansour, V. H. Platinum compounds: a new class of potent antitumour agents. *Nature*, 222:385–386, 1969.

[5] Einhorn, L. H. Treatment of testicular cancer: a new and improved model. *Journal of Clinical Oncology*, 8:1777–81, 1990.

[6] Wang, D. and Lippard, S. J. Cellular processing of platinum anticancer drugs. *Nature Reviews Drug Discovery*, 4:307–320, 2005.

[7] Hall, M. D. and Hambley, T. W. Platinum(IV) antitumour compounds: their bioinorganic chemistry. *Coordination Chemistry Reviews*, 232:49 – 67, 2002.

[8] Wheate, N. J.; Walker, S.; Craig, G. E. and Oun, R. The status of platinum anticancer drugs in the clinic and in clinical trials. *Dalton Transactions*, 39:8113–8127, 2010.

[9] Hartinger, C. G.; Jakupec, M. A.; Zorbas-Seifried, S.; Groessl, M.; Egger, A.; Berger, W.; Haralabos, Z.; Dyson, P. J. and Keppler, B. K. KP1019, A new redox-active anticancer agent – preclinical development and results of a clinical phase I study in tumor patients. *Chemistry and Biodiversity*, 5:2140–2155, 2008.

[10] Rademaker-Lakhai, J. M.; van den Bongard, D. and Pluim, D. e. a. A phase I and pharmacological study with imidazolium-trans-DMSO-imidazole-tetrachlororuthenate, a novel ruthenium anticancer agent. *Clinical Cancer Research*, 10:3717–3727, 2004.

[11] Lipponer, K.-G.; Vogel, E. and Keppler, B. K. Synthesis, characterization and solution chemistry of trans-indazoliumtetrachlorobis(indazole)ruthenate(III), a new anticancer ruthenium complex. IR, UV, NMR, HPLC investigations and antitumor activity. Crystal structures of trans-1-methyl-indazoliumtetrachlorobis-(1-methylindazole)ruthenate(III) and its hydrolysis product trans-monoaquatrichlorobis-(1-methylindazole)-ruthenate(III). *Metal Based Drugs*, 3:243–260, 1996.

[12] Pongratz, M.; Schluga, P.; Jakupec, M. A.; Arion, V. B.; Hartinger, C. G.; Allmaier, G. and Keppler, B. K. Transferrin binding and transferrin-mediated cellular uptake of the ruthenium coordination compound KP1019, studied by means of AAS, ESI-MS and CD spectroscopy. *Journal of Analytical Atomic Spectrometry*, 19:46–51, 2004.

[13] Jakupec, M. A.; Reisner, E.; Eichinger, A.; Pongratz, M.; Arion, V. B.; Galanski, M.; Hartinger, C. G. and Keppler, B. K. Redox-active antineoplastic ruthenium complexes with indazole: Correlation of in vitro potency and reduction potential. *Journal of Medicinal Chemistry*, 48:2831–2837, 2005.

[14] Bartel, C.; Egger, A.; Jakupec, M.; Heffeter, P.; Galanski, M.; Berger, W. and Keppler, B. Influence of ascorbic acid on the activity of the investigational anticancer drug KP1019. *Journal of Biological Inorganic Chemistry*, 16:1205–1215, 2011.

[15] Gava, B.; Zorzet, S.; Spessotto, P.; Cocchietto, M. and Sava, G. Inhibition of B16 melanoma metastases with the ruthenium complex imidazolium trans-imidazoledimethylsulfoxide- tetrachlororuthenate and down-regulation of tumor cell invasion. *Journal of Pharmacology and Experimental Therapeutics*, 317:284–291, 2006.

[16] Bacac, M.; Hotze, A. C.; van der Schilden, K.; Haasnoot, J. G.; Pacor, S.; Alessio, E.; Sava, G. and Reedijk, J. The hydrolysis of the anti-cancer ruthenium complex NAMI-A affects its DNA binding and antimetastatic activity: an NMR evaluation. *Journal of Inorganic Biochemistry*, 98:402 – 412, 2004.

[17] Mestroni, G.; Alessio, E.; Sava, G.; Pacor, S.; Coluccia, M. and Boccarelli, A. Water-soluble ruthenium(III)-dimethyl sulfoxide complexes: Chemical behaviour and pharmaceutical properties. *Metal Based Drugs*, 1:41–63, 1994.

[18] Brindell, M.; Piotrowska, D.; Shoukry, A.; Stochel, G. and Eldik, R. Kinetics and mechanism of the reduction of (ImH)[trans-$RuCl_4$(dmso)(Im)] by ascorbic acid in acidic aqueous solution. *Journal of Biological Inorganic Chemistry*, 12:809–818, 2007.

[19] Brindell, M.; Stawoska, I.; Supel, J.; Skoczowski, A.; Stochel, G. and Eldik, R. The reduction of (ImH)[trans-$Ru^{III}Cl_4$(dmso)(Im)] under physiological conditions: preferential reaction of the reduced complex with human serum albumin. *JBIC Journal of Biological Inorganic Chemistry*, 13:909–918, 2008.

[20] Groessl, M.; Zava, O. and Dyson, P. J. Cellular uptake and subcellular distribution of ruthenium-based metallodrugs under clinical investigation versus cisplatin. *Metallomics*, 3:591–599, 2011.

[21] Vargiu, A. V.; Robertazzi, A.; Magistrato, A.; Ruggerone, P. and Carloni, P. The hydrolysis mechanism of the anticancer ruthenium drugs NAMI-A and ICR investigated by DFT-PCM calculations. *The Journal of Physical Chemistry B*, 112:4401–4409, 2008.

[22] Chen, J.; Chen, L.; Liao, S.; Zheng, K. and Ji, L. A theoretical study on the hydrolysis process of the antimetastatic ruthenium(III) complex NAMI-A. *The Journal of Physical Chemistry B*, 111:7862–7869, 2007.

[23] Chiorescu, I.; Chang, Y.-C.; Arion, V. B.; Keppler, B. and Deubel, D. V. to be published 2013.

[24] Clarke, M. J. Oncological implications of the chemistry of ruthenium. In H. Sigel, editor, *Metal Ions in Biological Systems*, volume 11: Metal Complexes as Anticancer Agents, page 231. Marcel Dekker, Basel and New York, 1980.

[25] Höckel, M.; Schlenger, K.; Knoop, C. and Vaupel, P. Oxygenation of carcinomas of the uterine cervix: evaluation by computerized O_2 tension measurements. *Cancer Research*, 51:6098–6102, 1991.

[26] Höckel, M. and Vaupel, P. Tumor hypoxia: Definitions and current clinical, biologic, and molecular aspects. *Journal of the National Cancer Institute*, 93:266–276, 2001.

[27] Harris, A. L. Hypoxia - a key regulatory factor in tumor growth. *Nature Reviews Cancer*, 2:38–47, 2002.

[28] Carr, J.; Tingle, M. and McKeage, M. Satraplatin activation by haemoglobin, cytochrome C and liver microsomes in vitro. *Cancer Chemotherapy and Pharmacology*, 57:483–490, 2006.

[29] Szatrowski, T. P. and Nathan, C. F. Production of large amounts of hydrogen peroxide by human tumor cells. *Cancer Research*, 51:794–798, 1991.

[30] Taube, H. Rates and mechanisms of substitution in inorganic complexes in solution. *Chemical Reviews*, 50:69–126, 1952.

[31] Reedijk, J. Metal-ligand exchange kinetics in platinum and ruthenium complexes. *Platinum Metals Review*, 52:2–11, 2008.

[32] Veal, E. A.; Day, A. M. and Morgan, B. A. Hydrogen peroxide sensing and signaling. *Molecular Cell*, 26:1 – 14, 2007.

[33] Fenton, H. J. H. LXXIII.-Oxidation of tartaric acid in presence of iron. *Journal of the Chemical Society, Transactions*, 65:899–910, 1894.

[34] Haber, F. and Weiss, J. The catalytic decomposition of hydrogen peroxide by iron salts. *Proceedings of the Royal Society of London. Series A*, 147:332–351, 1934.

[35] Bray, W. and Gorin, M. Ferryl ion, a compound of tetravalent iron. *Journal of the American Chemical Society*, 54:2124–2125, 1932.

[36] Valko, M.; Izakovic, M.; Mazur, M.; Rhodes, C. J. and Telser, J. Role of oxygen radicals in DNA damage and cancer incidence. *Molecular and Cellular Biochemistry*, 266:37–56, 2004.

[37] Kadiiska, M. and Mason, R. In vivo copper mediated free radical production: an ESR spin-trapping study. *Spectrochimica Acta Part A-molecular and Biomolecular Spectroscopy*, 58:1227–1239, 2002.

[38] Buda, F.; Ensing, B.; Gribnau, M. and Baerends, E. DFT study of the active intermediate in the Fenton reaction. *Chem. Eur. J.*, 7:2775–2783, 2001.

[39] Cadet, J.; Delatour, T.; Douki, T.; Gasparutto, D.; Pouget, J.-P.; Ravanat, J.-L. and Sauvaigo, S. Hydroxyl radicals and DNA base damage. *Mutation Research/Fundamental and Molecular Mechanisms of Mutagenesis*, 424:9 – 21, 1999.

[40] Balasubramanian, B.; Pogozelski, W. K. and Tullius, T. D. DNA strand breaking by the hydroxyl radical is governed by the accessible surface areas of the hydrogen atoms of the DNA backbone. *Proceedings of the National Academy of Sciences*, 95:9738–9743, 1998.

[41] Tainer, J. A.; Getzoff, E. D.; Richardson, J. S. and Richardson, D. C. Structure and mechanism of copper, zinc superoxide dismutase. *Nature*, 306:284–287, 1983.

[42] Chelikani, P.; Fita, I. and Loewen, P. Diversity of structures and properties among catalases. *Cellular and Molecular Life Sciences CMLS*, 61:192–208, 2004.

[43] Whittaker, J. W. Non-heme manganese catalase – The 'other' catalase. *Archives of Biochemistry and Biophysics*, 525:111 – 120, 2012.

[44] Jakoptisch, C.; Droghetti, E.; Schmuckenschlager, F.; Furtmüller, P. G.; Smulevich, G. and Obinger, C. Role of the main access channel of catalase-peroxidase in catalysis. *Journal of Biological Chemistry*, 280:42411–42422, 2005.

[45] Burdon, R. H. Superoxide and hydrogen peroxide in relation to mammalian cell proliferation. *Free Radical Biology and Medicine*, 18:775–794, 1995.

[46] Lim, S. D.; Sun, C.; Lambeth, J. D.; Marshall, F.; Amin, M.; Chung, L.; Petros, J. A. and Arnold, R. S. Increased Nox1 and hydrogen peroxide in prostate cancer. *The Prostate*, 62:200–207, 2005.

[47] López-Lózaro, M. Dual role of hydrogen peroxide in cancer: Possible relevance to cancer chemoprevention and therapy. *Cancer Letters*, 252:1 – 8, 2007.

[48] Gorman, A.; McGowan, A. and Cotter, T. G. Role of peroxide and superoxide anion during tumour cell apoptosis. *Febs Letters*, 404:27 – 33, 1997.

[49] Kapitza, S.; Jakupec, M. A.; Uhl, M.; Keppler, B. K. and Marian, B. The heterocyclic ruthenium(III) complex KP1019 (FFC14A) causes DNA damage and oxidative stress in colorectal tumor cells. *Cancer Letters*, 226:115 – 121, 2005.

[50] Zhou, Y.; Hileman, E. O.; Plunkett, W.; Keating, M. J. and Huang, P. Free radical stress in chronic lymphocytic leukemia cells and its role in cellular sensitivity to ROS-generating anticancer agents. *Blood*, 101:4098–4104, 2003.

[51] Born, M. and Oppenheimer, R. Zur Quantentheorie der Molekeln. *Annalen der Physik*, 389:457–484, 1927.

[52] Szabo, A. and Ostlund, N. S. *Modern Quantum Chemistry: Introduction to Advanced Electronic Structure Theory*. Dover Publications, Inc., first edition, revised edition, 1996.

[53] Koopmans, T. Über die Zuordnung von Wellenfunktionen und Eigenwerten zu den einzelnen Elektronen eines Atoms. *Physica*, 1:104–113, 1934.

[54] Parr, R. G. and Yang, W. *Density-Functional Theory of Atoms and Molecules*. Oxford University Press, 1989.

[55] Hohenberg, P. and Kohn, W. Inhomogeneous electron gas. *Physical Review*, 136:B864–B871, 1964.

[56] Kohn, W. and Sham, L. J. Self-consistent equations including exchange and correlation effects. *Physical Review*, 140:A1133–A1138, 1965.

[57] Vosko, S. H.; Wilk, L. and Nusair, M. Accurate spin-dependent electron liquid correlation energies for local spin density calculations: a critical analysis. *Canadian Journal of Physics*, 58:1200–1211, 1980.

[58] Becke, A. D. Density-functional exchange-energy approximation with correct asymptotic behavior. *Physical Review A*, 38:3098–3100, 1988.

[59] Lee, C.; Yang, W. and Parr, R. G. Development of the Colle-Salvetti correlation-energy formula into a functional of the electron density. *Phys. Rev. B*, 37:785–789, 1988.

[60] Colle, R. and Salvetti, O. Approximate calculation of correlation energy for closed shells. *Theoretica Chimica Acta*, 37:329–334, 1975.

[61] Becke, A. D. Density functional thermochemistry. III. The role of exact exchange. *Journal of Chemical Physics*, 98:5648–5652, 1993.

[62] Stephens, P. J.; Devlin, F. J.; Chabalowski, C. F. and Frisch, M. J. Ab initio calculation of vibrational absorption and circular dichroism spectra using density functional force fields. *The Journal of Physical Chemistry*, 98:11623–11627, 1994.

[63] Grimme, S. Semiempirical GGA-type density functional constructed with a long-range dispersion correction. *Journal of Computational Chemistry*, 27:1787–1799, 2006.

[64] Adamo, C. and Barone, V. Toward reliable density functional methods without adjustable parameters: The PBE0 model. *The Journal of Chemical Physics*, 110:6158–6170, 1999.

[65] Goerigk, L. and Grimme, S. A thorough benchmark of density functional methods for general main group thermochemistry, kinetics, and noncovalent interactions. *Physical Chemistry Chemical Physics*, 13:6670–6688, 2011.

[66] Noodleman, L. Valence Bond description of antiferromagnetic coupling in transition metal dimers. *Journal of Chemical Physics*, 74:5737–5743, 1981.

[67] Yamaguchi, K.; Jensen, F.; Dorigo, A. and Houk, K. A spin correction procedure for unrestricted Hartree-Fock and Møller-Plesset wavefunctions for singlet diradicals and polyradicals. *Chemical Physics Letters*, 149:537 – 542, 1988.

[68] Ditchfield, R.; Hehre, W. J. and Pople, J. A. Self-consistent molecular-orbital methods. IX. An extended Gaussian-type basis for molecular-orbital studies of organic molecules. *The Journal of Chemical Physics*, 54:724–728, 1971.

[69] Andrae, D.; Haeussermann, U.; Dolg, M.; Stoll, H. and Preuss, H. Energy-adjusted ab initio pseudopotentials for the second and third row transition elements. *Theoretica Chimica Acta*, 77:123–141, 1990.

[70] Frisch, M. J.; Trucks, G. W.; Schlegel, H. B.; Scuseria, G. E.; Robb, M. A.; Cheeseman, J. R.; Scalmani, G.; Barone, V.; Mennucci, B.; Petersson, G. A.; Nakatsuji, H.; Caricato, M.; Li, X.; Hratchian, H. P.; Izmaylov, A. F.; Bloino, J.; Zheng, G.; Sonnenberg, J. L.; Hada, M.; Ehara, M.; Toyota, K.; Fukuda, R.; Hasegawa, J.; Ishida, M.; Nakajima, T.; Honda, Y.; Kitao, O.; Nakai, H.; Vreven, T.; Montgomery, J. A., Jr.; Peralta, J. E.; Ogliaro, F.; Bearpark, M.; Heyd, J. J.; Brothers, E.; Kudin, K. N.; Staroverov, V. N.; Kobayashi, R.; Norm, J.; Raghavachari, K.; Rendell, A.; Burant, J. C.; Iyengar, S. S.; Tomasi, J.; Cossi, M.; Rega, N.; Millam, J. M.; Klene, M.; Knox, J. E.; Cross, J. B.; Bakken, V.; Adamo, C.; Jaramillo, J.; Gomperts, R.; Stratmann, R. E.; Yazyev, O.; Austin, A. J.; Cammi, R.; Pomelli, C.; Ochterski, J. W.; Martin, R. L.; Morokuma, K.; Zakrzewski, V. G.; Voth, G. A.; Salvador, P.; Dannenberg, J. J.; Dapprich, S.; Daniels, A. D.; Farkas, O.; Foresman, J. B.; Ortiz, J. V.; Cioslowski, J. and Fox, D. J. Gaussian 09 Revision C.01. Gaussian Inc., Wallingford CT, 2010.

[71] Hay, J. P. and Wadt, W. R. Ab initio effective core potentials for molecular calculations. Potentials for K to Au including the outermost core orbitals. *Journal of Chemical Physics*, 82:299–310, 1985.

[72] Schrodinger, LLC, New York, NY. Jaguar, version 8.0, 2013.

[73] Tomasi, J.; Mennucci, B. and Cammi, R. Quantum mechanical continuum solvation models. *Chemical Reviews*, 105:2999–3094, 2005.

[74] Debye, P. and Hueckel, E. Zur Theorie der Elektrolyte. *Physikalische Zeitschrift*, 24:185–206, 1923.

[75] Chapman, D. L. A contribution to the theory of electrocapillarity. *Philosophical Magazine*, 25:475–481, 1913.

[76] Fogolari, F.; Brigo, A. and Molinari, H. The Poisson–Boltzmann equation for biomolecular electrostatics: a tool for structural biology. *Journal of Molecular Recognition*, 15:377–392, 2002.

[77] Tannor, D. J.; Marten, B.; Murphy, R.; Friesner, R. A.; Sitkoff, D.; Nicholls, A.; Honig, B.; Ringnalda, M. and Goddard, W. A. Accurate first principles calculation of molecular charge distributions and solvation energies from ab initio quantum mechanics and continuum dielectric theory. *Journal of the American Chemical Society*, 116:11875–11882, 1994.

[78] Hanwell, M. D.; Curtis, D. E.; Lonie, D. C.; Vandermeersch, T.; Zurek, E. and Hutchison, G. R. Avogadro: An advanced semantic chemical editor, visualization, and analysis platform, 2012. Version 1.0.3.

[79] Rappe, A. K.; Casewit, C. J.; Colwell, K. S.; Goddard, W. A. and Skiff, W. M. UFF, a full periodic table force field for molecular mechanics and molecular dynamics simulations. *Journal of the American Chemical Society*, 114:10024–10035, 1992.

[80] Hehre, W. J.; Ditchfield, R. and Pople, J. A. Self-consistent molecular orbital methods. XII. Further extensions of Gaussian-type basis sets for use in molecular orbital studies of organic molecules. *The Journal of Chemical Physics*, 56:2257–2261, 1972.

[81] Binkley, J. S.; Pople, J. A. and Hehre, W. J. Self-consistent molecular orbital methods. 21. Small split-valence basis sets for first-row elements. *Journal of the American Chemical Society*, 102:939–947, 1980.

[82] McLean, A. D. and Chandler, G. S. Contracted Gaussian basis sets for molecular calculations. I. Second row atoms, Z=11–18. *The Journal of Chemical Physics*, 72:5639–5648, 1980.

[83] Deubel, D. V. Thianthrene 5-oxide as a probe for the electronic character of oxygen-transfer reactions: Re-interpretation of experiments required. *The Journal of Organic Chemistry*, 66:2686–2691, 2001.

[84] Martin, J. M. L. and Sundermann, A. Correlation consistent valence basis sets for use with the Stuttgart-Dresden-Bonn relativistic effective core potentials: The atoms Ga-Kr and In-Xe. *Journal of Chemical Physics*, 114:3408–3420, 2001.

[85] Weast, R., editor. *CRC Handbook of Chemistry and Physics*. CRC Press, Boca Raton, FL, 60th edition, 1979.

[86] Chiorescu, I.; Deubel, D. V.; Arion, V. B. and Keppler, B. K. Computational electrochemistry of ruthenium anticancer Agents. Unprecedented benchmarking of implicit solvation methods. *Journal of Chemical Theory and Computation*, 4:499–506, 2008.

[87] Young, D. *Computational Chemistry A Practical Guide for Applying Techniques to Real World Problems*. Wiley Interscience, 2001.

[88] Sonnenberg, J. L.; Schlegel, B. and Hratchian, H. P. Spin contamination in inorganic chemistry calculations. In *Encyclopedia of Inorganic and Bioinorganic Chemistry*. 2011.

[89] McKellar, A. R. W.; Bunker, P. R.; Sears, T. J.; Evenson, K. M.; Saykally, R. J. and Langhoff, S. R. Far infrared laser magnetic resonance of singlet methylene: Singlet–triplet perturbations, singlet–triplet transitions, and the singlet–triplet splitting[sup a)]. *The Journal of Chemical Physics*, 79:5251–5264, 1983.

[90] Yamaguchi, Y.; Sherrill, C. D. and Schaefer, H. F. The X 3B1, a 1A1, b 1B1, and c 1A1 Electronic States of CH2. *The Journal of Physical Chemistry*, 100:7911–7918, 1996.

[91] Gibson, S. T.; Greene, J. P. and Berkowitz, J. Photoionization of the amidogen radical. *The Journal of Chemical Physics*, 83:4319–4328, 1985.

[92] Peyerimhoff, S. D. and Buenker, R. J. Ab initio MRD-CI potential surfaces for the low-lying states of the NH_2^+ molecular ion. *Chemical Physics*, 42:167–176, 1979.

[93] Peti, W.; Pieper, T.; Sommer, M.; Keppler, B. K. and Giester, G. Synthesis of tumor-inhibiting complex salts containing the anion trans-tetrachlorobis(indazole)ruthenate(III) and crystal structure of the tetraphenylphosphonium salt. *European Journal of Inorganic Chemistry*, 1999:1551–1555, 1999.

[94] Huheey, J. E. *Inorganic Chemistry Third Edition, Principles of Structure and Reactivity.* Harper & Row, Publishers, Inc., 1983.

[95] Hummer, A. A.; Heffeter, P.; Berger, W.; Filipits, M.; Batchelor, D.; Büchel, G. E.; Jakupec, M. A.; Keppler, B. K. and Rompel, A. X-ray absorption near edge structure spectroscopy to resolve the in vivo chemistry of the redox-active indazolium trans-[tetrachlorobis(1H-indazole)ruthenate(III)] (KP1019). *Journal of Medicinal Chemistry*, 56:1182–1196, 2013.

[96] Kojima, T.; Nakayama, K.; Ikemura, K.; Ogura, T. and Fukuzumi, S. Formation of a ruthenium(IV)-oxo complex by electron-transfer oxidation of a coordinatively saturated ruthenium(II) complex and detection of oxygen-rebound intermediates in C–H bond oxygenation. *Journal of the American Chemical Society*, 133:11692–11700, 2011.

[97] Che, C.-M. and Lau, T.-C. Ruthenium and osmium: high oxidation states. In E. in Chief: J. A. McCleverty and T. J. Meyer, editors, *Comprehensive Coordination Chemistry II*, pages 733 – 847. Pergamon, Oxford, 2003.

[98] Millis, K. K.; Weaver, K. H. and Rabenstein, D. L. Oxidation/reduction potential of glutathione. *The Journal of Organic Chemistry*, 58:4144–4146, 1993.

[99] Truhlar, D. G.; Cramer, C. J.; Lewis, A. and Bumpus, J. A. Molecular modeling of environmentally important processes: reduction potentials (including corrections). *Journal of Chemical Education*, 81:596, 2004.

[100] Pearson, R. G. Hard and Soft Acids and Bases. *Journal of the American Chemical Society*, 85:3533–3539, 1963.

[101] Chu, J.-W. and Trout, B. L. On the mechanisms of oxidation of organic sulfides by H_2O_2 in aqueous solutions. *Journal of the American Chemical Society*, 126:900–908, 2004.

[102] Dankleff, M. A. P.; Curci, R.; Edwards, J. O. and Pyun, H.-Y. The influence of solvent on the oxidation of thioxane by hydrogen peroxide and by tert-butyl hydroperoxide. *Journal of the American Chemical Society*, 90:3209–3218, 1968.

[103] Usharani, D.; Janardanan, D.; Li, C. and Shaik, S. A theory for bioinorganic chemical reactivity of oxometal complexes and analogous oxidants: The exchange and orbital-selection rules. *Accounts of Chemical Research*, 46:471–482, 2013.

[104] Groves, J. T. Key elements of the chemistry of cytochrome P-450: The oxygen rebound mechanism. *Journal of Chemical Education*, 62:928, 1985.

[105] Groves, J. T. High-valent iron in chemical and biological oxidations. *Journal of Inorganic Biochemistry*, 100:434–447, 2006.

[106] Ensing, B.; Buda, F.; Gribnau, M. C. M. and Baerends, E. J. Methane-to-methanol oxidation by the hydrated iron(IV) oxo species in aqueous solution. A combined DFT and Car-Parinello molecular dynamics study. *Journal of the American Chemical Society*, 126:4355–4365, 2004.

[107] Rydberg, P. and Olsen, L. Do two different reaction mechanisms contribute to the hydroxylation of primary amines by cytochrome P450? *Journal of Chemical Theory and Computation*, 7:3399–3404, 2011.

[108] Rydberg, P.; Jørgensen, M. S.; Jacobsen, T. A.; Jacobsen, A.-M.; Madsen, K. G. and Olsen, L. Nitrogen inversion barriers affect the N–oxidation of tertiary alkylamines by cytochromes P 450. *Angewandte Chemie-international Edition*, 52:993–997, 2013.

[109] Ji, L. and Schüürmann, G. Model and mechanism: N-hydroxylation of primary aromatic amines by cytochrome P450. *Angewandte Chemie International Edition*, 52:744–748, 2013.

CURRICULUM VITAE

Christoph Alexander Bauer

Born: March 7th, 1989, Baden, Austria

Academic Background:

09/2008-10/2011: Studies of Chemistry at the University of Vienna

09/13/2011: B.Sc. in Chemistry (University of Vienna)

since 10/2012: M.Sc. thesis "Computational study on Ruthenium anticancer compounds in the presence of ROS" (working title) with Prof. Leticia González and Dr. Dirk Deubel

Relevant work experience:

09/2010: Internship at OMV oil refinery, Mannswörth, Austria

10/2011-01/2012: Student assistant (Tutorium) at the Institute of Organic Chemistry, University of Vienna

03/2013-07/2013: Student assistant (Tutorium) at the Institute of Organic Chemistry, University of Vienna

Research Interests:

Computational chemistry of anticancer transition metal compounds, electronic structure theory

Scholarships, grants, awards:

Scholarship for academic performance of the University of Vienna for the academic years 2008/2009, 2009/2010, 2010/2011 and 2011/2012 (awarded separately each year)

since 03/2011: Pro Scientia scholarship

Additional qualifications:

06/2007: Cambridge Certificate in Advanced English (Level C1)

06/2007: Diplôme D'Etudes En Langue Française DELF B1